SOL-GEL SYNTHESIS OF VANADIUM PHOSPHOROUS OXIDES FOR THE PARTIAL OXIDATION OF N-BUTANE TO MALEIC ANHYDRIDE

by

JUAN MANUEL SALAZAR

B. Sc., National University of Colombia, Manizales, 1999

AN ABSTRACT OF A DISSERTATION

submitted in partial fulfillment of the requirements for the degree

DOCTOR OF PHILOSOPHY

Department of Chemical Engineering
College of Engineering

KANSAS STATE UNIVERSITY
Manhattan, Kansas

2007

Abstract

Vanadium phosphorous oxide (VPO) is traditionally manufactured from solid vanadium oxides by synthesizing $VOHPO_4 \cdot 0.5H_2O$ (the precursor) followed by in-situ activation to produce $(VO)_2P_2O_7$ (the active phase). These catalysts considerably improve their performance when prepared as nanostructured materials and this study discusses an alternative synthesis method based on sol-gel techniques capable of producing nanostructured VPO. Vanadium(V) triisopropoxide oxide was reacted with ortho-phosphoric acid in tetrahydrofuran (THF). This procedure yielded a gel of $VOPO_4$ with interlayer entrapped molecules. The gels were dried at high pressure in an autoclave with controlled excess and composition of THF-2-propanol mixtures. The surface area of the obtained materials was between 50 and 120 m^2/g. Alcohol produced by the alkoxide hydrolysis and incorporated along with the excess solvent reduced the vanadium during the drying step. Therefore, after the autoclave drying, the solid $VOPO_4$ was converted to the precursor; and, non-agglomerated platelets were observed. Use of additional 2-propanol increased the amount of precursor in the powder but reduced its surface area and increased its crystallite size.

In general, sol-gel prepared catalysts were significantly more selective than the traditionally prepared materials, and it is suggested that the small crystallite size obtained in the precursor influenced the crystallite size of the active phase increasing their selectivity towards maleic anhydride. The evaluation of these materials as catalysts for the partial oxidation of n-butane at 673 K under mixtures of 1.5% n-butane in air yielded selectivity of 40% at 50% conversion compared to 25% selectivity at similar level of conversion produced by the traditionally prepared catalysts. Variations in the catalytic performance are attributed to observed polymorphism in the activated materials, which is evidenced by remarkable differences in the intrinsic activity. All precursors and catalysts were characterized by IR, XRD, SEM and BET, and the products of the catalytic tests were analyzed by GC.

SOL-GEL SYNTHESIS OF VANADIUM PHOSPHOROUS OXIDES FOR THE PARTIAL OXIDATION OF N-BUTANE TO MALEIC ANHYDRIDE

by

JUAN MANUEL SALAZAR

B. Sc., National University of Colombia, Manizales, 1999

A DISSERTATION

submitted in partial fulfillment of the requirements for the degree

DOCTOR OF PHILOSOPHY

Department of Chemical Engineering
College of Engineering

KANSAS STATE UNIVERSITY
Manhattan, Kansas

2007

Approved by:

Major Professor
Dr. Keith L. Hohn

Copyright

Abstract

Vanadium phosphorous oxide (VPO) is traditionally manufactured from solid vanadium oxides by synthesizing $VOHPO_4 \cdot 0.5H_2O$ (the precursor) followed by in-situ activation to produce $(VO)_2P_2O_7$ (the active phase). These catalysts considerably improve their performance when prepared as nanostructured materials and this study discusses an alternative synthesis method based on sol-gel techniques capable of producing nanostructured VPO. Vanadium(V) triisopropoxide oxide was reacted with ortho-phosphoric acid in tetrahydrofuran (THF). This procedure yielded a gel of $VOPO_4$ with interlayer entrapped molecules. The gels were dried at high pressure in an autoclave with controlled excess and composition of THF-2-propanol mixtures. The surface area of the obtained materials was between 50 and 120 m^2/g. Alcohol produced by the alkoxide hydrolysis and incorporated along with the excess solvent reduced the vanadium during the drying step. Therefore, after the autoclave drying, the solid $VOPO_4$ was converted to the precursor; and, non-agglomerated platelets were observed. Use of additional 2-propanol increased the amount of precursor in the powder but reduced its surface area and increased its crystallite size.

In general, sol-gel prepared catalysts were significantly more selective than the traditionally prepared materials, and it is suggested that the small crystallite size obtained in the precursor influenced the crystallite size of the active phase increasing their selectivity towards maleic anhydride. The evaluation of these materials as catalysts for the partial oxidation of n-butane at 673 K under mixtures of 1.5% n-butane in air yielded selectivity of 40% at 50% conversion compared to 25% selectivity at similar level of conversion produced by the traditionally prepared catalysts. Variations in the catalytic performance are attributed to observed polymorphism in the activated materials, which is evidenced by remarkable differences in the intrinsic activity. All precursors and catalysts were characterized by IR, XRD, SEM and BET, and the products of the catalytic tests were analyzed by GC.

Table of Contents

List of Figures

List of Tables

Acknowledgements

I want to acknowledge my major advisor, Dr. Keith L. Hohn for the unconditional support and contribution to all my ideas to carry out the research compiled in this dissertation. His knowledge, guidance, kindness and patience are deeply appreciated and admired. I also want to acknowledge the U.S. Department of Energy for the financial support to this project.

I want to thank the members of the evaluating committee: Dr. James Edgar, Dr. John Schlup, Dr. Terry King, Dr. Kenneth Klabunde and the outside chair Dr. John Tomich for the evaluation of this study and the very valuable contributions to it.

I want to recognize the scientific discussions with former members of our research group: Dr. Abdennour Bourane and Dr. Yu-Chuan Lin, they immensely contributed to the experiments and the conclusions of this work. And also I recognize the cooperation during the daily work in the lab from my colleagues Chundi Cao and Chien-Chang Huang.

I want to express gratitude to the staff on the Department of Chemical Engineering: Florence Sperman, Cindy Barnhart, Alison Hodges and David Threewit for their cooperation in all the administrative activities related to this research. I also want to express my gratitude and admiration to Dr. L.T. Fan for his mentoring and contribution to my education in Chemical Engineering.

X-ray diffraction analyses were possible thanks to the department of Chemistry at K-State and SEM analyses thanks to the cooperation of Kent Hampton at the department of Entomology also at K-State.

I want to thank my beloved wife Deisy Corredor for her amazing love, encouragement, patience, complicity and extraordinary colleagueship.

I want to thank my parents, my sister and my little brother for all their encouragement, love and support.

Thanks to the members of the Colombian Association of KSU for their enthusiasm to share Colombian culture at K-State, it was a great complement to my research endeavors.

Finally, thanks to God for life, chemical engineering and everything…

Dedication

To my best friend and greatest love
Deisy

To my parents
Luis Álvaro and Viainery

To my sister
Liana María
and my little brother
Tomás

To the Republic of Colombia and its National University

Preface

Vanadium phosphorous oxides are well identified and characterized crystalline materials that have been employed in the partial oxidation of C_4 hydrocarbons [1]. N-butane partial oxidation on a vanadium phosphorous oxide catalyst is the only partial oxidation of a C_1-C_4 alkane that has been scaled up to the industrial level [2]. The commercially available compound used as the catalyst for this reaction is the vanadyl pyrophosphate, $(VO)_2P_2O_7$.

The preparation of vanadyl pyrophosphate strongly influences its catalytic activity [3, 4]. The first step for this preparation is the synthesis of $VOHPO_4 \bullet 0.5H_2O$, referred to as the precursor or the hemihydrate in this work. The type of reagents, the ratio of phosphorous to vanadium, the nature of the solvent and the conditions of the reduction step can control the characteristics of the precursor and thus the catalytic behavior of $(VO)_2P_2O_7$ [3], which will be referred to as the active phase in this work. Several techniques have been applied to increase the activity of VPO catalysts, and they are summarized by Hutchings [5] and Ballarini et al. [6]. Among them, we focus on those that increase the surface area of either the precursor or the final active phase.

The main purpose of this work is exploring a sol-gel technique, namely, the metal alkoxide method (MAM) for the preparation of high surface area precursors and their corresponding activated phases as potentially improved catalysts. Sol-gel methods have often been used to synthesize metal oxide catalysts and adsorbents due to their ability to regulate the composition and nanostructure of the final material during the earlier stages of synthesis [7]. Thus, certain important aspects of the sol-gel process that have not been previously studied in any detail are the objectives of the present work. The contributions of this dissertation to the sol-gel synthesis of VPO are chronologically described from Chapter 2 through Chapter 5. The first modification to the sol-gel synthesis was suggested by the literature and the subsequent ones were proposed based on the results of its application. This process was repeated throughout the chapters that are described bellow.

Chapter 1 entails a summary of the main issues related to the partial oxidation of n-butane and vanadium phosphorous oxides. Chemical steps involved in the mechanism and the

catalytic materials responsible of them are described in section 1.1 . A summary of the most recent approaches to improve the characteristics of the catalysts is presented in section 1.2 . Traditional preparation techniques, novel methodologies to increase surface area of the catalytic materials and fundamentals of the sol-gel method are compiled in section 1.3

Chapter 2 describes the experimental conditions (section 2.1) and the results (sections 2.2 and 2.3) of the use of MAM in the synthesis of vanadium phosphorous oxides. The chapter proposes the use of an autoclave to remove the solvent from the VPO gel.

Chapter 3 includes the experimental conditions (section 3.1) to evaluate the materials (section 3.2) as catalysts for the partial oxidation of n-butane.

Chapter 4 explores additional possibilities of the MAM to prepare the precursors. Sections 4.1 , 4.2.1 and 4.2.2 describe the experimental conditions and some theoretical aspects of for the discussion in the following sections. Section 4.3 studies some necessary conditions to obtain highly concentrated hemihydrates as precursors. Phase equilibria conditions of the autoclave drying are predicted and compared with the experimental results in section 4.4 . At the same section a simple method based on the microcrystalline analysis of catalysts is proposed to estimate their level of purity. A modification of the gelation process conditions is evaluated in section 4.5 and finally the catalytic test of all the prepared precursors is reported in section 4.6 .

Chapter 5 is intended to recognize the characteristics of the active site reported in the literature. Section 5.1 reports the experimental conditions of simple experiments to generate and characterize nanostructured catalysts. Section 5.2 summarizes the most recent model of active ans selective site. The amounts of nanostructured crystallites as well as their possible relations with the active surface are studied in sections 5.3 and 5.4 .

For a better understanding of the whole contribution, Chapter 6 presents the modifications to the sol-gel synthesis wrapped up in a schematic way (section 6.1). The scheme points the location of each contribution within the body of the dissertation and the conclusions formulated from them, which are stated in section 6.2 . Finally, a summary of the future work to improve the catalytic performance of VPO catalysts is presented in section 6.3 .

Chapter 1 Introduction

1.1 General characteristics of n-butane partial oxidation and vanadium phosphorous oxides

1.1.1 n-butane partial oxidation to maleic anhydride

Maleic anhydride was once produced with benzene as the hydrocarbon source but economical, environmental and safety problems motivated the replacement of benzene by n-butane [3]. The high price of benzene and the abundance of n-butane, the waste of two carbon atoms to transform benzene to maleic anhydride, the byproducts of benzene reaction (phthalic anhydride and benzoquinone) and the classification of benzene as a carcinogen all contributed the switch to partial oxidation of n-butane (Equation 1.1) [4]. The catalytic agent involved in this reaction is a vanadium phosphorous oxide (**VPO**) [3, 4].

$$n-C_4H_{10}+\frac{7}{2}O_2 \xrightarrow{\text{VPO}} C_4H_2O_3+4H_2O$$

Equation 1.1

More than 50% of the global production of MA is consumed by the unsaturated polyester resin industry. Other applications include production of malic and fumaric acids, lubricant additives, copolymers and many others [4, 8].

Several industrial technologies have been developed to supply maleic ahydride consumption which has grown 6-7 % a year to reach 1.5 million metric tons in 2006 [8]. The main differences between these technologies are the type of reactor, type of separation and purification of maleic anhydride, feedstock composition, preparation of the catalysts, promoters of the catalyst and purity of produced maleic anhydride [2].

Parallel and series combustion reactions take place in the reactor, yielding CO and CO_2 as the main byproducts. Thus, improvements to the process have been oriented to increase the selectivity at high levels of conversion, to modify the reaction patterns (fixed or fluidized beds), and to modify the catalysts.

The partial oxidation of n-butane to maleic anhydride is a very complex reaction involving 14 electrons while removing 8 hydrogen atoms and inserting 3 oxygen atoms into the

4-carbon chain [9]. In the literature, two major groups of mechanisms are proposed, the alkenyl mechanism and the alkoxide mechanism [10]. The first mechanism has been reported by Cavani and Trifirò [11]and is reproduced in Equation 1.2 from Hutchings et al. [10]

$$n-C_4H_{10}+O^* \rightarrow 1-C_4H_8+H_2O$$
$$1-C_4H_8+O^* \rightarrow 1,3-C_4H_6+H_2O$$
$$1,3-C_4H_6+O^* \rightarrow C_4H_6O$$
$$C_4H_6O+4O^* \rightarrow C_4H_2O_3+2H_2O$$

Equation 1.2

The necessity of activated oxygen (O^*) in all the steps should be noted, suggesting the importance of the adsorption and diffusion process of oxygen species on the catalysts surface. The formation of the olefins from n-butane has been described in detail in the literature, and it has been generally accepted [12]. However, the transformation of the unsaturated hydrocarbons into maleic anhydride has been a matter of considerable debate. In the alkenyl mechanism, elementary steps in the transformation of 2,5-dihydrofuran to maleic anhydride were proposed based on experimental [2, 11] and theoretical evidence [9, 13, 14]. Trifiró and collaborators proposed the allylic hydrogen abstraction to convert the 2,5-dihydrofuran to furan [2, 11]. This furan can then be transformed directly to maleic anhydride through an electrophilic attack-deprotonization sequence called electrophillic oxygen insertion [9, 11] or through another intermediate, 2 (5H) furanone, [15]. Formation of 2 (5H) furanone from 2,5-dihydrofuran and without a furan intermediate was proposed based on theoretical studies [13, 14].

The presence of 2,5-dihydrofuran (C_4H_6O) as an intermediate has been argued by the proposal of the consecutive alkoxide mechanism reported by Hutchings et al. [10] and backed by Xue and Schrader [16]. These researchers proposed a mechanism involving unsaturated non-cyclic compounds, such as 2-butene-1,4-dial ($C_4H_4O_2$) produced from the unsaturated hydrocarbons as shown in the second reaction of Equation 1.3.

$$n-C_4H_{10}+O^* \rightarrow 2-C_4H_8+H_2O$$
$$2-C_4H_8+4O^* \rightarrow C_4H_4O_2+2H_2O$$
$$C_4H_4O_2+2O^* \rightarrow C_4H_2O_3+H_2O$$

Equation 1.3

The alkoxide mechanism begins with the allylic oxidation of the olefins towards methyl vinyl ketone and 2-butenal [11, 15, 16]. Xue and Schrader suggested the formation of the 2-butene-1,4-dial from the ketones, and it is subsequently converted into maleic anhydride [16].

Additionally, in their work Xue and Schrader proposed that furan-related compounds (cyclic) proposed by the alkoxide mechanism can also generate 2-butene-1,4-dial and other non-cyclic C_4 compounds (which are intermediate compounds in the alkenyl mechanism), adding a set of reactions that can connect the two mechanisms [16]. This implies that the mechanism of the n-butane partial oxidation is extremely complex, since steps in Equation 1.2 and Equation 1.3 can be broken into a very large system of bimolecular elementary reactions that together can generate several possible reaction pathways.

1.1.2 Vanadium phosphorous oxides involved in partial oxidation of n-butane

All commercial processes use a crystalline compound named vanadyl pyrophosphate, $(VO)_2P_2O_7$, as the catalyst. Vanadyl pyrophosphate is prepared from the thermal treatment of another crystalline compound, the precursor $VOHPO_4 \bullet 0.5H_2O$. The most recent and common commercial formulations for the preparation of the precursor prefer organic compounds as solvents [2]. The crystalline structure and the morphology of the crystallites have been determined with a combination of X-ray diffraction and electron (scanning and transmission) microscopy techniques [1] and are shown in Figure 1.1 for the precursor and in Figure 1.2 for the active phase .

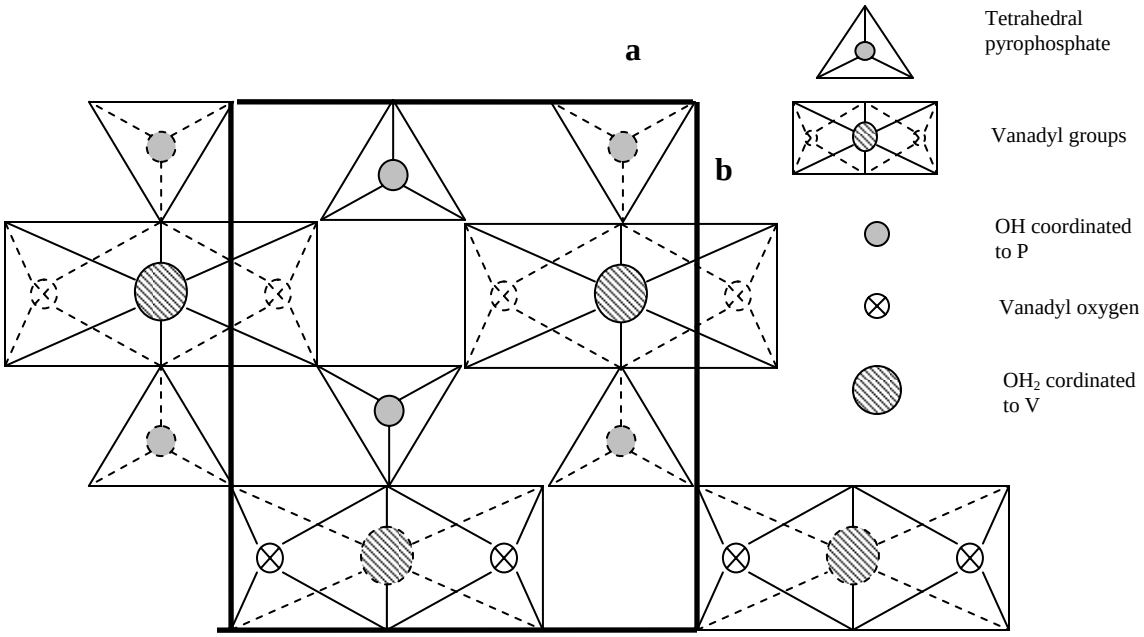

Figure 1.1 Idealized structure of (001) plane of $VOHPO_4 \bullet 0.5H_2O$, schematic representations of vanadium, phosphorous and oxygen atoms (except vanadyl oxygen) were omitted for simplicity, a and b indicate the cell dimensions [1]

The transformation of the precursor into the activated pyrophosphate drastically influences the catalytic behavior of these materials [4]. However, this is not the only transformations that can occur during the activation process. Several crystalline vanadium phosphorous oxides have been reported by the literature, which can undergo different transformations due to the remarkable redox characteristics of vanadium [1]. The most significant ones for the transformation are $VOPO_4 \bullet 2H_2O$ (dihydrate), α_I-$VOPO_4$, α_{II}-$VOPO_4$, β-$VOPO_4$ and δ-$VOPO_4$. All of these are vanadium compounds with a 5^+ oxidation state. The conditions of the activation determine which compounds are formed. Certain levels of temperature and types of activation gas can yield non-selective materials and the changes are summarized in Figure 1.3 [17].

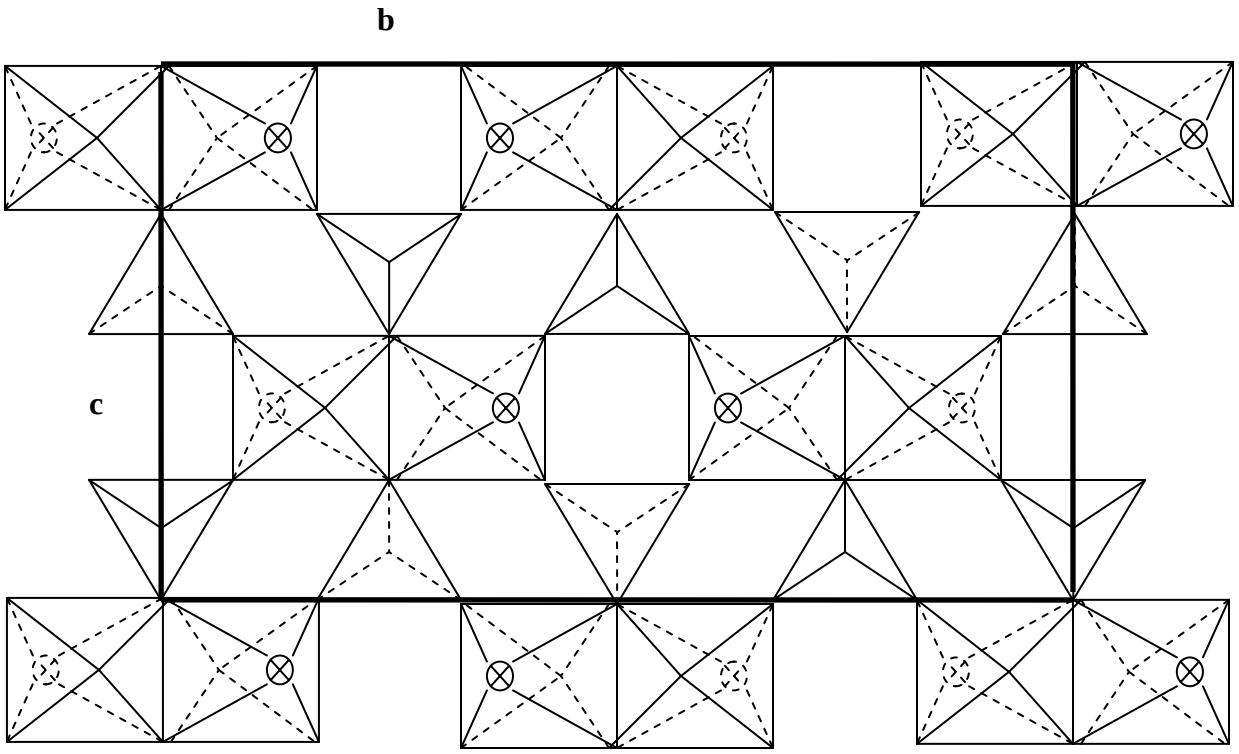

Figure 1.2 Idealized structure of (100) plane of $(VO)_2P_2O_7$, schematic representations of vanadium, phosphorous and oxygen atoms (except vanadyl oxygen, ⊗) were omitted for simplicity. Tetrahedra represent the phosphates and octahedral the vanadyl groups while b and c indicate the cell dimensions [1]

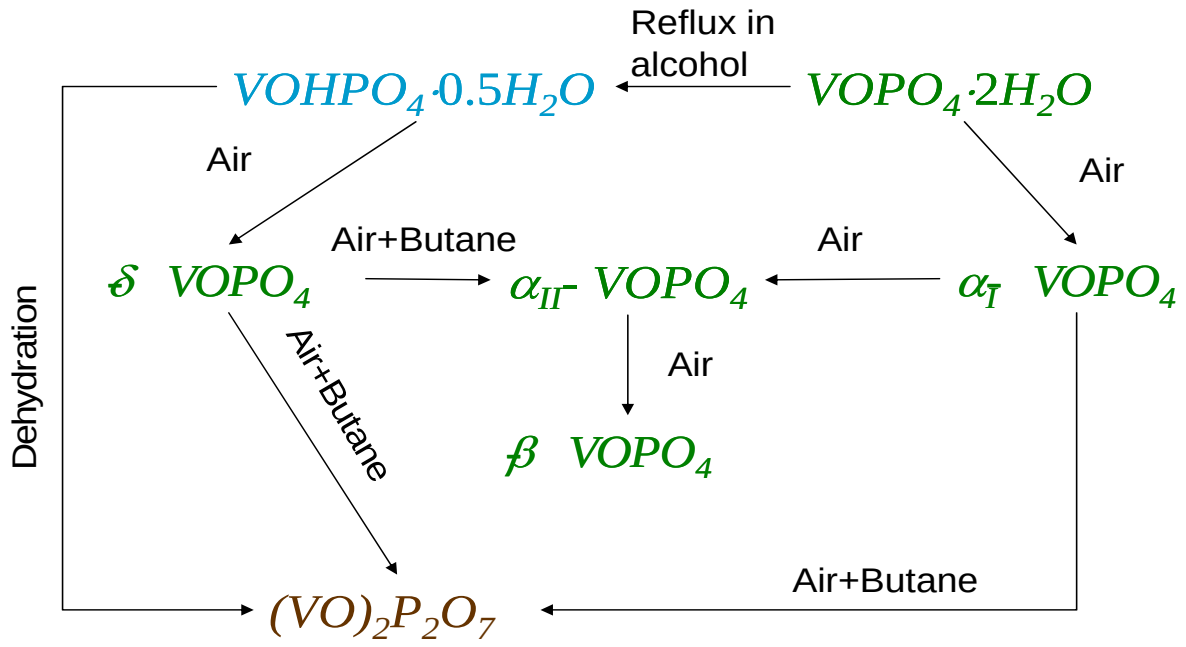

Figure 1.3 Transformation of vanadium phosphorous oxides during the activation process

A starting material could be the dihydrate ($VOPO_4 \bullet 2H_2O$) whose calcination yields α_I-$VOPO_4$. When the reaction mixture is flowed through the material, the active phase can be obtained. However the transformation towards the α_{II} phase and subsequently towards the β phase is possible during the first step. This transformation is detrimental for the activation process since α_{II} and β-$VOPO_4$ are very stable vanadium 5^+ compounds that are difficult to reduce to the active phase. The alternative route is using the hemihyrate as the starting compound. It can be synthesized by reducing the dihydrate in alcohol, after which the precursor can be transformed into the active phase by direct dehydration in an inert atmosphere. The hemihydrate can also be treated in an air stream, and its oxidation yields the δ-$VOPO_4$ phase which subsequently yields both the activated phase and the stable α_{II}, β-$VOPO_4$ under the reaction mixture [17].

1.2 Recent approaches to the improvement of the catalytic performance of V/P oxides

Vanadium phosphorous oxides have been extensively studied since their application as catalysts for the partial oxidation of n-butane in 1966 [10]. The most recent approaches to improve their performances in the catalytic reaction have been summarized in three recent reviews [5, 6, 10] which are also summarized in Table 1.1. Among the approaches reported in Table 1.1, this work focuses on the introduction of novel process in the preparation of the precursor to increase the surface area. Synthesis of small crystallites that keep the necessary morphology and composition characteristics for a good catalytic performance are the goal of the improvement approach.

Table 1.1 Recent approaches to improve the catalytic performance of vanadium phosphorous oxides

Approach	Effect on Physical properties	Effect on Surface activity
Changing the solvents and reducing agents in traditional preparations	The nature of the alcohols for the reduction of V^{5+} to V^{4+} and the sequence in which the source of vanadium and phosphorous were reacted with them (section 1.3.1) allowed to modify the morphology of the hemihydrate. Non-agglomerated platelets were optimum [18]	
Doping the precursor with metal cations in the V/P/O framework	Generally it increased the surface area compared to non-promoted materials [19]	Only Co, Mo and Nb increased the intrinsic activity by stabilizing the amorphous surface and improving its redox properties [19-21]
Introducing novel processes in the preparation of the precursor	Ball milling, Intercalation-exfoliation and precipitation in presence of surfactants increased the surface area and controlled the porosity of the catalysts[22-24] (section 1.3.2)	Precipitation in presence of supercritical antisolvents generated amorphous phases with improved intrinsic activity [25, 26];
Supporting active material on inert supports	Supporting VPO increased the surface area when β-SiC was employed [27]	Maleic anhydride yield was increased under hydrocarbon-rich conditions since the support helped the heat dissipation [27]
Using polyoxometalates of P,Mo,V and Nb as pyridine salts		Mo^{5+} and Nb^{4+} are reduced stable species under hydrocarbon-rich conditions [28-30]
Using V_2O_4 as a source of		Activated catalysts reached higher intrinsic

reduced V or H_3PO_3 as reducing agent in water to avoid use of organic solvents		activity than those traditionally prepared having the same surface area due to an appropriate V^{4+}/V^{5+} ratio on the surface[31]
Increasing n-butane concentration to obtain better productivity	Under this conditions it was found that rosette-like morphology is better for the selectivity than platelet due to its redox characteristics [32]	Low selectivity resulted in carbon accumulation due to the restricted availability of oxygen which promotes the presence of V^{3+} phases [33, 34] and formation of heavy anhydrides was observed[35]
Using membrane reactors to gradually deliver oxygen from a stream rich on it.		Use of n-butane/oxygen ratios higher than the flammability level was possible without affecting selectivity [36-39]

1.3 Preparation of vanadium phosphorous oxides

The present work has focused in the improvement of the catalytic behavior of vanadyl pyrophosphate by increasing the surface area of its precursor $VOHPO_4 \bullet 0.5H_2O$. To increase the surface area of this hemihydrate, a sol-gel process was employed as the synthesis method. In the following sections, the most traditional preparations, the procedures intended to generate high surface area materials, and the fundamentals of the sol-gel synthesis are briefly described.

1.3.1 Traditional preparation methods

The preparation of vanadium phosphorous oxides drastically influences the compounds present in the final activated phases and subsequently their performance in the partial oxidation reaction. Three main methods were summarized by Hutchings, and they were called VPA, VPO and VPD. All of them lead to the synthesis of the precursor, and they are represented in Equation 1.4, Equation 1.5 and Equation 1.6 respectively [5].

$$VPA: V_2O_5 + HCl \rightarrow V^{4+}$$
$$V^{4+} + H_3PO_4 \rightarrow VOHPO_4 \bullet 0.5H_2O$$

Equation 1.4

$$VPO: V_2O_5 + H_3PO_4 + alcohol \rightarrow VOHPO_4 \bullet 0.5H_2O$$

Equation 1.5

$$VPD: V_2O_5 + H_3PO_4 \rightarrow VOPO_4 \bullet 2H_2O$$
$$VOPO_4 \bullet 2H_2O + alcohol \rightarrow VOHPO_4 \bullet 0.5H_2O$$

Equation 1.6

After the activation of the precursors, Hutchings reported a direct linear relationship between the specific butane conversion (in moles per gram per hour) and the surface area for each of the three preparations: the higher the surface area the higher the activity. This observation allowed the researcher to suggest that there is only one reason for VPO and VPD catalysts to be more active: they have higher surface areas than VPA. Consequently it is suggested that their surface is similar in nature [5].

However, Hutchings' research work also demonstrated that the bulk compositions of the activated materials are very different: VPA product is comprised mainly of crystalline $VOPO_4$

phases, VPO product is comprised of mainly vanadium 5^+ compounds along with $(VO)_2P_2O_7$, and VPD product is comprised of mainly crystalline pyrophosphate [5]. It can be noticed that the preparation method influences important aspects for the catalytic activity of the material, such as the surface area and the composition.

1.3.2 Preparation of high surface area vanadium phosphorous oxides

As noted above, a higher surface area results in more active catalysts. A classic approach to achieve such a high surface area as expressed in section 1.2 is ball milling of the precursor. With this technique, the surface area of the active phase was 40 m^2/g compared to values of 3-11 m^2/g obtained with the traditional preparations [40, 41]. A more recent approach reached values of up to 41 m^2/g when intercalation of primary alcohols and subsequent exfoliation were applied to $VOPO_4 \cdot 2H_2O$ (a vanadium (V) phase) [42]. Carreon et al. reported the synthesis of mesoporous VPO with surface areas as high as 250 m^2/g; however, this material was not stable during butane oxidation [5, 6, 24]. Carreon and Guliants obtained the active phase with a surface area of up to 44 m^2/g by using polystyrene spheres as templates to generate macroporous materials [43]. The highest value of surface area has been 400 m^2/g, which was obtained by spreading the layers of $VOPO_4 \cdot 2H_2O$ apart with amine intercalation. These were denominated nickel pillared vanadyl phosphates [44]. Particle morphology and size are also important issues for the activity of the catalytic materials (they are directly related to its surface area) since small crystallites with exposure of the (100) plane are considered more selective [9, 22]. Therefore, synthetic routes that can be oriented to the manipulation of the precursor morphology, crystallite size and surface area are candidates to yield an improved catalyst.

1.3.3 Sol-gel synthesis

The alkoxide method is a particular case of a sol-gel process which has been widely employed to synthesize nanostructured materials having high surface areas. By resorting to this method, high purity and very homogeneous oxides can be obtained at low temperatures [7]. It takes advantage of the highly electronegative alkoxygroups attached to the metal atom which generate a positive charge suitable to be attacked by a nucleophilic group such as water, Figure 1.4 .

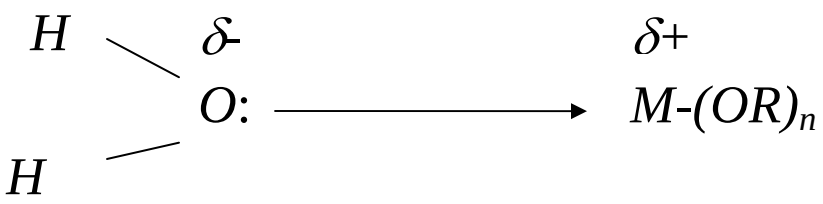

Figure 1.4 Nucleophilic attack of water on the metal center in a metal alkoxide (*M-(OR)$_n$*) where *M:* metal and *R:* alkyl group

After the nucleophilic attack, the hydrolysis is completed with the transfer of a proton from water and the subsequent departure of the alkyl group as alcohol. Equation 1.7 shows this partial hydrolysis reaction [7].

$$M(OR)_x + mH_2O \rightarrow M(OR)_{x-m}(OH)_m + mROH$$

Equation 1.7

To complete this inorganic polymerization, two molecules of the partially hydrolyzed alkoxide can react through their hydroxyl group, producing water as byproduct according to Equation 1.8 [7].

$$2M(OR)_{x-m}(OH)_m \rightarrow \left[(OH)_{m-1}(OR)_{x-m}M\right]_2O + H_2O$$

Equation 1.8

Alternatively, the polymerization can propagate by hydrolyzing the alkoxyl groups with one of the hydroxyl groups of the partially hydrolyzed alkoxide, as shown in Equation 1.9 [7].

$$2M(OR)_{x-m}(OH)_m \rightarrow (OH)_{m-1}(OR)_{x-m}M - O - M(OR)_{x-m-1}\left(OH\right)_m + ROH$$

Equation 1.9

In general, any negatively charged species can perform the nucleophilic substitution; thus, acidic compounds (such as acetic acid in Equation 1.10) can be employed [7].

$$\equiv MOR + CH_3COOH \rightarrow \equiv MOCOCH_3 + ROH$$

Equation 1.10

For the synthesis of vanadium phosphorous oxides, the starting hydrolysis reaction can be carried out by using phosphoric acid as the hydrolyzing agent of a vanadium alkoxide to obtain a partially hydrolyzed compound containing the V-O-P bonds which are characteristic of the catalysts, Equation 1.11.

$$VO(OR)_3 + PO(OH)_3 \rightarrow VO(OR)_2 OPO(OH)_2 + ROH$$

Equation 1.11

The products of this reaction condensate to yield solid three-dimensional networks whose pores are filled with solvent (gels). Removing the solvent by evaporation collapses the pores due to the high surface tension present in the vapor-liquid interface that is applied to the fragile gel structure. Therefore, it's been established that avoiding the coexistence of vapor and liquid phases during the drying can contribute to maintain the porous structure. To avoid a vapor-liquid interface the drying process can be carried out at pressure and temperature higher than the critical point of the substance acting as the solvent [45].

Chapter 2 Sol-gel synthesis of $VOHPO_4 \bullet 0.5H_2O$

The metal alkoxide method (MAM) is one of the most commonly used sol-gel procedures. Metal alkoxides undergo hydrolysis and condensation to obtain colloidal gels whose structural characteristics can be controlled. High surface area metal oxides are produced from this gel following an appropriate drying process [7]. Thus, the MAM is a likely candidate for synthesis of an improved precursor. The application of the MAM to vanadium phosphorous oxides has shown that reactions in aprotic solvents and in the absence of water lead to the formation of small and compact particles [46]. Other studies showed that the active phase could be synthesized through a sol-gel procedure and explored the application of colloidal and polymeric gelation to form membrane reactors [47]. Methods that involve the use of proton exchange resin are also reported in the synthesis of $VOPO_4 \bullet 2H_2O$ [48].

2.1 Experimental

2.1.1 Synthesis of the precursors

As a reference material for the catalytic evaluation, the precursor was prepared according to one of the traditional methods [22]. The procedure comprises the reduction of V_2O_5 with a mixture of alcohols (isobutyl and benzyl alcohol) and the addition of the phosphoric acid, 85% (Fisher) (VPO method in section 1.3.1). The sol-gel procedure was based on the methodology reported by Ennacciri et al [49]. Two 1M solutions were prepared: (i) vanadium (V) triisopropoxide oxide (the alkoxide) (Alfa-Aesar) in tetrahydrofuran (THF) (Fisher) and (ii) orthophosphoric acid, anhydrous solid (Fluka), in THF (Fisher). Equal volumes (10 mL) of each solution were mixed. The phosphoric acid solution (ii) was added to the alkoxide solution (i) while stirring. The gel was reacted for three hours and the final slurry was dried according to the procedure described below.

2.1.2 Drying process

As a control procedure, the yellow slurry was dried under nitrogen at atmospheric pressure for four hours. This material will be referred to as atmospheric drying (AD). To dry the materials under high pressure, a reported procedure was followed [50]. The slurry was poured into a glass-lined 600-mL Parr reactor. The reactor was pressurized with nitrogen to 7.9 bars and heated from 25°C to 265°C at a rate of 1°C/min. After ten minutes at the maximum temperature, the reactor was vented. In order to reach the critical point and avoid the collapse of the fragile gel, solvent was added before the slurry was poured into the autoclave [45]. To determine the influence of the amount of added solvent in the final product, an experiment with a completely randomized design [51] was carried out with three levels or treatments: adding 20 mL, 50 mL or 100 mL (low, medium and high level, respectively) of THF. The resultant materials were referred to as LS, MS and HS respectively. Three replications were performed for each level.

2.1.3 Characterization

Diffuse reflectance infrared Fourier transform spectroscopy (DRIFTS) was done with a Thermo Nicolet Nexus™ 670 FT-IR spectrophotometer equipped with a Smart Collector. The samples were diluted to 1-10 weight % in infrared-grade potassium bromide (Acros). X-ray diffraction (XRD) was carried out with a Bruker axs D8 advance diffractometer that was set at 40 kV and 40 mA. Scans were from 5° to 70° (2θ) and with a step size of 0.05°. The diffractometer radiation was copper Kα (wavelength λ=1.54Å). The sample was put on the sample holder and exposed to the atmosphere at room temperature during the analysis. The scanning electron micrographs (SEM) were taken with a Hitachi S-3500N. The oxidation state of the vanadium in the samples was determined with the volumetric method reported in the literature [52].

The surface areas of the samples were determined by an Altamira instruments AMI-200 according to the BET model and using a flow procedure [53]. The procedure consists of flowing precisely blended mixtures of nitrogen and helium over the solid sample until equilibrated flow is reached. The cell containing the sample is immersed in liquid nitrogen to condense nitrogen from the flowing mixture on the sample surface. The temporary change in nitrogen concentration in the flowing mixture is detected by a thermal conductivity detector (TCD) as a signal peak. The procedure is carried out with streams containing different nitrogen/helium ratios. Data from peak

areas at different nitrogen partial pressures was fit to the BET model to find surface area [53]. The procedure is recommended for mesoporous materials (pore diameter > 20nm) since microporous materials require degassing procedures [53]. Nanostructured vanadyl pyrophosphate has been reported as a mesoporous material [54], which make the procedure a suitable characterization technique for the present work.

2.2 Alkoxide method in tetrahydrofuran

The sol-gel procedure resulted in an immediate gelation process, and an orange gel was observed. At this point, stirring using a magnetic stir bar was not possible due to the high viscosity of the solution. After three hours of reacting, the mixture turned into bright yellow slurry. The surface area of the slurry following atmospheric drying (AD) is 56 m^2/g. The DRIFTS spectrum of this sample is shown in Figure 2.1, and the comparison with other reference materials is shown in Table 2.1

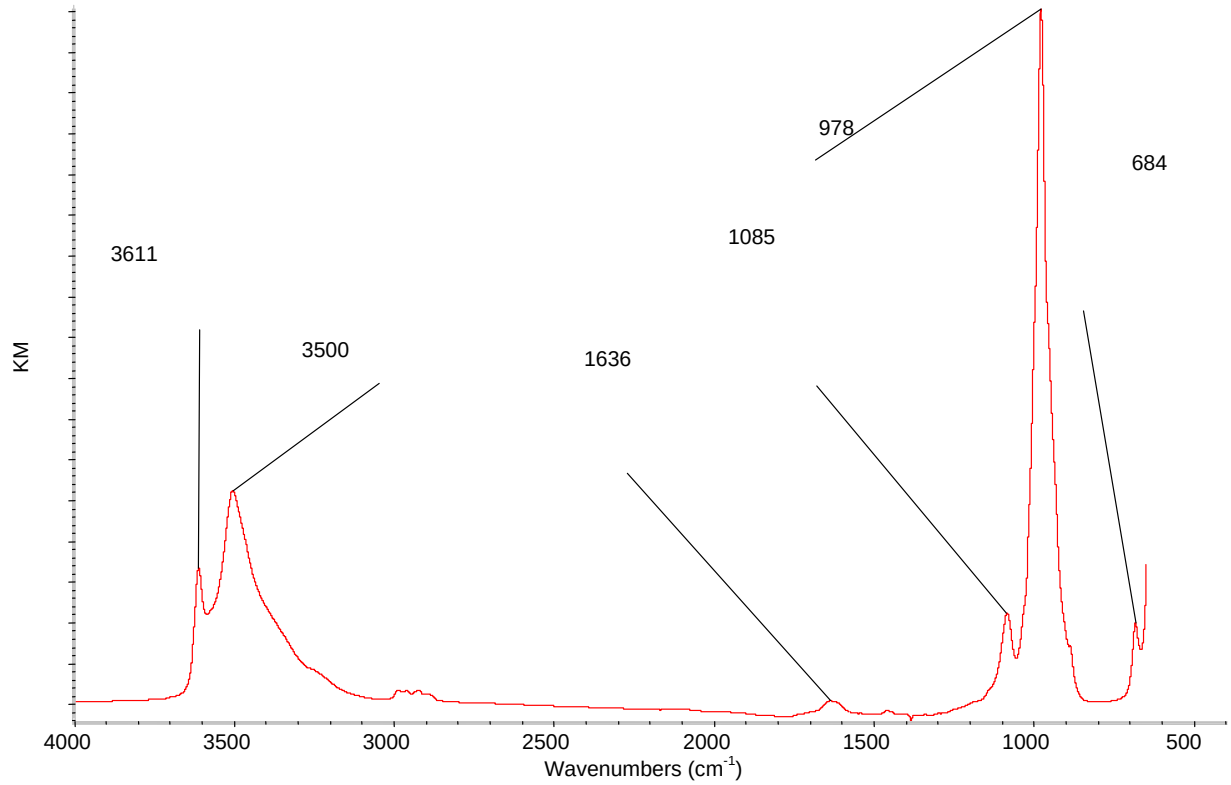

Figure 2.1 DRIFTS spectrum of VPO slurry in THF after drying in a stream of nitrogen

All of the vibrations of $VOPO_4 \bullet 2H_2O$ are present [48]. However, some of the bands present in AD, especially the weak ones (2993 cm^{-1}, 2893 cm^{-1}, 1460 cm^{-1} and 1364 cm^{-1}, which

are not pointed in Figure 2.1) are not related to any of the vanadium phosphates. These bands are attributed to intercalated compounds as discussed below.

Table 2.1 DRIFTS bands (wavenumbers in cm^{-1}) of atmospheric dried slurry

Reference Compounds			This work	Assignment [48, 55]
R1[a]	THF	R2[b]	AD	
		3620	3611	ν(OH)
		3580	3500	ν(OH)
2993	2993		2993	ν(C-H)
2893	2893		2893	ν(C-H)
1464	1460		1460	δ(C-H)
		1625	1636	δ(H-O-H)
	1364		1364	ν(C-O)
		1088	1085	ν_{as}(P-O)
		1000	978	ν(V=O)
		913	911	ν(P-O)
		685	684	δ(V-OH)orδ(P-OH)

[a] 2-Propanol

[b] $VOPO_4 \cdot 2H_2O$

The X-ray diffraction pattern of AD, Figure 2.2, shows the presence of many of the typical reflections of α-$VOPO_4$ as well as some of the reflections of $VOPO_4 \bullet 2H_2O$ [1]. Table 2.2 compares the spacing and intensity of these referenced compounds with the AD . However, there are other very intense reflections at 8.71Å, 5.03Å and 2.91Å that are not characteristic of any of the most well known VPO phases. These reflections are attributed to the intercalation of either solvent or isopropyl alcohol. Okuhara and coworkers recently explored the phenomena of exfoliation by means of intercalating alcohols into the layers of $VOPO_4 \bullet 2H_2O$. The process was carried out for three hours at relatively low temperatures (30-70°C) and the subsequent reduction of the exfoliated VPO by primary alcohols yielded the precursor [42, 56]. Previous works employed alkylphosphonic acid that reacted with V_2O_5 to intercalate the corresponding alkyl groups and intercalated pyridine into $VOPO_4 \bullet 2H_2O$ by reflux [57, 58].

Table 2.2 DRIFTS and XRD analysis for atmospheric dried (AD) slurry

Reference Compounds[1]		This work
R3[c]	R2[b]	AD
		8.71 (100)
	7.45 (vS[d])	7.32 (21.5)
		5.03 (40.9)
4.43 (w[g])		4.41 (35.5)
3.57 (S[e])		3.59 (11.8)
3.07 (vS[d])	3.1 (M[e])	3.07 (83.9)
		2.91 (58.1)
	2.19 (w[g])	2.18 (15.1)
1.9 (S[e])		1.95 (12.9)
1.83 (M[f])		1.87 (14)
1.56 (M[f])	1.55 (S[e])	1.55 (20.4)
1.5 (M[f])	1.52 (S[e])	1.52 (13.4)
1.43 (M[f])	1.46 (M[f])	1.46 (13.8)

[c] $VOPO_4$

[d] Very strong,

[e] strong,

[f] Medium

[g] Weak

Thus, the DRIFTS and XRD patterns in Figure 2.1 and Figure 2.2 show $VOPO_4$ intercalated either with isopropyl alcohol or THF. This possibility is also supported by the presence of weak bands in the DRIFTS spectrum at 2993 cm^{-1} and 2893 cm^{-1} that correspond to C-H stretches of THF or isopropyl alcohol and the remaining weak bands that can be ascribed to these two compounds, Table 2.1. To substantiate that the sample was an intercalated $VOPO_4$, the XRD powder pattern was indexed to obtain the cell parameters. This calculation was done with CELREF software, version 3. A tetragonal cell symmetry was considered, which is the known symmetry of $VOPO_4 \bullet 2H_2O$ and other intercalated compounds [1]. This calculation gave cell parameter values of a=6.158Å and b=8.868 Å. The main (hkl) indices are shown in Figure 2.2. The hard sphere diameter for THF and 2-propanol was estimated according to the methodology reported by Misawa [59] and both are ~4.8 Å. This hard sphere diameter is approximately equal to the subtraction of the b parameter of $VOPO_4$ (4.1 Å [1]) from the b parameter for the powder pattern shown in Figure 2.2 (8.86 Å) which can be interpreted as an association of the

intercalated molecules with each of the oxide layers that bound the intercalation space. This situation has been denominated as interdigitated intercalation, where layers of the alcohol or THF are included into a $VOPO_4$ lamellar structure [60]. Even though THF was not considered as an exfoliation agent, THF or isopropyl alcohol could act as donor reagents, intercalating the solid layers by donating electrons to the vanadium(V). At this time, it is not known whether THF or isopropyl alcohol is the intercalated molecule.

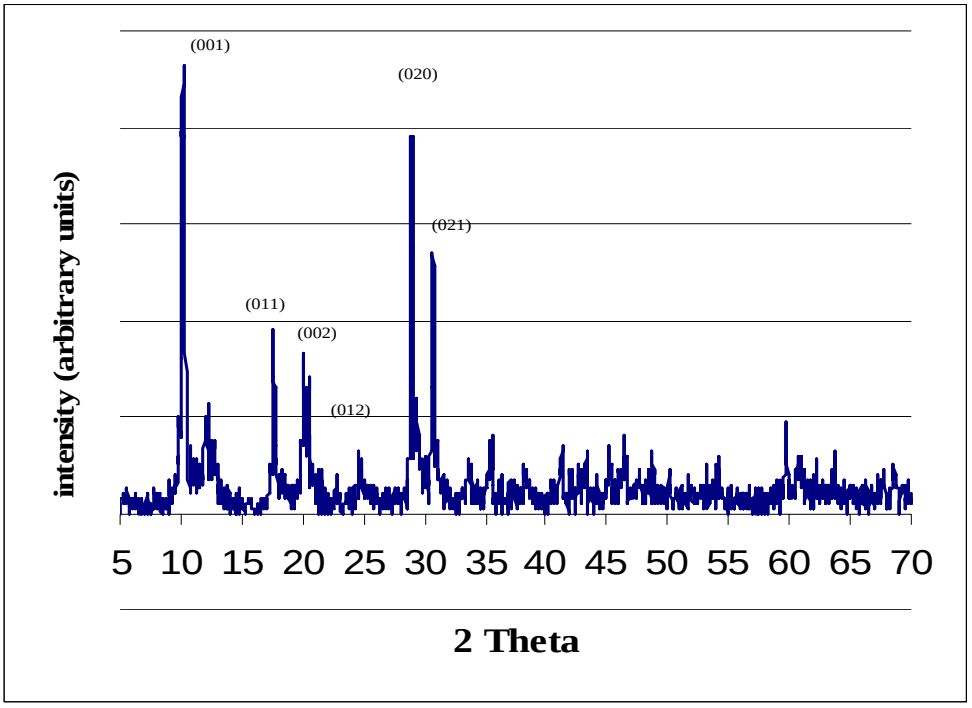

Figure 2.2 XRD pattern of VPO slurry after drying in a stream of nitrogen

2.3 Autoclave drying

The drying process can be carried out by evaporation or by the well known supercritical drying [45]. During the evaporation process the gel structure is affected by the high surface tension present in the liquid-gas interface. The very small pores of the gel are initially filled with liquid. As the liquid is vaporized, the walls of the pores cannot resist the applied force and collapse. This significantly damages the gel structure, increases the particle size and reduces the surface area [61]. This problem can be avoided if the evaporation process is carried out close to the critical point of the solvent where there is no surface tension [45, 61]. The process is carried

out in an autoclave and an appropriate excess of solvent is added to reach the critical point before the gel loses the solvent [45]. Several transformations of VPO can occur during this process. Different compositions, morphologies and subsequently different catalytic properties are reported as consequences of the high-pressure synthesis of VPO [62-64].

2.3.1 Pressure-temperature diagram during autoclave drying

The pressure in the autoclave was measured for three levels of solvent (20 mL 50 mL, and 100 mL) as a function of temperature and is shown in Figure 2.3. For comparison, a curve of the liquid-vapor equilibrium of THF is also plotted as Figure 2.3 a) [65]. When high and medium amount of solvent are added to the slurry before the drying step, the system develops a behavior similar to the vapor-liquid equilibrium of pure solvent, and the liquid vaporizes very close to the critical point. In contrast, when a low amount of solvent is added, the liquid completely vaporizes at relatively low temperatures and never reaches the critical point.

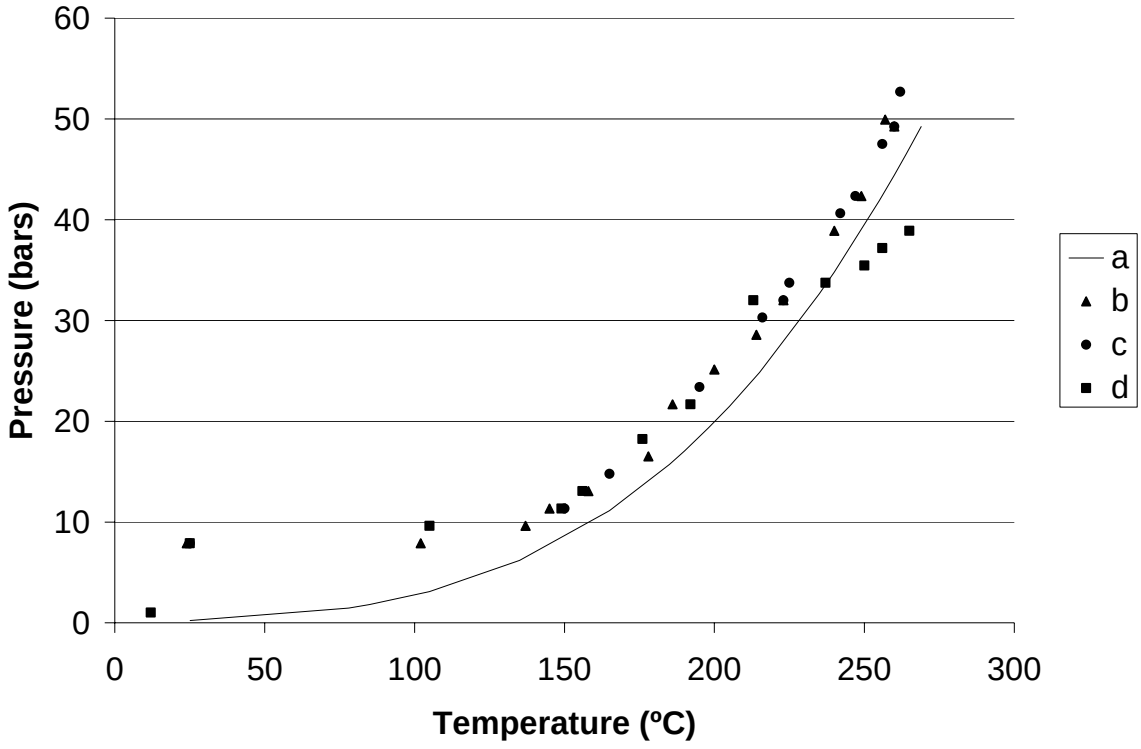

Figure 2.3 Pressure-temperature behavior during the autoclave drying compared with the vapor pressure of THF. a) Vapor pressure of pure THF b) High amount of solvent (100 mL) c) Medium amount of solvent (50 mL) d) Low amount of solvent (20 mL).

2.3.2 Morphology of precursor crystallites

The morphology of the particles is strongly affected by the type of drying. Figure 2.4 shows that high pressure drying yields platelets while atmospheric pressure drying yields spherical particles (the morphology of the atmospheric-dried samples is in agreement with literature [49]). Among the high pressure treatments, LS produced larger particles and there is not a significant difference between MS and HS. The morphology of LS is typical of the precursor with phosphorous/vanadium ratios close to one [22]. Thus, in the autoclave drying, the amount of added solvent influences the conditions where it is completely vaporized [45] and influences the final size and morphology. An additional and interesting aspect is that the observed morphology of the particles after the drying step is very similar of those obtained by Okuhara and coworkers [42], but have a smaller particle size. Their claims include the formation of platelets of the reduced compounds with particle sizes of 500-6000 nm in length and 69-156 nm in thickness (calculated from surface area measurements). The reduced compounds shown in Figure 2.4 b) and c) are approximately 400 nm in length and the length of crystallites in Figure 2.4 a) is 500 nm. For LS, MS and HS precursors the thickness of crystallites was not calculated from surface area data due to the impurity (non-complete reduction) of samples (see discussion in section 4.2.2).

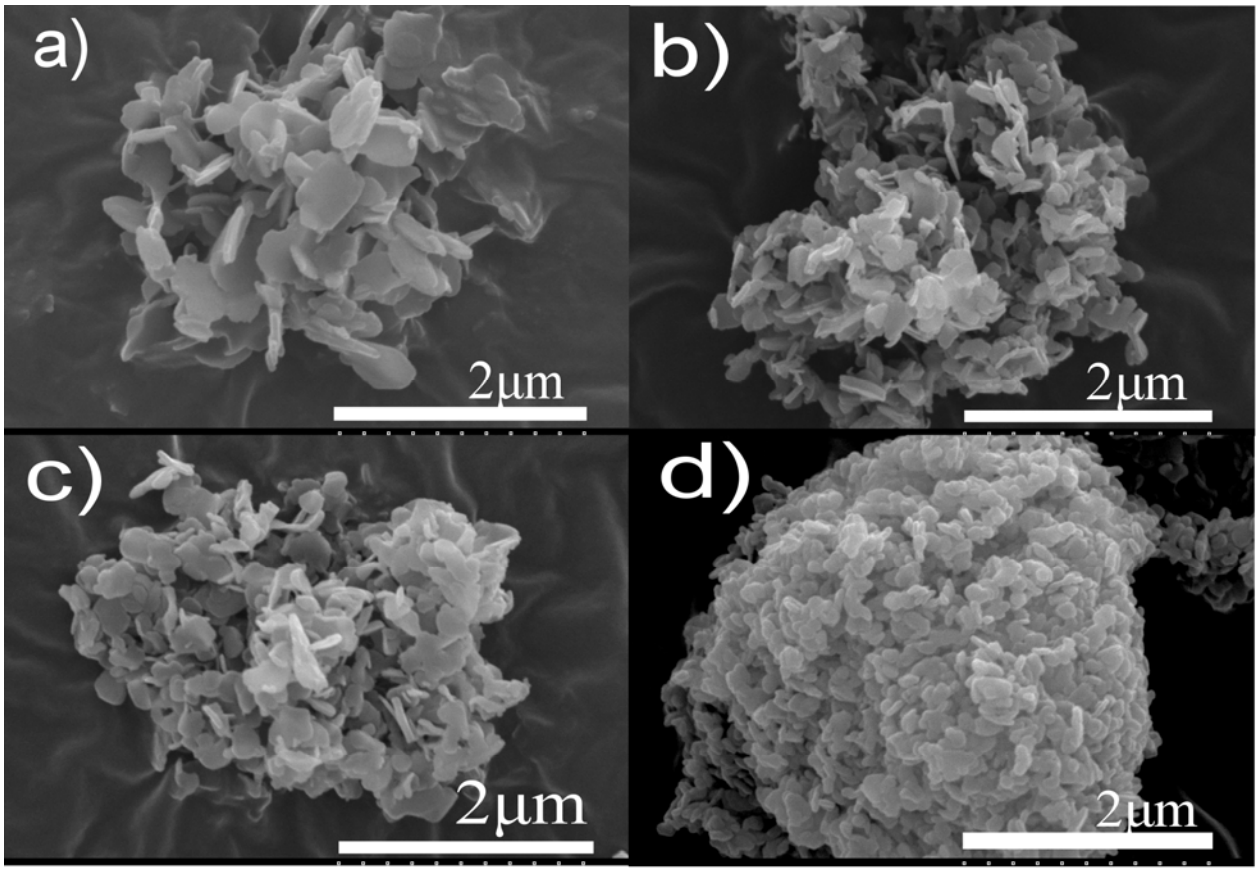

Figure 2.4 Scanning electron micrographs (SEM) of precursors prepared with the alkoxide method and a) Autoclave drying, low amount of solvent b) Autoclave drying, medium amount of solvent c) Autoclave drying, high amount of solvent and d) Atmospheric drying

2.3.3 Surface area measurements of precursors

The surface areas of all autoclave-prepared precursors are 65, 103 and 121 m^2/g for low solvent, medium solvent, and high solvent respectively and the influence of the amount of added solvent in this parameter is evident. The values are also higher than the results reported by Ennaciri for atmospheric pressure drying in air [49]. The analysis of variance for the experiment with the three levels of solvent results in the conclusion that there is no difference between MS and HS, but LS is different from the average HS and MS. The Bonfferoni t test was used to compare the means [51]. These results indicate that vaporization of the solvent during drying before the critical point leads to a dramatic loss of surface area.

2.3.4 Reduction inside the autoclave

Infrared spectra and X-ray diffraction patterns were obtained for the materials dried with different amounts of solvent. These spectra, along with reference spectra, are shown in Figure 2.5. a) and e) are DRIFTS fingerprints of $VOPO_4$ compounds shown in Figure 2.1 and the precursor, respectively [48, 55]. b) to d) show the evolution of spectra from $VOPO_4$ towards the precursor when the amount of added solvent is decreased. Bands at 1054 cm^{-1}, 977 cm^{-1} and 1196 cm^{-1} appear in b), then 1104 cm^{-1} and 932 cm^{-1} are added in c) and finally 1133 cm^{-1} band shows up in d) to complete the six characteristic bands of the fingerprint spectra of the precursor. These spectra are very similar to those reported by Kamiya et al. for exfoliated-reduced $VOPO_4 \bullet 2H_2O$ [42] The amount of added solvent in the three cases influences the chemical composition of the final materials.

Similarly, Figure 2.6 a) and e) are X-ray diffraction patterns of the $VOPO_4$ phase shown in Figure 2.2 and the precursor, respectively [1]. In Figure 2.6 b) the reflections at 5.67Å and 2.91Å appear as the first sign of the presence of the hemihydrate. Figure 2.6 c) is mostly equal to a), however the peak at 4.5Å can be also observed and is associated with the main reflection of the hemihydrate (4.53 Å). Figure 2.6 d) is the closest pattern to e) since it contains additional reflections at 3.64 Å, 3.08Å, 2.77Å, 2.59Å, 2.39Å, 1.89Å and 1.84Å. Thus the crystallography of the resultant materials evidences the transformation of the yellow slurry into a compound that can be identified as the precursor.

These results show that in addition to the physical changes that occur during autoclave drying, chemical transformations also occur. Interestingly, while HS and MS had nearly the same surface area, they have quite different phase compositions. This suggests that the differences in surface area for these materials are not just due to differences in phase composition: the autoclave drying procedure has a substantial role in producing high surface-area vanadium phosphates.

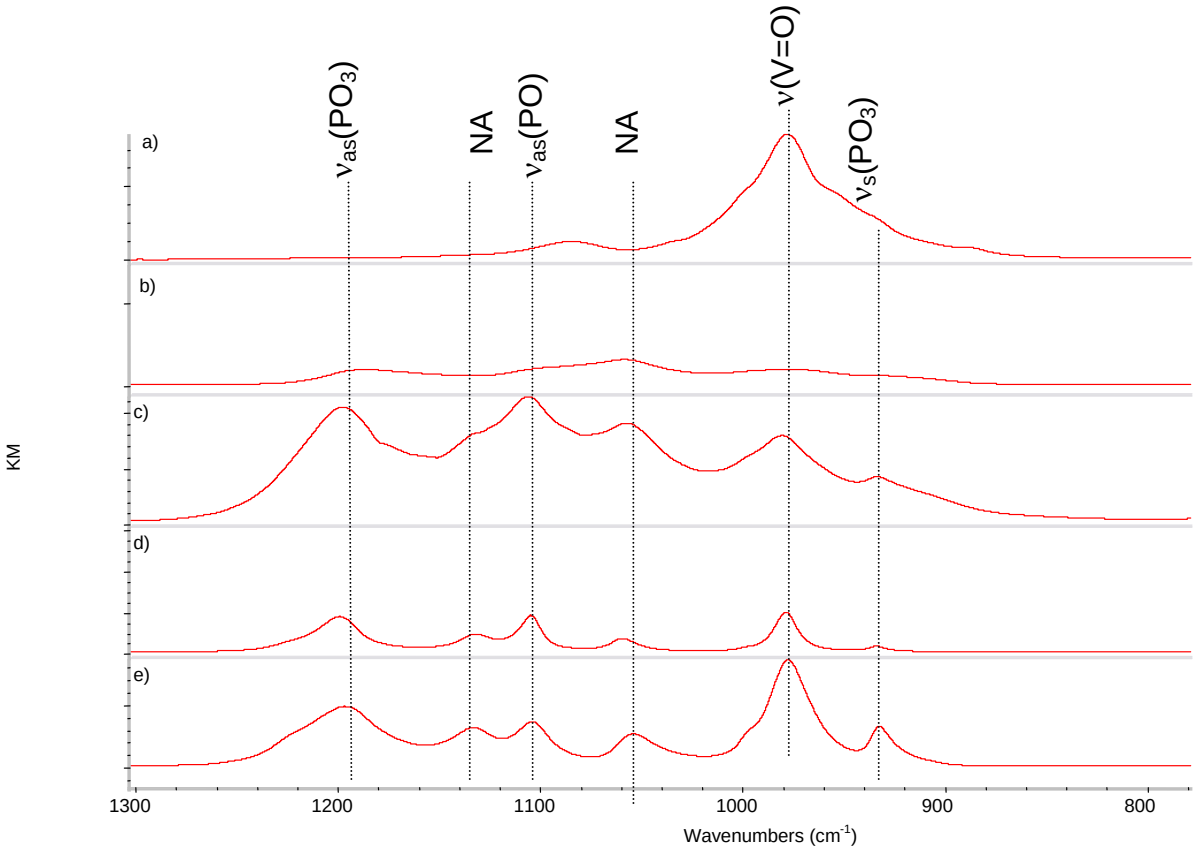

Figure 2.5 DRIFTS spectra of different VPO, (KM: Kubelka-Munk units) a) Slurry dried on nitrogen b) High amount of solvent c) Medium amount of solvent d) Low amount of solvent e) $VOHPO_4 \bullet 0.5H_2O$. NA: Non-assigned band

As discussed in the previous sections, when the material was dried inside the autoclave, chemical transformations occurred, which yielded products containing reduced-vanadium phases. The reduction process can be attributed to the alcohol generated as byproduct during the hydrolysis of the vanadium alkoxides. It is known that alcohols are good reducing agents to prepare the precursor [66]. Reduction of $VOPO_4$ with isopropyl alcohol and other alcohols has been reported to yield non-agglomerated particles with platelet crystalline morphology as a result of the reduction of $VOPO_4$ [22]; this is in agreement with the trend seen in Figure 2.4 a), b) and c). As more solvent was added to the slurry, the concentration of alcohol decreased and less reduced products were obtained. In contrast, a low amount of added solvent resulted in more

reduced phases. As measured through titration, the average oxidation state of the samples decreased with the amount of solvent.

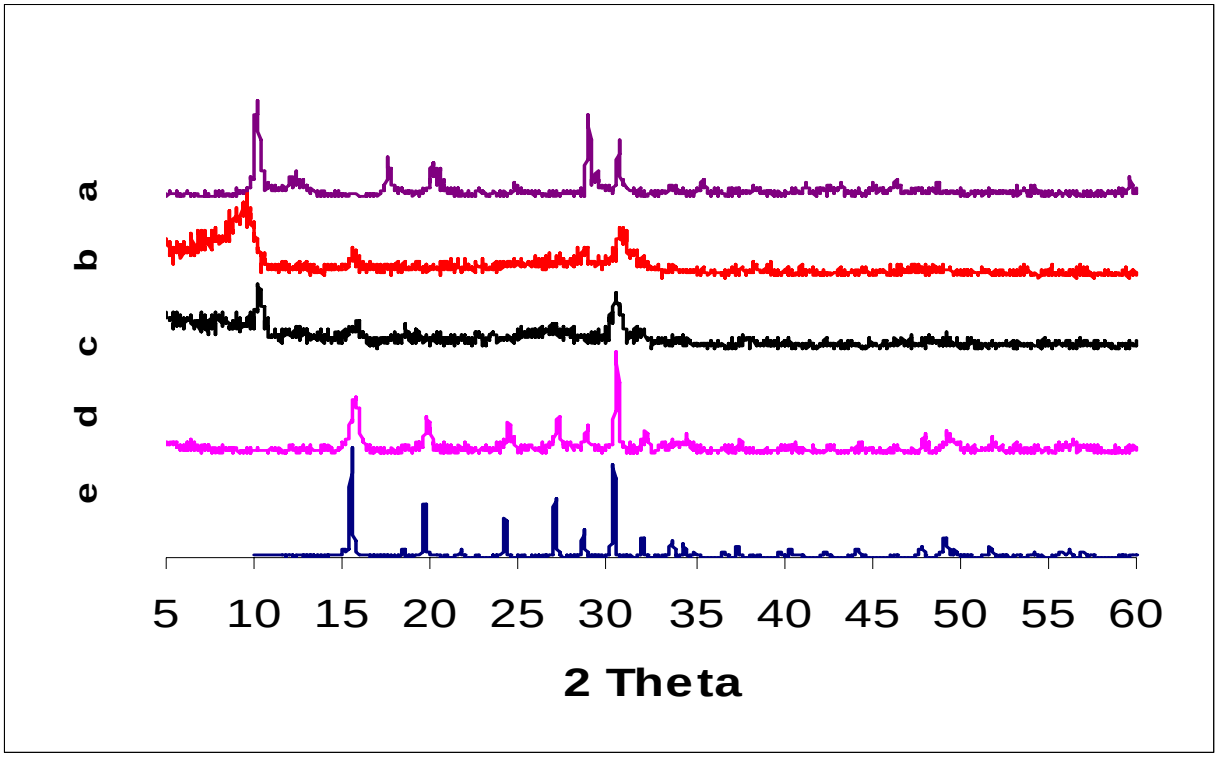

Figure 2.6 XRD patterns of different VPO materials a) Slurry dried on nitrogen b) High amount of solvent c) Medium amount of solvent d) Low amount of solvent e) $VOHPO_4 \bullet 0.5H_2O$

Chapter 3 Evaluation of sol-gel prepared precursor in the partial oxidation of n-butane

Transformation from the precursor to the active phase is topotactic; the (001) plane on the former transforms into the (100) in the latter [1]. Thus, the morphology of the precursor plays an important role on the catalytic activity of the active phase [22]. In their work Horowitz et al. reduced $VOPO_4$ to the precursor by secondary or primary alcohols. It was found that the type of alcohol dramatically influenced the morphology of the particles and consequently their catalytic activity [22]. The size of the crystallite has been demonstrated to affect the catalytic activity of VPO. Small crystallites of the precursor yielded small crystallites of the active phase and were reported as highly selective for the partial oxidation of butane to maleic anhydride [17, 54, 67]. Those small active crystallites are thought to form when the precursor crystallites break apart [68].

Several papers have evaluated the catalytic activity of precursors prepared from the exfoliation-reduction of $VOPO_4 \bullet 2H_2O$. We summarize some of the most relevant results from those works as follows. An exfoliated-reduced precursor in 1-butanol yielded an active phase with 3000 nm crystallite size that gave 53 % selectivity to maleic anhydride at a conversion of 50 % at 430°C [42]. When 2-butanol was used as the exfoliating-reducing agent, the active phase with 800 nm crystallites was 75% selective at 50% conversion at 390°C[17, 67, 68]. Finally, when the materials were exfoliated with a mixture of 2-butanol and ethanol, the active phase with 50 nm crystallites was 82% selective at 50% conversion at 390°C [54]. High pressure and temperature preparations also yielded active catalysts for the partial oxidation of n-butane. $VOPO_4 \bullet 2H_2O$ was reduced with 1-octanol at 150°C in an autoclave and the resulting material gave 50% selectivity at 39% conversion at 400°C [63]. A precursor prepared by mixing V_2O_5, H_3PO_4, oxalic acid and water in an autoclave at 150°C yielded an activated catalyst with 61% selectivity at 35% conversion at 400°C[69].

3.1 Experimental

3.1.1 General conditions

Precursors LS, MS and HS were evaluated as catalysts for the partial oxidation of butane to maleic anhydride. W/F (weight of catalysts per molar flow of n-butane) was adjusted to 60 g h mol^{-1} for MS and HS (having bulk density up to 0.1 g/mL) and 150 g h mol^{-1} for LS and traditionally prepared precursor (bulk density of 0.18 g/mL and above). This allowed us to keep gas hourly space velocities (GHSV) between 1700 $h^{-1}$and 2200 h^{-1}. The precursors were initially treated under nitrogen from 298 K to 673 K and were kept at this temperature for 2 h. Next, a reacting mixture of 1.7% butane in air was flowed through the catalytic bed. The activated materials were referred to as CLS, CMS and CHS.

3.1.2 Gas chromatography

The products were analyzed with gas chromatography employing a 5Å molecular sieve and a Porapaq QS column. Two samples are simultaneously taken by an injection valve which is kept inside the molecular sieve oven at 100°C. The first sample is carried inside the molecular sieve by helium at a flow rate of 33.4 standard cm^3/min. The molecular sieve column isothermally separates light gases (N_2 O_2 and CO). They are analyzed then with a thermal conductivity detector (TCD). The second sample is carried with another stream of helium through the Porapaq QS column at 52.3 standard cm^3/min to separate the CO_2, n-butane and maleic anhydride. The latter gases are separated with a temperature program that initially held the column at 80°C for 12 minutes, then heats it up to 200°C at 15°C/min and holds it at 200°C for 25 min. CO_2 and n-butane are analyzed with the TCD using N_2 as internal standard; however, the sensitivity of the TCD for maleic anhydride is very low, so a flame ionization detector (FID) was used to quantify the amounts of it in the products stream. The internal standard for the FID was the n-butane since its concentration can be determined with the TCD analysis.

The calibration of the gas chromatograph was based on standard mixtures for light gases, i.e. N_2, CO and CO_2. A mixture of 0.5% molar of H_2, CO, CO_2 and O_2 in N_2 as balance (Scotty®, gas mixture) was used for this calibration. The calibration of n-butane was undertaken with mixtures of 0.75 % and 1.5% of n-butane in air prepared with calibrated mass flow controllers.

Finally, the calibration for maleic anhydride was performed using a saturator. Solid maleic anhydride (Alfa-Aesar) was melted and kept in a water bath at 62°C. A stream of 0.75 % of n-butane in air was bubbled through the melted anhydride for 10 minutes and analyzed with the chromatograph. For each replicate of the calibration, the saturator was cooled down to solidify the maleic anhydride to avoid the fast vaporization and its accumulation inside the lines before the GC. Appendix A contains a table with the calibration factors of the compounds that were obtained.

3.1.3 Experimental design and analysis

The transformation from the precursor to the activated catalyst is an extremely slow process that can last several hundreds of hours [4, 70]. In this study the reaction was carried out for 72 hours in each run. This length was chosen to mirror conditions of most catalytic tests described in the literature [5, 18, 54, 71]. The long conditioning process for the catalyst to reach the equilibrated state reduces the number of samples of each preparation that can be evaluated (less replications). The purpose of this section is to establish an appropriate statistical analysis for the performances of each sample along the 72 hours to render possible the reduction of the error with only two replicates by considering the activation time as an additional factor.

A completely randomized factorial design involving preparation and time as factors, each of them with at least 4 levels (four preparations including the traditional as control and four levels of time 12, 32, 52 and 72 hours) will yield an enormous number of experiments (4 samples per preparation with one replicate would reach 32). The repeated measures design is an interesting alternative to reduce the size of the experiment. It is widely used when the analysis of time tendency in responses is needed and only 8 samples (2 per each preparation) instead of 32 are required [72]. The response variable from each of the 8 samples is observed at 12, 32, 52 and 72 hours of activation.

The analysis of the repeated measures design can be carried out similarly to the so-called split-plot design [72]. Conventional split-plot designs are employed when the size of the experimental units for each factor is required to be different. In the case of the preparation and time experiment, each of the eight samples (called whole-plots) would need to be split in four smaller pieces (called sub-plots) to be treated at each time level. Therefore, this design would require the same 32 observations as the factorial design structure. The difference with the

repeated measures design lies in the fact that the levels of time are not randomly assigned to the split samples since all levels are chronologically evaluated in the same sample. This fact requires the adjustment in the degrees of freedom for the numerator and the denominator for the F statistic in the analysis of variance [72].

The statistical analysis of the results of the catalysts evaluation was performed for both conversion and selectivity as response variables, resorting to the Repeated Measures analysis of variance of the general linear model (GLM) procedure in the available software SAS. Table 3.1 shows the results for selectivity of the eight runs evaluated at the four levels of time. The results evidence that the interaction of time and preparation and time itself don't significantly influence the selectivity. A p-value less than 0.01 indicates that there's more than 99% of probabilities that the variability in the selectivity is due to the different preparations. The p-value in Table 3.1, 0.0096 signifies that at least two of the preparations yield catalysts whose mean selectivity is different from each other.

.

Table 3.1 Repeated Measures analysis of variance of a catalysts evaluation test, response variable: selectivity

Source[a]	DF[b]	SS[c]	MS[d]	F[e]	p-value[f]	Adj G-G[g]	Adj H-F[h]
Preparation	3	3544.9	1181.6	17.1	0.0096		
Error	4	276.4	69.1				
Time	3	336.2	112.1	2.17	0.1443	0.2112	0.166
Time*Preparation	9	208.6	23.2	0.45	0.882	0.7426	0.842
Error (time)	12	619.0	51.5				

[a] of variability

[b] Degrees of freedom

[c] Sum of squares

[d] Mean square

[e] value of the F statistic

[f] probability that the F value is not >1

[g] Green house-Geisser adjusted p-value to account for non-randomly assigned time levels

[h] Huynh-Feldt adjusted p-value to account for non-randomly assigned time levels

Once the influence of the preparation technique is validated, it is necessary to establish the difference between the four preparations and, most important, if any of them is different from the traditional synthetic method (the control). Comparing the means of four preparations is an appropriate methodology to establish the aforementioned differences. Two statistical approaches are available for the comparison: a simple Student test and a multiple comparison test. The student test compares two means; therefore, conclusions drawn from this comparison cannot be simultaneously stated with the conclusions from any other comparison. For instance, traditional preparation yields significantly less selective catalysts than the first sol-gel preparation and the catalysts from the first sol-gel preparation are not significantly different to the second sol-gel preparation. However, from these two statements it is not appropriate to state that the traditional preparation and the second sol-gel preparation are significantly different. To be able to draw accurate general conclusions, the second approach is necessary. Multiple comparisons using the Bonferoni *t* test or the Dunnet *d* test are suggested [51]. For the sake of simplicity, the simple t test was employed to formulate the confidence intervals of the response variables as conversion and selectivity but the multiple comparison tests were performed without significant compromise of accuracy in the conclusions.

3.2 Evaluation of sol-gel prepared $VOHPO_4 \bullet 0.5H_2O$ in the partial oxidation of n-butane

The materials prepared on this study are compared with a control synthesized through the traditional methodology [22]. Conversion, selectivity and intrinsic activity were calculated according to Equation 3.1, Equation 3.2 and Equation 3.3, respectively, where *N* represents the molar flow rates (moles per hour) of the species, the subscripts *C_4* and *MA* are indicating butane and maleic anhydride respectively, the superscripts indicate inlet and outlet streams, *w* is the weight of catalyst and *SA* is the surface area of the catalytic material,

$$conversion = \frac{N_{C_4}^{in} - N_{C_4}^{out}}{N_{C_4}^{in}} * 100$$

Equation 3.1

$$selectivity = \frac{N_{MA}^{out}}{N_{C_4}^{in} - N_{C_4}^{out}} * 100$$

Equation 3.2

$$Intrinsic\ \ Activity = \frac{N_{MA}^{out}}{w * SA}$$

Equation 3.3

Even though researchers activated the precursors under an oxidizing atmosphere and our activation (dehydration process) was under anaerobic conditions, traditionally prepared catalysts yielded similar conversion and selectivity as reported [22]. The implication of an anaerobic activation procedure is the formation of non-selective V^{3+} phases during activation under nitrogen since intercalated benzyl alcohol might act as a reducing agent [73]. Despite the possible formation of V^{3+}, we chose this activation procedure to avoid the over-oxidation of the precursors with an aerobic atmosphere as suggested by the same authors [73]. Thus, this catalyst is an appropriate baseline to compare with the sol-gel prepared materials.

3.2.1 Conversion and selectivity

The results of the catalysts evaluation are shown in Table 3.2. The conversion levels of the four catalysts were not significantly different, as seen by the overlapping of the confidence intervals in Table 3.2. Selectivity increases when the amount of solvent used during the precursor's drying decreases. The confidence intervals for selectivity of traditional and low solvent treatment do not overlap, meaning that the low solvent treatment is more selective. The confidence interval for the medium solvent treatment overlaps with the traditionally prepared material, suggesting similar selectivity, while the high solvent treatment has a lower selectivity than the traditional treatment. These results are attributed to the fact that the materials prepared with low amounts of the solvent have higher concentrations of the precursor and, therefore, higher concentration of the active phase after activation.

Table 3.2 Conversion, selectivity and intrinsic activities of traditionally and sol-gel prepared catalysts

Treatment	Butane Conversion	95% Confidence Interval	Maleic Anhydride selectivity	95% Confidence Interval	Intrinsic activity 10^{-5} Mol MA/m^2/h
Traditional	37.42	(29.15,41.7)	28.65	(22.63,34.67)	1.82
Low solvent	31.05	(29.78, 39.73)	41.76	(35.74,47.78)	1.06
Medium Solvent	20.58	(12.31,28.96)	27.99	(21.97,34.01)	1.75
High Solvent	28.36	(20.09,36.64)	12.07	(6.05,18.09)	1.19

3.2.2 Composition and morphology of activated catalysts

The activated catalysts are confirmed to be $(VO)_2P_2O_7$ by the XRD patterns in Figure 3.1[1]. The scanning electron micrographs in Figure 3.2 illustrate the morphology of these materials. Small non-agglomerated crystallites of about 600 nm in length are observed as activated catalysts from LS precursor. A similar shape but larger size, 1000 nm, is observed for active phase from MS and HS precursors. The crystallite thickness was estimated from both the Scherer's equation [69] and the surface area [67] (see section 4.2.2 for better understandig on this statement). The XRD-based calculation yielded 14 nm for those having 600 nm in length and 11 nm for those of 1000 nm; the estimation from the surface area measurements gave values of 4 and 7 nm, respectively. This suggests that it cannot be assumed that the materials have a single morphology, so the surface area-based calculation is likely in error. Selective parts of the activated catalysts are suspected to be the very small particles present in Figure 3.2 b), produced by breaking down the corresponding precursor Figure 2.4 a). The existence of the non-selective low surface area domains is the reason for their low selectivity at the evaluated level of conversion (compared to those reported in the literature for small crystallites of the activated catalyst [54]).

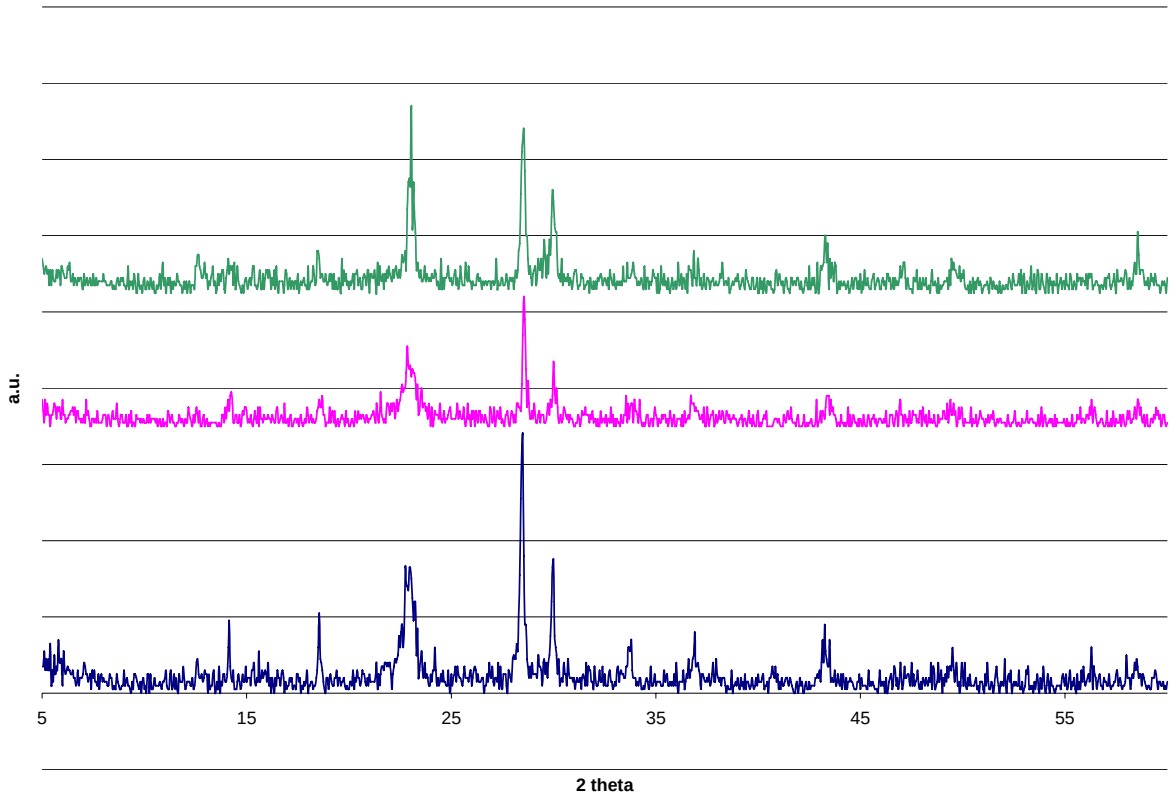

Figure 3.1 XRD patterns of activated catalysts from the precursors prepared with the three levels of extra solvent

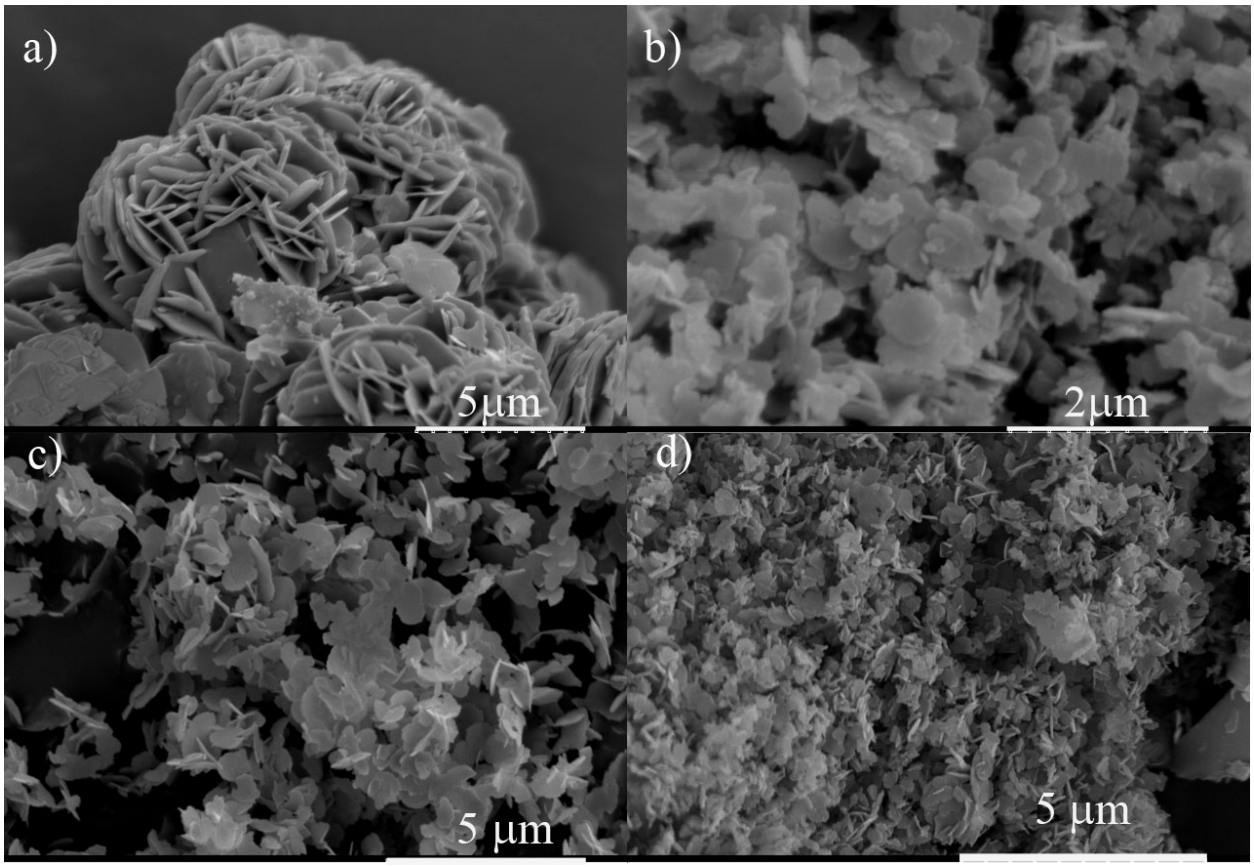

Figure 3.2 SEM of activated catalysts from precursors prepared in a) traditional preparation, atmospheric drying b) alkoxide method, autoclave drying, low solvent c) alkoxide method, autoclave drying, medium solvent and d) alkoxide method, autoclave drying, high solvent.

Chapter 4 Nanostructured $VOHPO_4 \bullet 0.5H_2O$ and $(VO)_2P_2O_7$

As described in previous chapters, autoclave drying provides the required conditions for the reduction of the sol-gel prepared intercalated $VOPO_4$. The 2-propanol produced during the hydrolysis and condensation reactions of the vanadium alkoxide can react with the material producing the reduction. The amount of 2-propanol in the $VOPO_4$ slurry is approximately 0.03 moles and the total volume of the slurry prior to autoclave drying should be 70 mL at least. A concentration of 1.43 M is too low when compared with reduction processes carried out under pure alcohols [63] and the reduction process generates a low concentration of the precursor. One idea is to add extra alcohol together with THF to the slurry prior to the drying process to improve the purity of the precursor.

Early patent literature reported the so-called organic method as a means of involving organic compounds for the reduction steps during the precursor preparation [74]. The preparation includes the reduction of vanadium (V) phosphates, namely $VOPO_4 \bullet 2H_2O$ with alcohols. Benzyl alcohol and iso-butanol are the most widely and consistently used [22, 66]. The nature of the alcohol substantially influences the morphology and then the physical and chemical characteristics of the produced $VOHPO_4 \bullet 0.5H_2O$. Secondary alcohols like 2-propanol reduced $VOPO_4 \bullet 2H_2O$ towards the hemihydrate yielding non-agglomerated crystallites and iso-butanol, a branched primary alcohol, produced rosette-like morphology [22]. Long chain linear alcohols were also used to reduce $VOPO_4 \bullet 2H_2O$ at high pressure and temperature yielding $VOHPO_4 \bullet 0.5H_2O$ [63].

This chapter describes the preparation and the evaluation of a second generation of sol-gel prepared VPO catalysts. Inclusion of 2-propanol during the drying process and toluene during the hydrolysis and condensation reactions are discussed in the following sections. Adding a second component to the slurry inserts complexity to the process. The concentration of that second component can affect the characteristics of the final material since it is very influential in the reduction process inside the autoclave. In addition, the mixing conditions are important since

sufficient time must be allowed to guarantee the complete incorporation of the reducing agent with the gel. Finally, the second compound influences the critical point of the solution and thus the required conditions for the autoclave procedure. For this reasons, this chapter discusses experimental procedures to probe the influence of the 2-propanol concentration and mixing time. Theoretical estimations of the mixture's critical point based on the THF-2-propanol vapor liquid equilibrium and estimation of the concentration of $VOHPO_4 \bullet 0.5H_2O$ in the dried material based on the estimation of the thickness of the crystallites are also discussed in this chapter.

4.1 Experimental

After the gellation process described in previous chapters was finished, the yellow slurry was mixed for 3 hours with 40 mL of 2-propanol and 10 mL of THF prior to the autoclave drying. To study the influence of stirring time, the mixing and stirring between the slurry and the 2-propanol was carried out overnight (15 h) to be compared with the previous preparation. The amount of alcohol was decreased to 20 mL of alcohol and 30 mL of THF to minimize the influence of the polar compound in the gelation process. The autoclave drying was carried out exactly as in the previous chapters and the temperature and pressure were recorded to compare them with equilibrium conditions of the mixture.

For a modification of the gelation process, toluene was mixed with THF in order to decrease the dielectric constant of the solvent and generate smaller crystallites of gel and precursor. A solution of 50 % in volume was used, which kept the orthophosphoric acid completely soluble. The same procedure described in previous sections was followed for the synthesis of this material changing the pure THF for the 50% mixture. The slurry was mixed with the 20 mL of alcohol and 30 mL of THF solution for the drying process.

With the aim of having conditions for the evaluation of the materials closer to those reported in the literature and to avoid the interference of the pretreatment in nitrogen suspected in the evaluations in section 3.2 , the activation and evaluation of the precursors in this chapters were carried out under the reaction mixture. The materials were loaded into a quartz reactor and a mixture of 1.5% (molar) of n-butane in air was flowed through the catalytic bed. The reactor was heated from room temperature to 400°C in 2 hours and kept at this temperature for 72 hours. The products of the reaction were analyzed with the gas chromatograph every 4 hours. The GHSV was between 2100 and 2300 h^{-1} and the values of W/F are from 0.07-0.17 kg of active

phase per mol/h of n-butane. Two independently prepared samples of each material were evaluated in a completely randomized design and a repeated measures analysis (see section 3.2).

Characterization of the catalysts and the products of the reactions were carried out with XRD, SEM, BET and GC as described in section 2.1.3 .

4.2 Theoretical

4.2.1 Prediction of vapor-liquid equilibrium of THF-2-propanol mixtures

In previous chapters, the importance of hypercritical drying to avoid collapse of the gel structure was shown. Determination of the critical point of a pure substance was a very straightforward task; however its prediction for binary mixtures is very difficult due to the system of non-linear algebraic equations that needs to be solved to satisfy the stability conditions [75-78]. Several numerical techniques have been employed to solve the system of equations including global optimization algorithms [79, 80]. Thus, it was concluded that the accurate determination of the critical points for the THF-2-Propanol mixture is out of the scope of this work. Instead, an estimation of the vapor-liquid equilibrium (VLE) will be used to generate an idea of the temperature-pressure region in which they might be located. When the VLE estimation is compared with the data collected from the autoclave drying an analogous graph to Figure 2.3 can be obtained and a similar analysis carried out.

A.VLE model

THF-2-propanol is a mixture of polar non-electrolyte compounds. During the high-pressure drying, pressures higher than 10 bar were measured. Literature suggests that for this type of mixture and under these conditions, the combination of fugacity coefficients based on an equation of state (EOS) and a mixing rule is an appropriate model for the VLE [81]. The EOS and mixing rule combination in the present work aims to follow the original Wong and Sandler approach [82, 83] by using the Peng-Robinson EOS with the Stryjek and Vera improvement (PRSV EOS)[84].

The Wong-Sandler (WS) mixing rule takes advantage of the extensive collection of experimental data available in the literature for binary mixtures at low pressures. The researchers extended the binary interaction parameters obtained from those experimental data to high pressures [82, 83].

Statistical mechanics established that the second virial coefficient (B_{mixt}) of a mixture is a quadratic function of composition according to Equation 4.1 and its general expression from a virial expansion of the PRSV EOS is Equation 4.2 [82, 85]

$$B_{mixt} = \sum_i \sum_j y_i y_j B_{ij}$$

Equation 4.1

$$B_{mixt} = b_m - \frac{a_m}{RT}$$
$$B_{ij} = \left(b - \frac{a}{RT} \right)_{ij}$$

Equation 4.2

Combination of Equation 4.1 and Equation 4.2 yields Equation 4.3, which involves the EOS parameters for the mixture a_m and b_m as function of the parameters of pure substances a_i and b_i (using also Equation 4.4).

$$a_m - \frac{b_m}{RT} = \sum_i \sum_j y_i y_j \left(b - \frac{a}{RT} \right)_{ij}$$

Equation 4.3

Equation 4.3 involves the cross second virial coefficients expressed with an adjustable parameter k_{ij}, Equation 4.4.

$$\left(b - \frac{a}{RT} \right)_{ij} = \frac{\left(b_i - \frac{a_i}{RT} \right) + \left(b_j - \frac{a_j}{RT} \right)}{2} \left(1 - k_{ij} \right)$$

Equation 4.4

Formulating expressions for the a_m and b_m is the aim of the mixing rule, thus an additional expression to combination of Equation 4.3 and Equation 4.4 is required to be able to solve for these values. The expression for the excess Helmholtz free energy from the EOS of the mixture can be evaluated at infinite pressure yielding Equation 4.5 which only depends on molar fractions and parameters of the pure compounds a_i and b_i.

$$a_{\infty}^{E}(\mathbf{y}) = \frac{a_m}{b_m} - \sum_i y_i \frac{a_i}{b_i}$$

Equation 4.5

Solving Equation 4.3 and Equation 4.5 generates the WS mixing rule which satisfies the statistical mechanics condition and the expressions for a_m and b_m. Equation 4.6 depend on the parameters for pure compounds, the excess Helmholtz free energy at infinite pressure, a_{∞}^{E} and the adjustable parameter k_{ij}. Parameter C is a constant dependent on the equation of state, for van der Walls EOS $C=-1$ and for PRSV EOS $C=-0.62322$ [85].

$$b_m = \frac{\sum_i^m \sum_j^m y_i y_j \left(b - \frac{a}{RT}\right)_{ij}}{1 - \sum_i \left(y_i \frac{a_i}{b_i RT}\right) - \left(\frac{a_{\infty}^{E}(\mathbf{y})}{CRT}\right)} \quad and \quad \frac{a_m}{b_m} = \sum_i y_i \frac{a_i}{b_i} + \frac{a_{\infty}^{E}(\mathbf{y})}{C}$$

Equation 4.6

Parameters of pure compounds can be easily determined from critical properties [84]. To determine a_{∞}^{E}, it should be noticed that excess Helmoltz free energy is not a function of pressure ($a_{\infty}^{E}=a^{E}$). Additionally, at low pressure the excess Helmholtz free energy is equal to excess Gibbs free energy thus, $a_{\infty}^{E}=a^{E}=g^{E}$ [82, 83]. Models for g^{E} or the activity coefficient (AC) applied to liquid solutions are widely known (Wilson, NRTL, Van Laar, etc.) and available in the literature [85] and any of these models can be employed to calculate g^{E} (and consequently a_{∞}^{E})[82, 83]. Calculation of g^{E} with an activity coefficient model does not necessarily equate the value from a g^{E} expression derived from EOS and evaluated at low pressures, this condition is forced to be satisfied by adjusting k_{ij} and the activity coefficient model parameters [83]. Thus, the condition of the WS mixing rule can be expressed as $g_{EOS}{}^{E} = g_{AC}{}^{E}$ where the subscripts *EOS* and *AC* are labels for the excess Gibbs free energy calculated from the equation of state and the activity coefficient model, respectively.

For a binary mixture, fitting the binary interaction parameters for both the second virial coefficient used in the mixing rule (k_{12} [83]) and the activity coefficient model Λ_{12} and Λ_{21} for Wilson model (Equation 4.7) or α_{12}, g_{12} and g_{21} for the NRTL model (Equation 4.8 [85]) is the first step in modeling the VLE (where R is the universal gas constant and T the temperature).

$$\frac{g^E}{RT} = -x_1 \ln\left(x_1 + \Lambda_{12} x_2\right) - x_2 \ln\left(x_2 + \Lambda_{21} x_1\right)$$

Equation 4.7

$$\frac{g^E}{RT} = x_1 x_2 \left(\frac{\frac{g_{21}}{RT} \exp\left(-\alpha_{12} \frac{g_{21}}{RT}\right)}{x_1 + x_2 \exp\left(-\alpha_{12} \frac{g_{21}}{RT}\right)} + \frac{\frac{g_{12}}{RT} \exp\left(-\alpha_{12} \frac{g_{12}}{RT}\right)}{x_1 + x_2 \exp\left(-\alpha_{12} \frac{g_{12}}{RT}\right)} \right)$$

Equation 4.8

For the THF (compound 1)-2-propanol (compound 2) mixture, 11 VLE data points at atmospheric pressure are reported and fitted to the Wilson model, Λ_{12}=1.35224 and Λ_{21}=0.45485 [86]. For the whole set of experimental data reported [86], the values of k_{12} for which the condition of WS mixing rule ($g_{EOS}{}^E = g_{AC}{}^E$) is satisfied are dependent on the composition as shown in Figure 4.1. Only one of them will be used to predict the VLE at high pressure, thus a criterion to select the best k_{12} value is needed.

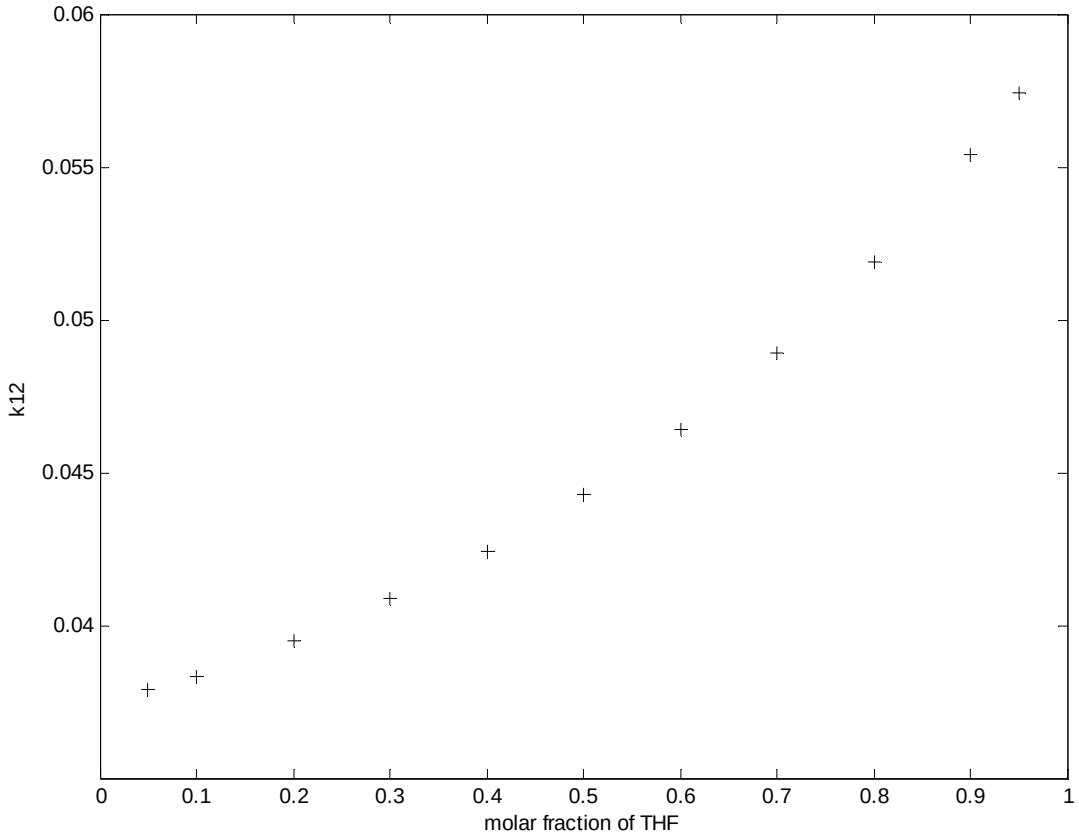

Figure 4.1 Binary interaction parameter for the second virial coefficient of THF (1) and 2-propanol (2) mixtures using the WS mixing rule; the values were determined so that g^E calculated with the mixing model match the g^E from Wilson model, Λ_{12}=1.35224 and Λ_{21}=0.45485 at 1.01325 bar

Literature reported that fixing the value of k_{12} involves the calculation described above and depicted in Figure 4.1 only for $x_1 = x_2 = 0.5$ [85] (page 722). However, Sandler and collaborators suggested that fitting of the available data at low temperature (and consenquently low pressures) making use of binary interaction parameters of g^E for non-ideal solutions (Wilson, NRTL or van Laar) together with the k_{12} is a better approach [78, 87]. The estimative character of the present VLE calculation leads to the formulation of an intermediate approach avoiding the simplification of a single point satisfaction of the mixing rule condition and the complexity of multi parameter fitting.

For each pair in the Λ_{12}-Λ_{21} domain, there is a set of 11 k_{12} values depending on concentration (as shown in Figure 4.1) that satisfy the g^E condition. However, not all of them necessarily satisfy the VLE experimental data at low pressure. Thus, optimizing Λ_{12}, Λ_{21} variables will find the k_{12} values that closely satisfy the two conditions. For the optimization process a function *h* in the form of Equation 4.9 where $1<m<11$ can be written. It generates the values for k_{12} that satisfy the g^E condition. The *h* function is a routine with the numeric solution for k_{12} values by trial and error with a bisection convergence algorithm.

$$k_{12}^{m} = h(\Lambda_{12}, \Lambda_{21})$$

Equation 4.9

Each of the $k_{12}{}^{m}$ values can be used in the mixing rule to determine the temperature and composition of the gas phase of all the experimentally evaluated mole fractions at 1.01325 bar. For this purpose, the fugacity coefficient calculated from the PRSV EOS can be used. Fugacity coefficients φ_i for the component *i* in the phase π (liquid or vapor) depend on temperature, pressure, composition and the set of parameters Λ_{12} , Λ_{21} and k_{12}. The function fugacity coefficients is a very complex equation that has been reported in the literature [82]and won't be presented here.

VLE condition for a binary mixture at low pressure based on the fugacity coefficient approach should satisfy the conditions expressed in Equation 4.10. That can be combined into Equation 4.11 to eliminate y_i.

$$Px_i\varphi_i^L = y_iP$$
$$\sum y_i = 1$$

Equation 4.10

$$\varphi_2^L + x_1(\varphi_1^L - \varphi_2^L) = 1$$

Equation 4.11

Equation 4.11 can be numerically solved for temperature and composition of the gas phase, y_1, for all the 11 x_1 molar fraction values experimentally evaluated [86]. To evaluate the error associated with the set of parameters Λ_{12} , Λ_{21} and $k_{12}{}^{m}$ in reproducing the experimental data, a deviation function was formulated. The expression of the error function is similar to that reported for the simultaneous fitting of the NRTL parameters together with k_{12} for the determination of critical points [78], and they are expressed in Equation 4.12.

$$T_{err} = \frac{\sum |T_c - T_e|}{11}$$
$$y_{err} = \frac{\sum |y_{1c} - y_{1e}|}{11}$$

Equation 4.12

In Equation 4.12 T represents equilibrium temperature and y_1 equilibrium gas phase molar fraction of THF; the subscripts c and e represent the properties calculated and experimental respectively. Thus, 11 values of T_{err}, one for each 11 k_{12}^m, were produced by a single pair Λ_{12}-Λ_{21}. The Λ_{12}-Λ_{21} values that yielded the smallest maximum value of the T_{err} set were considered the ones that best represent the experimental data at low pressure. The pair for the THF-2-propanol system was determined by a simplex algorithm started with the values reported by the fitting of the pure Wilson model Λ_{12}=1.35224 and Λ_{21}=0.45485 [86]. The Wilson parameters that generated the smallest value of the maximum T_{err} are Λ_{12}= 1.3477 Λ_{21}=0.65701 and the 11 k_{12}^m are shown in Figure 4.2 a). Wilson interaction parameters are slightly different from the original ones and the second virial coefficient interaction parameter k_{12} has been reduced in one order of magnitude, when compare with Figure 4.1.

To select one of the values in Figure 4.2 a), the reproduction of the experimental data at low pressure was performed for each k_{12} with Λ_{12}= 1.3477 Λ_{21}=0.65701. The values of the difference in g^E, T_{err} and y_{err} were calculated and are shown in Figure 4.2 b), c) and d) respectively. For simplicity, in these figures the molar fraction of THF in the liquid is used on the abscissa only as label for each of the k_{12} values. Three values of k_{12} were chosen; those that generate minimum values of difference in g^E, T_{err} and y_{err}. Their values were: 0.006607, 0.007467 and 0.00806 which correspond to k_{12} calculated for x_{THF} = 0.5, 0.8 and 0.95 respectively.

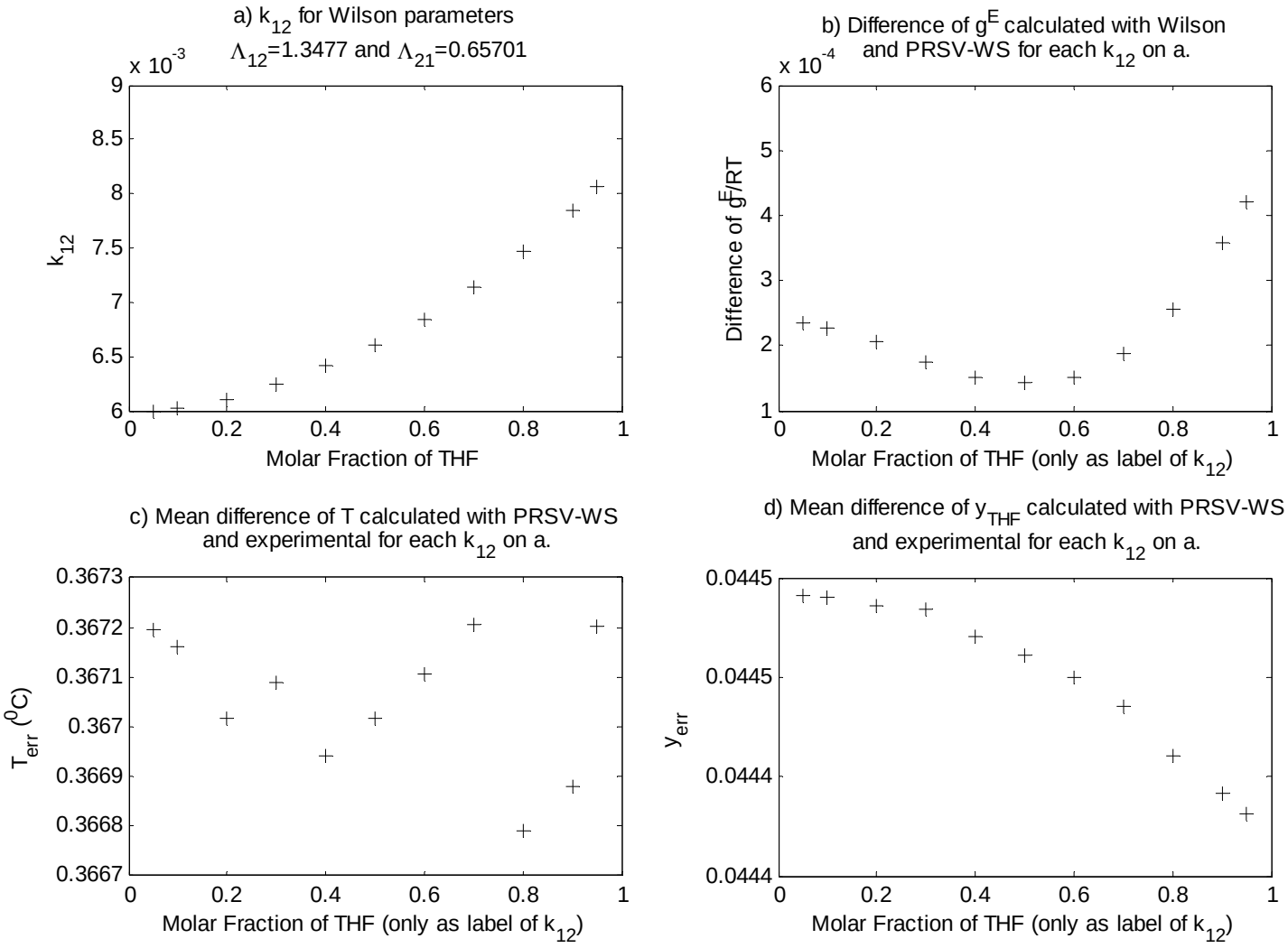

Figure 4.2 Determination of k_{12} that best predicts experimental data at low pressure with PRSV EOS and WS mixing rule

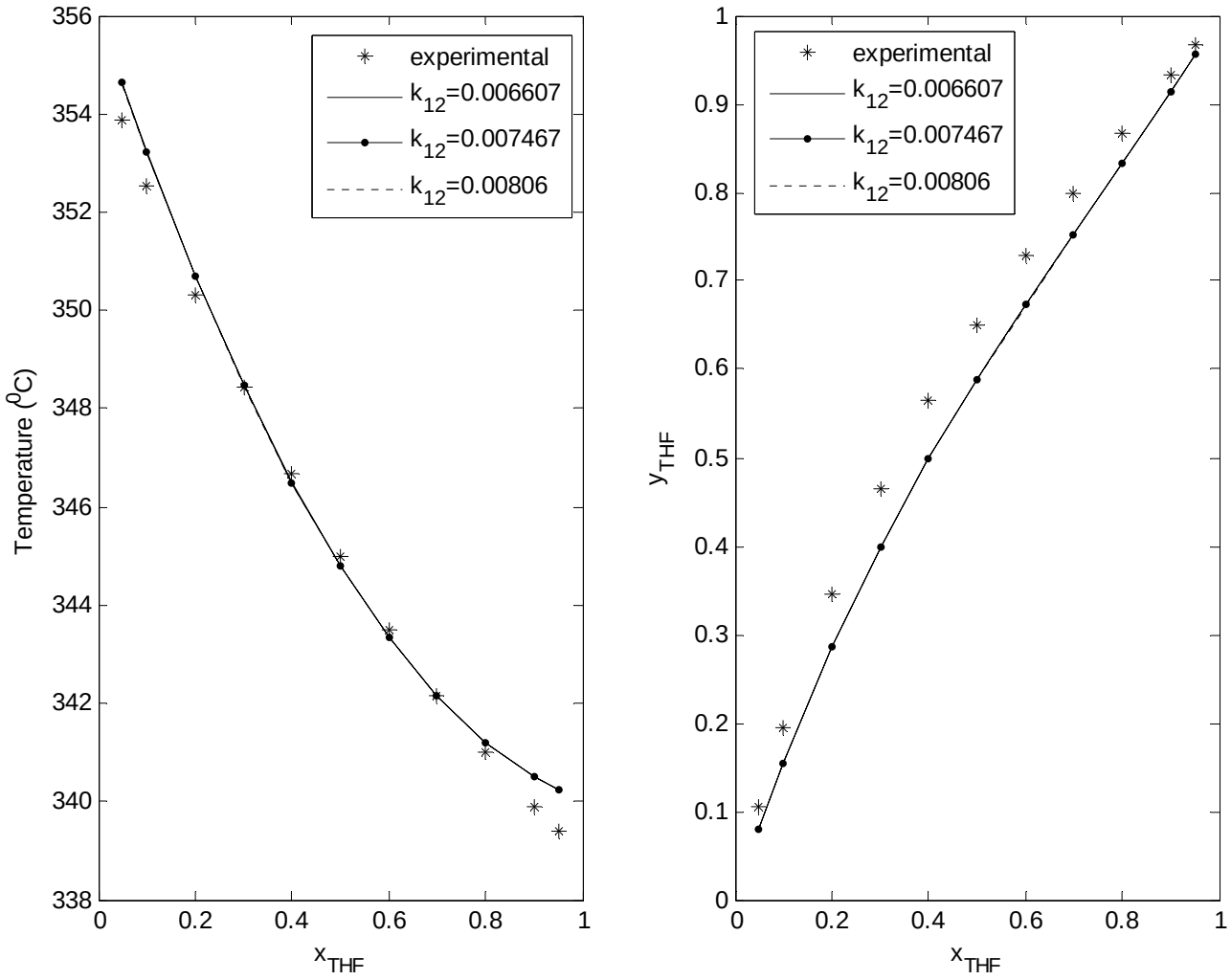

Figure 4.3 Prediction of VLE with PRSV EOS and WS mixing rule with Λ_{12}=1.3477 and Λ_{21}=0.65701 and three values of k_{12}

The comparison of the experimental and predicted VLE data for each of the above mentioned values of k_{12} is presented in Figure 4.3. Evidently, the model based on PRSV EOS with WS mixing rule predicts very well the equilibrium temperature since the fitting parameters were adjusted based on this particular property. The molar fraction of THF in the gas phase, y_{THF} doesn't evidence such a good prediction and the deviation may be attributed to the good conformity of the temperature prediction at the expense of the fulfillment of the g^E condition (which is due to the modification of the Wilson interaction parameters). As there is not considerable difference among the temperature predictions based on the three values of k_{12}, 0.006607 was chosen so the g^E condition can be satisfied in the best possible way.

B. VLE at high pressure

The only way to determine the validity of a model for VLE is with experimental data. However, the lack of such a data at high pressures for the system THF-2-propanol (operating condition inside the autoclave) was the motive to perform this complex calculation. Since the prediction of data near the critical point employing PRSV EOS with WS mixing rule is very sensitive to the binary interaction parameters[78], the approach to calculate them as described in the previous section was tested by predicting VLE for a system whose experimental data at high pressures are available. The results of this test are reported in detail in Appendix B . The example of a binary mixture of methanol-benzene implied that the best k_{12} parameter is the one that minimizes the predictions with an EOS model at low pressures and is also able to represent g^E in agreement with the activity coefficient model. So the properties of the mixtures of THF-2-propanol at high pressures and temperatures can be estimated with a reasonable level of accuracy using the parameters calculated in the previous section.

For this calculation, the fugacity coefficients were determined according to equation reported in the literature [82], selecting the corresponding values of the molar volume for liquid (L) and vapor phase (V). Since at high pressures (>10 bar), the vapor phase no longer behaves as an ideal gas, the equilibrium condition should be expressed as Equation 4.13, which needs to be solved to determine the bubble and dew pressure for different temperatures

$$Px_i\varphi_i^L = Py_i\varphi_i^V$$

Equation 4.13

4.2.2 Crystallite thickness from surface area measurement and XRD analysis

Densities of solid $VOHPO_4 \bullet 0.5H_2O$ and $(VO)_2P_2O_7$ can be determined from their cell parameters and chemical formulas. The values are 2.822 g/cm^3 and 3.342 g/cm^3, respectively[42, 67]. Researchers have used these values, electron microscopy results (knowledge about the crystallite morphology and length) and BET surface area measurements to estimate the crystallite thickness of differently prepared materials [42, 67]. Additionally, XRD microstructure analysis has also been employed to estimate the crystallite dimensions in nanostructured materials [88-90]. Both estimations will agree when the main assumptions in the first approach are valid. These assumptions are: single morphology and a highly pure solid. Therefore, evaluation of the agreement between the two estimations may provide information on the concentration and characteristics of the precursors dried in the presence of extra 2-propanol inside the autoclave.

A.Crystallite thickness from surface area

To estimate the surface area of the material from crystallite dimensions or vice versa, it is necessary to assume a single geometric shape for the crystallites based on electron microscopy. In Figure 2.4 a), b) and c); the morphology of the precursors might be approximated to oblong polyhedron which can be additionally approximated to regular polygon prisms (with any regular polygon as bases). For simplicity, a cylindrical prism will be used to obtain the relationship between crystallite dimensions and surface area, but any regular polygon can be used as the base of the prism to obtain the same expression (with apothem as the analogy to radius).

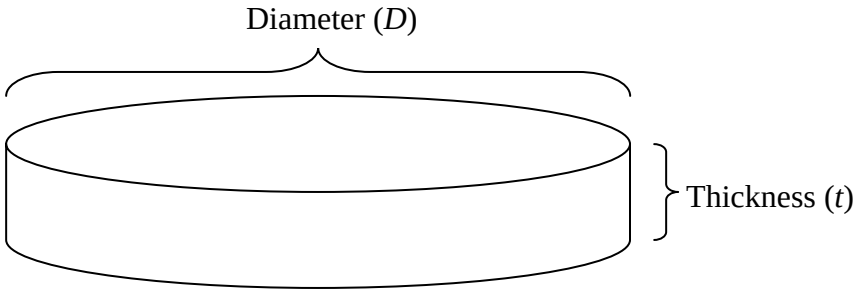

Figure 4.4 Geometric approximation of a crystallite precursor

$$V = \frac{\pi D^2}{4} t$$

$$A = \frac{\pi D^2}{2} + \pi D t$$

Equation 4.14

As seen in Figure 4.4 the volume (V) and external area (A) of this simplification can be easily expressed by Equation 4.14.

As the density (ρ) of the material is known, the mass of the platelet can be determined from volume V. Thus, A should be equal to the surface area (S) multiplied by the mass ρV as shown in Equation 4.15. An expression involving diameter D (which can be also called length), thickness t and the surface area S is obtained in Equation 4.16. D and S can be measured by SEM and BET respectively and t can be determined from Equation 4.16. To keep convenient units in the calculations, Equation 4.17 can be used with t in nm, L (D renamed for generalization) in μm, S in m^2/g and ρ in g/cm^3. This equation has been used in the literature with the same purpose as in this work [42].

$$\frac{\pi D^2}{2} + \pi D t = S\rho \frac{\pi D^2}{4} t$$

Equation 4.15

$$\frac{2}{t} + \frac{4}{D} = S\rho$$

Equation 4.16

$$\frac{2000}{t} + \frac{4}{L} = S\rho$$

Equation 4.17

B.Crystallite thickness from XRD microstructure analysis

Diffraction of incident x-ray or neutron beams on a crystalline material provides information about its structure [90]. Scattered radiation generates diffraction peaks whose position, intensity and shape are directly related with composition and structure of the analyte [91]. In previous sections, the position and intensity of the x-ray diffraction peaks permitted the

identification of the major crystalline component of the precursor and the active phases, $VOHPO_4 \bullet 0.5H_2O$ and $(VO)_2P_2O_7$, respectively. However, provided that the relation between morphology and crystallographic planes of vanadium phosphorous oxide catalysts has been reported [92], information about the crystallite dimensions can be obtained from the broadening (shape) of the diffraction peaks.

Crystallite dimensions are not measured directly from the XRD data. They need to be determined from column heights, which are uninterrupted successions of crystallographic planes within a crystallite. Figure 4.5 represents a square crystallite where column height perpendicular to the (0k0) planes matches the length of edge of the cube. However, in the hexagonal crystallite three different column heights can be observed perpendicular to the (0k0) planes and the corresponding XRD diffraction line will provide a volume-weighted average of three heights instead of the largest one which is the most likely to be meaningful for practical applications [93].

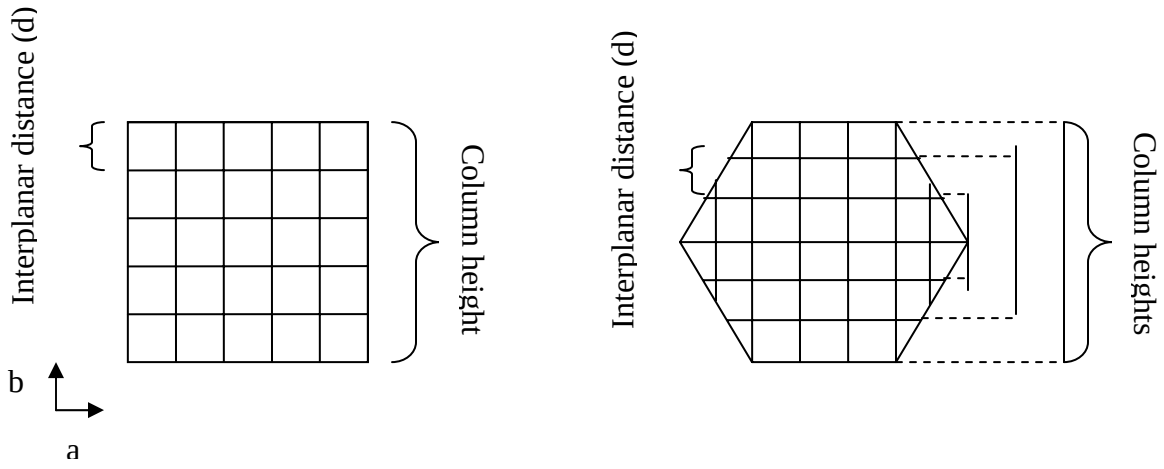

Figure 4.5 Representation of crystallites with square and hexagonal shapes

Thus, knowledge about the orientation of the diffraction planes within the crystallite is necessary to determine which diffraction peaks should be employed to determine each dimension [93].

For the particular case of this study it has been reported that the thickness of the crystallite is a dimension perpendicular to the (001) and (100) diffraction planes for the precursor and the activated catalyst respectively [92]. These diffraction peaks are located at 2θ 15.6° and

23° in the diffraction patters of the precursor and activated catalysts, respectively [1]. These are the diffraction lines that are analyzed in this section.

Crystallite size is one of the sources of peak broadening; nevertheless, crystallography and diffraction techniques define additional sources of peak broadening i.e. instrumental broadening and micro strain broadening [93]. The observed diffraction profile is defined as the convolution of the instrument resolution function and the sample actual profile [90]. To consider all contributions to the peak broadening it is necessary to fit the observed diffraction pattern to a convolution of the instrumental, strain and size contributions; the parameters obtained from the fitting allow the determination of microstructure characteristics of the material. Several techniques have been reported for such a calculation and they have been implemented in crystallography software. Two main approaches for the microstructure analysis are implemented in the available software DIFFRAC^{plus} TOPAS Version 2.1.

The conventional approach makes use of standard samples to determine the instrumental contribution to the broadening. Thus, observed data are fitted to a convolution of instrumental broadening and the sample functions representing crystallite size and strain broadening [93]. Generally, crystallite size broadening can be approximated to a Lorentzian function (Equation 4.18) and strain broadening can be described with a Gaussian function (Equation 4.19) [90]. Other methodologies include the use of Voigt functions (convolution of Lorentzian and Gaussian functions) for both instrumental and microstructure broadening and the observed profile is considered a convolution of two Voigt functions [90] .

$$f(2\theta) = \frac{1}{\pi} \frac{\left(\frac{1}{2} FWHM\right)}{\left(\frac{1}{2} FWHM\right)^2 + (2\theta - 2\theta_0)^2}$$

Equation 4.18

$$f(2\theta) = \exp\left(-4\ln 2\left(\frac{2\theta}{FWHM}\right)^2\right)$$

Equation 4.19

Even though they still use the convolution of instrumental and microstructural broadening, the non-conventional approaches avoid the determination of the instrumental contribution through the standard samples, mostly because they are difficult to obtain

commercially or to prepare. Instead, the methodology determines the instrumental contribution based on the knowledge of the diffractometer emission source and geometry. Both size and strain broadening can be approximated with Voigt functions (Double-Voigt approach) [93].

This standardless approach can be used in materials with anisotropic crystallites where microstructure analysis necessitates identifying the relationship between the shape-characteristic dimensions (diameter, thickness, length, etc.) of the crystallite and the (hkl) diffraction planes. One or several diffraction peaks may contribute to the calculation of the required crystallite dimensions. Fitting the diffraction profiles of several (hkl) planes with only one dimension in common incorporates constraints to the refining algorithm facilitating, the refinement of several parameters. As stated before, the platelet morphology of the materials studied in this work has been widely reported and it is well known that the thickness of such platelets is perpendicular to (00*l*) and (h00) for the precursor and the activated catalyst respectively [92]. However, only (001) and (200) diffraction peaks have been indexed for these materials [1] and no other diffraction peaks can be easily correlated to the thickness of the crystallites.

When no multiple orders in (hkl) diffraction lines are present for a particular dimension, the single-line fitting is the only available method [94], which is a simplification of the Double-Voigt approach. The absence of multiple orders in (hkl) diffraction lines renders impossible the option of constraining several refined parameters in a complete Double-Voigt approach and yields meaningless values for the crystallite size. The simplification uses pure Lorentzian and Gaussian functions to approximate the size and strain contributions respectively [88, 90, 94].

For the precursor and the activated catalysts, the standard samples were not available; consequently, the simplified standardless refinement procedure was carried out with the available software DIFFRAC^{plus} TOPAS Version 2.1. The corresponding elements related with the emission and optics were provided to the software routine and the use of Gaussian functions for the crystallite size contribution and the Lorentzian functions for the strain contribution were disabled.

A report from the software can be observed in Table 4.1 for the precursor prepared with 2-propanol and THF as solvents. R-values are quantitative measurements of the refinement quality and they are reported mainly for the so called Rietveldt analysis to index all the (hkl) diffraction planes to an X-ray diffractogram, which is not the purpose of this study. GOF and DW stand for goodness of fit and Durbin-Watson parameters whose ideal values are one and two

respectively [93]. The background is internally defined by the software and the instrument parameters were defined according to the software instructions, diffractometer configurations and analysis protocol [95]. In the peaks section, “position” and “I” (intensity) correspond to characteristics of each peak after the removal of the instrument contributions, in degrees and counts respectively. “Cry size Lor(nm)” is the thickness (in nm) calculated based on the full width at full maximum (FWHM) of the Lorentzian function describing the size broadening. The value “k: 1, LVol-IB (nm)” is the thickness calculated based in the integral breadth (Area/Intensity) of the same Lorentzian function. The software literature strongly recommends this latter calculation to estimate the desired dimension of the crystallite. The value “k: 0.89, LVol FWHM (nm)” reports the thickness based on the Scherrer’s equation with FWHM of the pure Lorenztian function. The strain parameters are calculated based in the FWHM and the integral breadth of the pure Gaussian function. In Figure 4.6 the fitting of the experimental data taking into account the presence of the (110) diffraction line at 15.17° is presented. Solid lines represent the convolution of instrument, size and strain broadening functions.

Table 4.1 Single-line analysis of sol-gel prepared $VOHPO_4 \bullet 0.5H_2O$ microstructure from XRD data

R-Values

Rexp : 26.34	Rwp : 28.92	Rp : 20.10	GOF : 1.10
Rexp': 33.13	Rwp': 36.38	Rp' : 26.51	DW : 1.94

Background

Chebychev polynomial, Coefficient	0	3.70
	1	-0.58

Instrument

Primary radius (mm)	217.5
Secondary radius (mm)	217.5
Receiving slit width (mm)	0.1
Divergence angle (°)	0.3
Full Axial Convolution	
Filament Length (mm)	12
Sample Length (mm)	15
Receiving Slit Length (mm)	12
Primary Sollers (°)	2
Secondary Sollers (°)	2

Peaks Phase 1

Phase name — Peak Phase:0

Type	Position	I		
FP	15.170	3.4	Cry Size Lor(nm)	58
			k: 1, LVol-IB(nm)	37
			k: 0.89, LVol-FWHM(nm)	52
			Strain G	0.0
			e0	0.0
FP	15.6325	55.4	Cry Size Lor(nm)	19.8
			k: 1, LVol-IB(nm)	12.6
			k: 0.89, LVol-FWHM(nm)	17.6
			Strain G	0.99
			e0	0.25

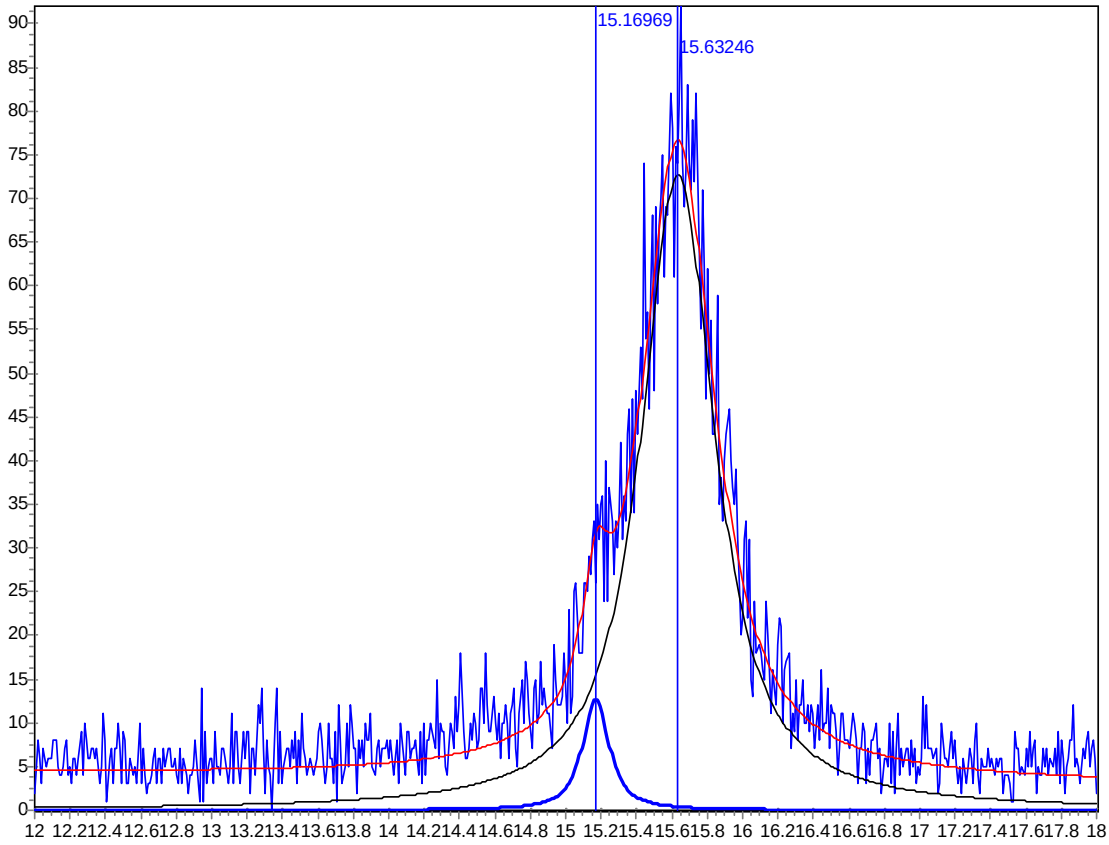

Figure 4.6 Fitting of (110) and (001) diffraction planes of sol-gel prepared $VOHPO_4 \bullet 0.5H_2O$ with lorentzian and gaussian functions for crystallite size and strain broadening

4.3 Time and concentration for mixing the slurry with 2-propanol

4.3.1 Effect of mixing time

When materials are mixed with a solution of 40 mL of 2-propanol and 10 mL of THF, the resultant powder consists of chunks of material with an external layer of a bluish compound and a fluffy brown material in the core. This observation suggests that the material didn't have enough contact time with the 2-propanol and only the external parts of the slurry's chunks were reduced. Thus, when the slurry is stirred with the alcohol solution overnight the resultant material has a surface area of 53 m^2/g and can be identified as a better crystallized precursor by the XRD analysis which is shown in Figure 4.7.

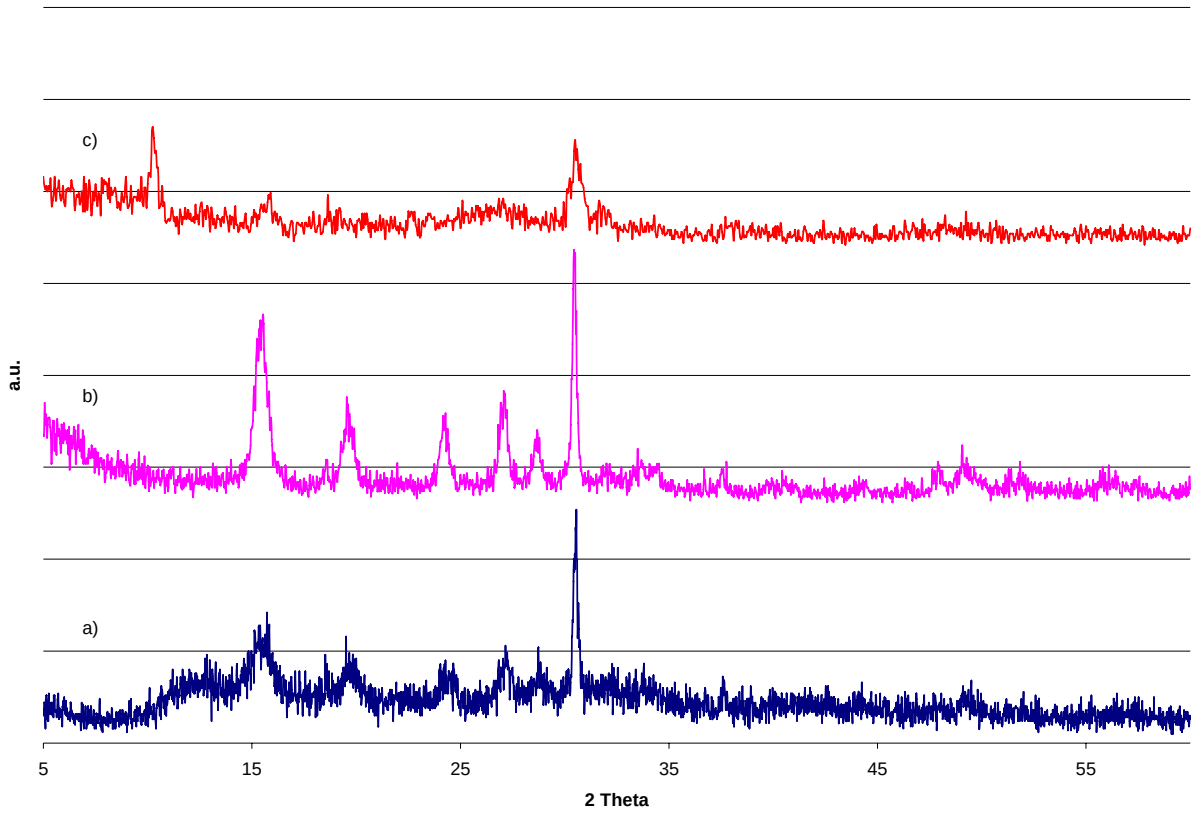

Figure 4.7 XRD analysis of powders after mixing slurry with 40 mL of 2-propanol and 10 mL of THF: a) 3 hours of mixing time, b) 15 hours of mixing time and c) no mixing

A well developed (100) plane can be observed for the precursor that was mixed overnight. The 15.4° diffraction peak in Figure 4.7 b) is sharper and more intense than those for 3 hours of mixing and no mixing process. The macro structure of the gelled intercalated $VOPO_4$ is a solid network with THF within its pores. Appropriate time and speed in the mixing process are necessary for the alcohol to homogenously diffuse into the THF.

4.3.2 Effect of 2-propanol concentration

The crystallinity of the precursor prepared with 40 mL of 2-propanol and mixed overnight is superior compared to non-mixed slurries as the one in Figure 4.7 c). Still, the amount of alcohol added could influence the drying process by modifying the critical point of the binary mixture and then the surface area.

Initially, employment of 2-propanol as the solvent for the sol-gel process could be suggested since both vanadium alkoxide and phosphoric acid are soluble in it. However, a very

significant influence of solvent's polarity on the hydrolysis steps in sol-gel synthesis has been reported in the literature and using a highly polar solvent for this particular case is not recommended [96]. Therefore, reduction of the alcohol amounts may be beneficial.

Again the XRD analysis of the precursors prepared in different concentration of 2-propanol was performed and is shown in Figure 4.8. Both materials have very similar crystallographic characteristics and can be undoubtedly identified as $VOHPO_4 \bullet 0.5H_2O$. The surface area of the material mixed with 20 mL of alcohol was 40 m^2/g.

The surface area of both precursors in Figure 4.8 is lower than the value reported for low and medium solvent without extra alcohol (65 and 102 m^2/g, respectively). Thus, the amount of alcohol included prior to the dying process significantly improves the crystallinity and hemihydrate contents of the sol-gel prepared precursors, but their surface area drastically declined. Two reasons are formulated for the decrease of surface area. First, it might be attributed to a drying process that does not reach the critical point of the THF-2-propanol mixture. Second, the low surface area may be due to the low intrinsic surface area of the hemihydrate. The fundamentals to discern among these possibilities were described in sections 4.2.1 and 4.2.2 , the results of such discriminations are discussed in the following sections.

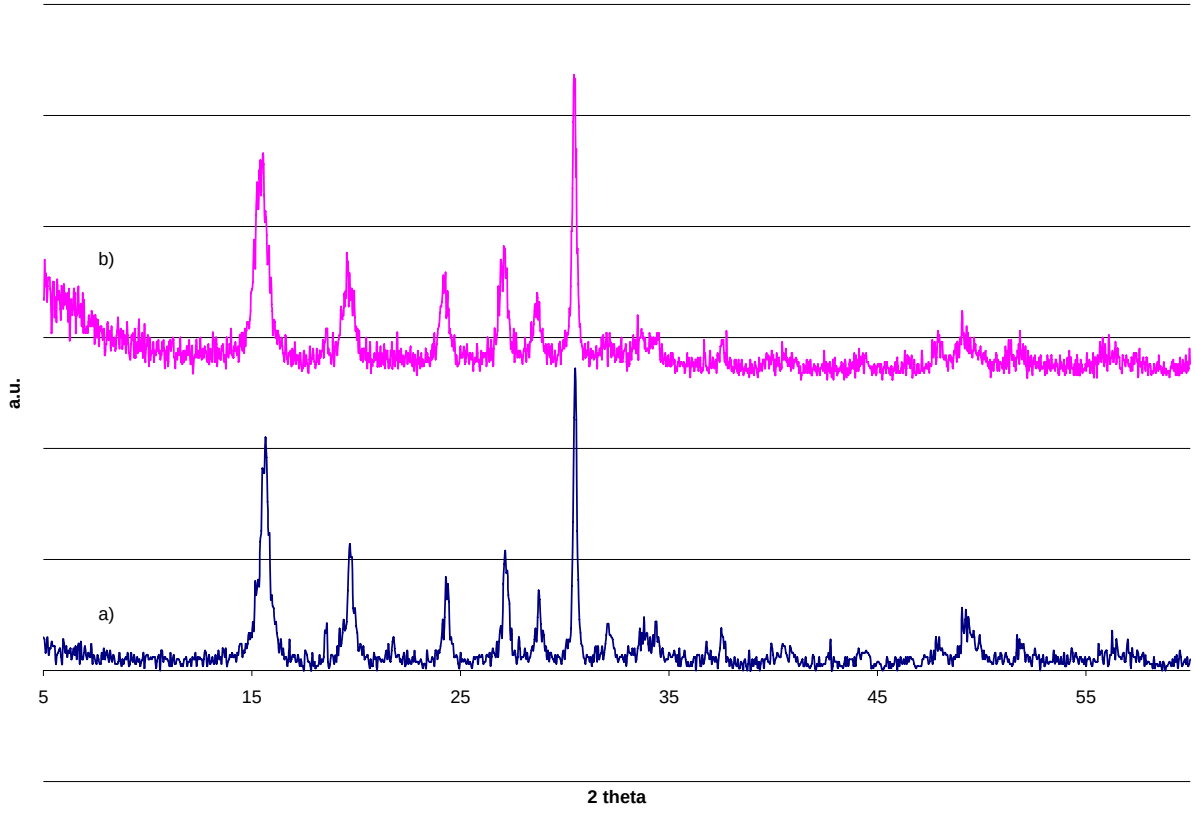

Figure 4.8 XRD analysis of dried powders after mixing 2-propanol for 15 hours: a) 40 mL of alcohol and 10 mL of THF and b) 20 mL of alcohol and 30 mL of THF

4.4 Verification of hypercritical condition and composition

4.4.1 VLE at high pressures for a mixture of THF-2-propanol

Equation 4.13 was used to determine the bubble and dew pressures for different temperatures according to the conventional algorithms for this calculation. Results for temperatures between 90°C and 250°C are presented in Figure 4.9. Two important features can be highlighted from these results. First, for all P-x-y diagrams dew pressure is grater than bubble pressure within certain x-y intervals. And second, the smoothness of the predicted functions is considerably affected at values greater than 210°C. The reasons for the generation of the unrealistic smooth curves can be attributed to the implicit error of the model, polyazeotropy or to the model's inability to predict partial or total immiscibility for the liquid phase at high pressures.

THF and 2-propanol have very similar vapor pressures, as can be seen in Figure 4.10. Values from Antoine's equation are represented with dotted and dashed lines and are labeled as pure THF and pure 2-propanol [86]. The similar vapor pressures will result in a higher chance for the existence of azeotropes and relative volatilities close to one. Relative volatility α_{12} is defined in Equation 4.20. For this reason the deviation observed in Appendix B for the PRSV EOS with WS mixing rules with respect to experimental data can yield unrealistic predictions when bubble pressure and dew pressure lines are so close to each other.

$$\alpha_{12} = \frac{y_1 / x_1}{y_2 / x_2}$$

Equation 4.20

In Figure 4.9 at 110°C and 130°C it can be noted that the dew and bubble point lines cross for intermediate values of x_1-y_1 and a more logical prediction is possible at highly concentrated mixtures. The tangential intercept of the bubble and dew pressure lines is evidence of the presence of azeotropic mixtures, so two intercepts (even though they are not tangential) could suggest the presence of two azeotropes (polyazeotropy). Conditions for polyazeotropy have been established in the literature [97]. Polyazeotropy is likely to occur in mixtures with similar vapor pressures. However, one of the azeotropes must be high temperature (low pressure) and the other low temperature (high pressure) which is not the case of P-x-y representations in Figure 4.9: the two intersections are high pressure. It is interesting to mention that polyazeotropy was reported experimentally for a mixture of THF and 1,1,1,2,3,4,4,5,5,5-declafluoropentane [98], and it was suggested to occur because of the double association of polar compounds, which could be the case of THF of 2-propanol. However, the theoretical conditions are not satisfied. This may suggest the bisectional intercepts are due to some different phenomena other than polyazeotropy.

Van Konynenburg and Scott published in the early literature on the analysis of critical phenomena a very widely known set of phase diagrams for binary mixtures [99]. One of the cases in their work is known as type V-A mixture, which is an azeotropic mixture with a partially miscible liquid phase. The authors predicted the VLE with the van der Waals EOS for idealized compounds. The projection of the equilibrium data on the T-x-y plane displayed two separated bubble-dew temperature loops, one with positive slope and the other with negative slope. The

two loops separate due to the presence of the liquid-liquid equilibrium zone which cannot be accurately represented by the PRSV with WS mixing rules model. It is suspected that this is the cause of the smooth unrealistic predictions in Figure 4.9. Experimental evidence of the presence of the two phases would be necessary to confirm this behavior, which is outside the scope of this work.

As smooth unrealistic predictions are attributed to the partial miscibility of the liquid phase, non-differentiable predictions (sharp changes/crossings in the bubble and dew point curves as those shown in Figure 4.9 for T grater than 210°C) are associated with supercritical regions. In such conditions Equation 4.13 is not satisfied by a combination of a liquid and a vapor phases, and the predicted values no longer satisfy the conditions of differentiability which are necessary for the equality of chemical potential.

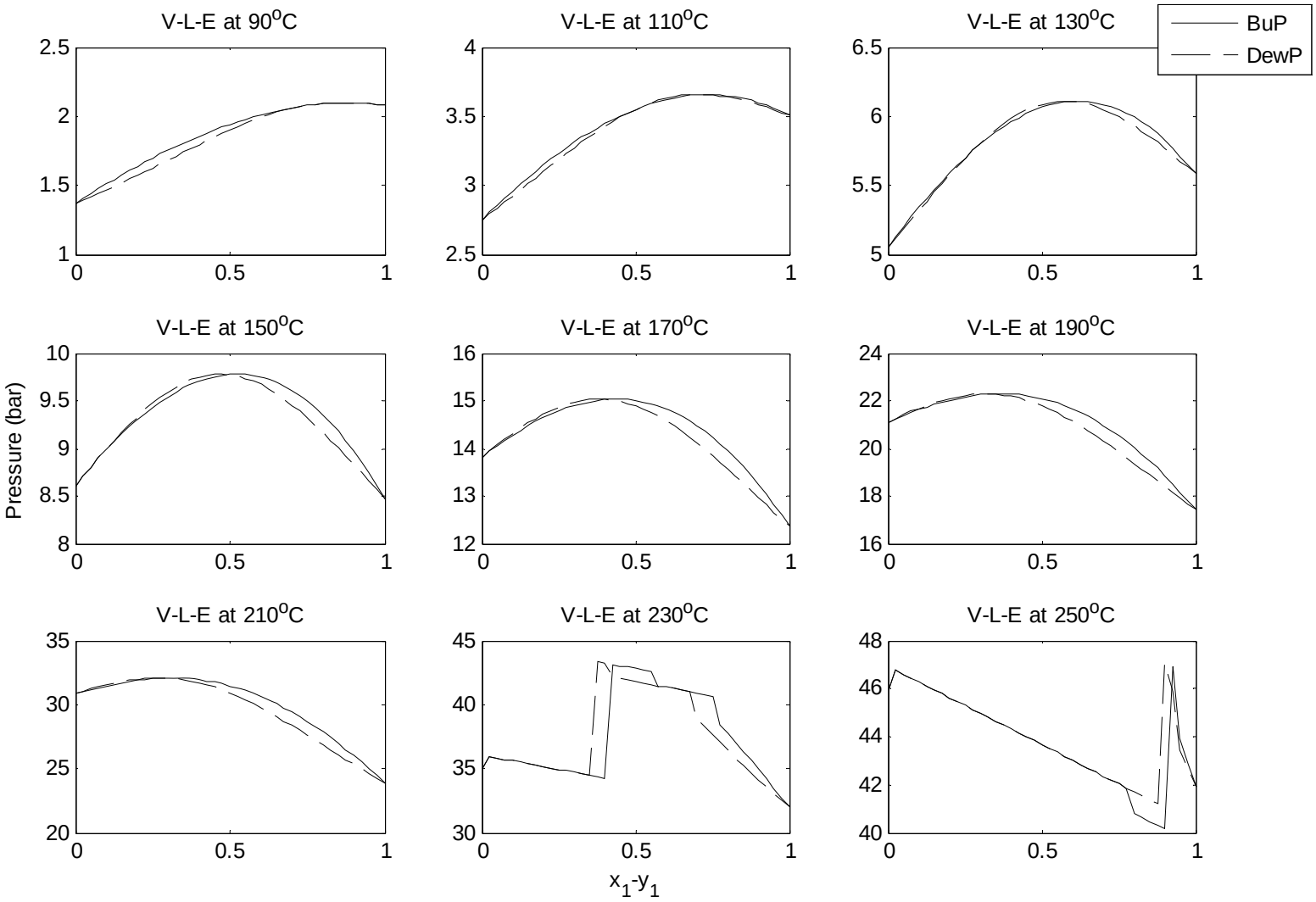

Figure 4.9 P-x-y diagrams for THF-2-Propanol at different temperatures; BuP: Bubble Pressure, DewP: Dew Pressure

4.4.2 Hypercritical condition

Calculations performed in section A and B along with interpretation and understanding of the unrealistic data presented in Figure 4.9 (predictions of VLE at high pressures) allow extrapolation of the bubble and dew point lines to approximately predict the critical points. A simple exercise could be carried out for a set of predicted and experimental data of VLE and critical points reported by Sandler and collaborators [78, 87]. Researchers predicted VLE at high pressures with PRSV EOS with WS mixing rule for mixtures of methane-ethanol and propane-methanol [87]. Predicted values of P-x-y isotherms are not reported in certain domains, but extrapolation of such curves could determine the regions of the critical pressure for each isotherm as shown in Table 4.2. In Table 4.2 the predictions are also compared with the rigorously calculated critical values [78]. The results of the extrapolation agree with the rigorous calculation even though vapor pressures of compounds used as examples in Table 4.2 are very different, which makes the extrapolation even more difficult than when the bubble and dew lines are very close to each other. These examples provided some criteria to roughly estimate a region in the P-T diagram for the loci of the critical points for the two mixtures of THF and 2-propanol as shown in Figure 4.10.

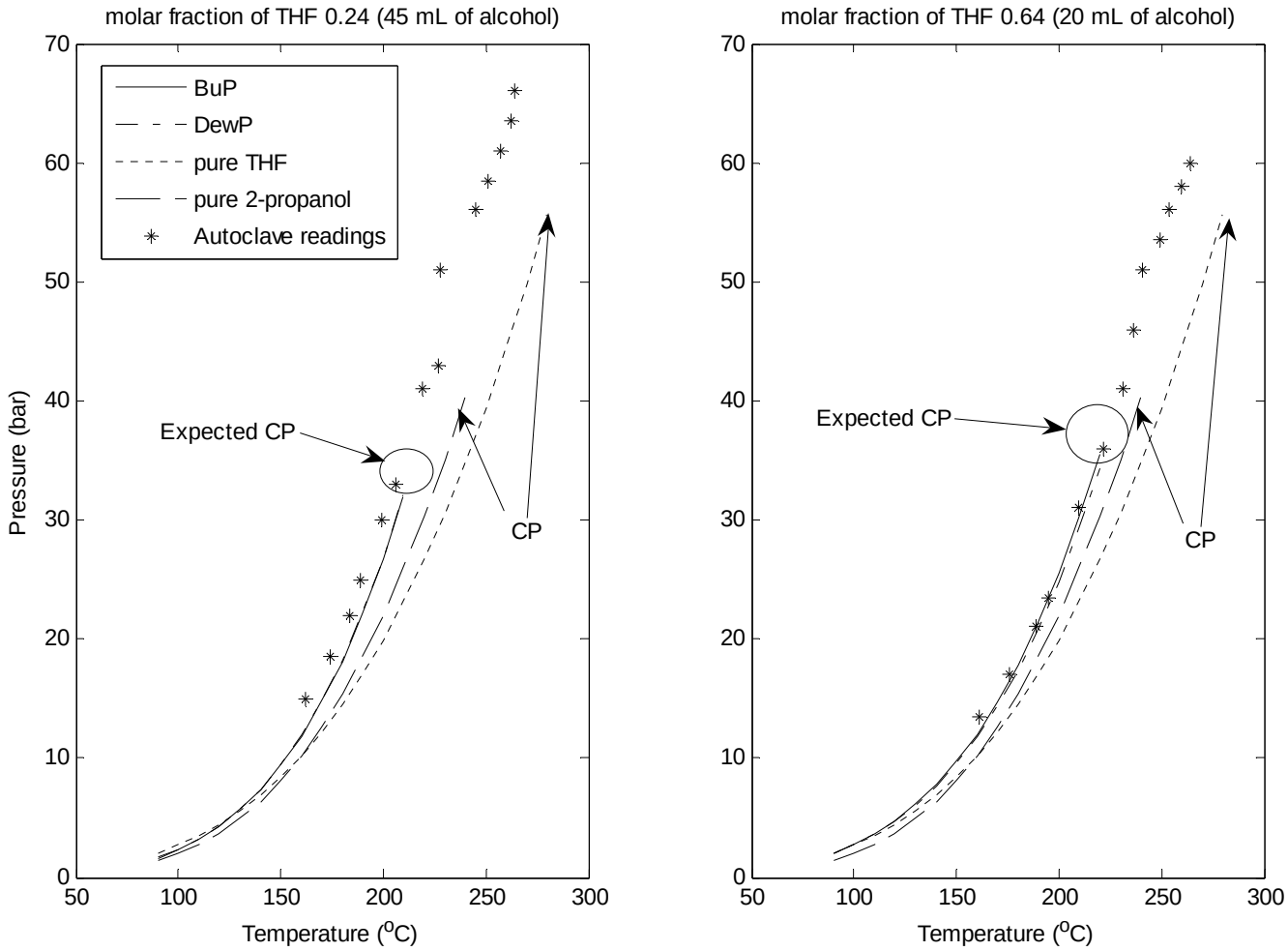

Figure 4.10 P-T diagram for two THF-2-propanol mixtures to identify possible locations of the critical points, BuP= bubble pressure, DewP= Dew pressure, CP=critical point for mixture or pure substances

Table 4.2 Comparison between estimated and calculated ranges for critical point for binary mixtures, N/A: non-available data

System	Isotherm	Pressure range (bar) estimated from predictions	Critical value (bar) reported
Methane-ethanol	298 K	(500,600) [87]	600[78]
	248 K	(480,500) [87]	510[78]
	398 K	(380,440) [87]	300[78]
	448 K	(200,280) [87]	200[78]
Propane-methanol	373 K	(40,46) [87]	42[78]
THF-2-propanol	230°C	(37,42) (Figure 4.9)	N/A
	250°C	(43,45) (Figure 4.9)	N/A

Similar estimations of the critical pressure for the 230°C and 250°C isotherms in Figure 4.9 were carried out in the final part of Table 4.2, but these values would correspond to mixtures with global composition of approximately 0.75 and 0.9 respectively. To be able to estimate the region where the critical point could be located for the composition used during the autoclave drying the smooth trend of the predicted VLE was extrapolated and the region was enclosed in a circle in Figure 4.10. The observed behavior of P-T of the autoclave was plotted together with the VLE data of the mixture and the pure substances and it appears to be very similar to Figure 2.3. The system tends to behave close to the equilibrium and the amount of solvent guarantees surpassing the critical conditions.

From these results it can be concluded that the decrease in surface area of the precursors drying in the presence of 2-propanol is not due to vaporization under the existence of a liquid-vapor interface.

4.4.3 Composition

Measurements of *L* were carried out based on Figure 4.11 and the average values are 1171 nm and 711 nm for the samples treated with 20 mL and 40 mL of 2-propanol, respectively.

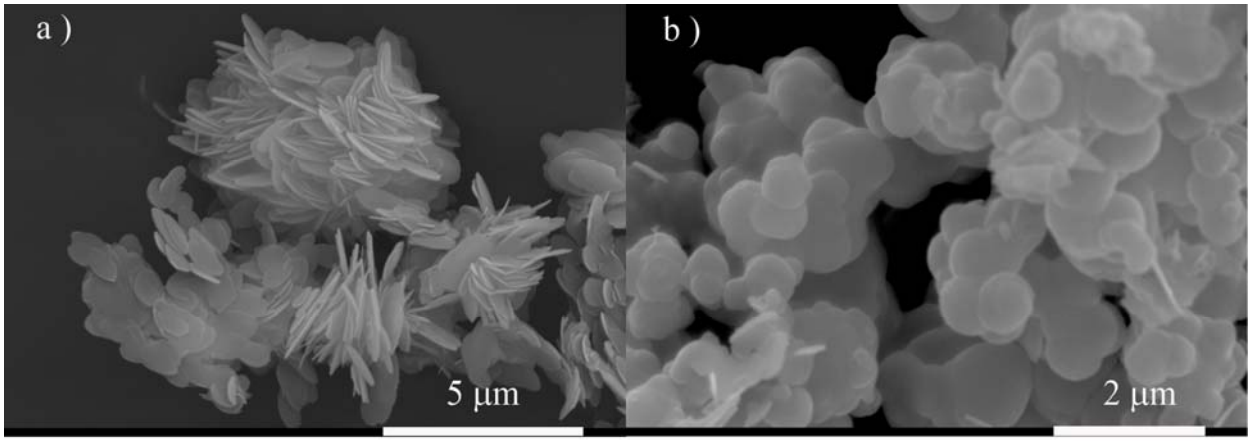

Figure 4.11 SEM of precursors after autoclave drying with combinations of THF and 2-propanol a) 20 mL of 2-propanol and 30 mL of THF, b) 40 mL of 2-propanonl and 10 mL of THF

When catalytic-evaluation results were analyzed in section 3.2 , the low concentration of the precursor and subsequent low concentration of activated catalysts were considered responsible for the low selectivity observed. This argument can be also supported by the comparison of crystallite thickness estimated from surface area measurements and XRD patterns. Table 4.3 shows this comparison for $VOHPO_4 \bullet 0.5H_2O$ prepared using the methods described in sections 2.1 and 4.1 . A reasonable agreement between the two estimations can be observed when the materials were mixed with 2-propanol prior the drying process in contrast with the large difference in the two estimations when the gels were mixed with pure THF. This observation can be interpreted as a validation of the assumptions of homogeneous shape and composition of the precursors made for the BET-SEM estimation.

As discussed in section 4.2.1 the drying process was able to avoid the collapse of the gel which was generated by non-hypercritical condition. Then, the other reason for the low surface area of the materials mixed with 2-propanol is that it is a characteristic inherent to them. The matching of the estimated platelet thickness can actually evidence that a very small crystallite of $VOHPO_4 \bullet 0.5H_2O$ (700 nm in length and 14 nm in thickness) can have a surface area of 53 m^2/g and then be considered good potential precursors for the activated catalysts.

Table 4.3 Crystallite thickness of $VOHPO_4 \bullet 0.5H_2O$ calculated based on BET, SEM and XRD analysis.

Precursor	Thickness from surface area measurement, length estimation from SEM and Equation 4.17 (nm)	Thickness from (001) diffraction line with internal breadth determination of a crystallite size broadening function as Equation 4.18 (nm)
Sol-gel prepared, autoclave drying, pure THF, low amount	6.8	17.4
Sol-gel prepared, autoclave drying, THF-2-propanol, 30mL-20mL	18.3	12.6
Sol-gel prepared, autoclave drying, THF-2-propanol, 10mL-40mL	13.9	14.0

4.5 Modification of gelation step by changing the solvent to reduce the crystallite size

An interesting study on the influence of solvent on the hydrolysis reactions in sol-gel processes and its implications on gelation times and particle sizes has been reported by Ranjit and Klabunde [96]. These researchers concluded that the solvation of the alkoxide may increase the gelation time (delaying the start of the condensation reactions). The solvation is easily produced in polar or protic solvents since they tend to interact with the positive charges on the metal center of the alkoxide, restricting the nucleophilic attack of the hydrolyzing agent and increasing the gelation time. Thus, non-polar or aprotic solvents normally make the gelation process faster to compensate for the insolubility of the hydrolyzing agents [49, 96].

The importance of the effect of the solvent's nature in the hydrolysis reaction depends also on the partial positive charge of the metal center. The higher the positive charge, the lower the effect of the solvent since a highly charged metal center is more prone to nucleophilic attack.

The partial charge on the metal center may be correlated to the electronegativity of the element: the higher the latter, the lower the former. Among the metal centers studied by Ranjit and Klabunde, titanium is the most electronegative one and the effect of the non-polar solvent in the gelation time was certainly the most dramatic as well. Thus, although the partial charge for the vanadium center in the alkoxide used in the present work is not known, a strong effect of the solvent nature can be expected since vanadium is slightly more electronegative than titanium. In fact, the studies on the hydrolysis of vanadium (V) alkoxides perfectly agree with postulates of Ranjit and Klabunde since those studies reported the fast gelation process in aprotic solvents (THF and diethyl ether) when compared with protic solvents (alcohols) [49, 100]. Additionally, Ranjit and Klabunde evidenced the influence of solvent (directly associated with the time required for the hydrolysis reactions) in the particle size and surface area of magnesium oxides from the sol-gel processing of magnesium alkoxides. Non-polar solvents (fast hydrolysis reactions) led to the formation of more seeds for the particle grow during the condensation reactions. Consequently, the non-polar or aprotic solvents inhibited the digestion of the hydroxide particles yielding smaller particles [96].

THF is an aprotic solvent whose dielectric constant is 7.5, so it can be considered a relatively non-polar solvent (toluene, benzene and anisole are less than 5.0 and acetonitrile and N, N-DMF are larger than 35 [96]). As discussed in previous sections, the gelation process of the vanadium (V) isopropoxide oxide with orthosphosphoric acid is really fast and yielded small crystallites after the autoclave drying of the intercalated vanadium (V) phosphates. The resulting precursors were analyzed with XRD to determine the thickness of the crystallite as described in section B and the analysis of the diffraction peak of plane (001) yielded perpendicular column heights of 13.4 nm which is fairly close to those reported for the THF-2-propanol samples in Table 4.3. With a surface area of 50 m^2/g the material is considered very similar to the one gelated in pure THF. This precursor was not observed to be different to the ones gelated in pure THF in terms of the catalytic performance either, however, certain differences in the morphology and surface areas were encountered for the activated phases (as will be discussed later on)

4.6 Evaluation of nanostructured vanadium phosphorous oxides in the partial oxidation of n-butane to maleic anhydride

Two samples of each type of preparation were evaluated as precursors of the partial oxidation of n-butane to maleic anhydride. The evaluated samples were synthesized with the traditional procedure (T), sol-gel prepared and autoclave dried with medium amount of pure THF (M), sol-gel prepared autoclave dried with 20mL of 2-propanol and 30 mL of THF (MiPr 20 mL) and sol gel prepared with a 50% volume mixture of toluene-THF autoclave dried with 20mL of 2-propanol and 30 mL of THF (MT50/iPr20). The results of the evaluation experiment are summarized in Table 4.4. Under the experimental conditions of this study the sol-gel prepared precursors generated more selective catalysts for the partial oxidation of n-butane to maleic anhydride.

Initially, it can be noticed that the addition of 2-propanol to increase the concentration of $VOHPO_4 \bullet 0.5H_2O$ during the autoclave drying did improve the selectivity of maleic anhydride under similar levels of conversion which are evident in the overlapping of the 95% confidence intervals. Again, in this experiment, no significant difference was found in the performance of the traditionally prepared materials (T) and the one dried with medium amount of solvent (M). However, the material dried with pure THF (and consequently the traditionally prepared one) is less selective than the ones dried in the presence of 2-propanol. Toluene as additive to the solvent during the gelation process did not considerably influence the catalytic performance of the materials, but interestingly, the activated materials have very different surface areas and similar intrinsic activities. Low values of surface area were observed in MT50/iPr20 suggesting that these materials might have a slightly different nature on the surface compared to the MiPr 20 mL. It should be noticed that intrinsic activity of nanostructured VPO catalysts have been reported within some range of variability depending on the preparation method (5 to 15 $\times 10^{-5}$ mol of MA/m^2/h) [17, 23, 42]. Thus, even though the experimental conditions were chosen to match those reported by the literature the values for the normalized activity of the materials are difficult to compare.

Table 4.4 Conversion, selectivity and intrinsic activities of traditionally and sol-gel prepared catalysts. T: Traditionally prepared, M: Medium solvent (pure THF), MiPr 20 mL: Medium solvent (20 mL of alcohol), MT50/iPr20: Gelled in 50% toluene-THF and dried with medium solvent (20 mL of alcohol)

Preparation	Butane Conversion	95% confidence interval	Maleic Anhydride Selectivity	95% confidence interval	Intrinsic activity 10^{-5} Mol MA/m^2/h
T	60.9	(45.5,76.2)	27.2	(22.9,32.4)	4.24
M	49.6	(34.3,65)	23.5	(18.2,28.7)	1.41
MiPr 20 mL	52.4	(38,68.7)	44.9	(39.7, 50.1)	3.0
MT50/iPr20	52.3	(37,67.7)	37	(31.8,42.2)	2.91

Even though the concentration of the precursor was increased with the inclusion of 2-propanol, the differences in the intrinsic activity of activated phases imply the presence of impurities or inactive domains that are not contributing to selectivity. Scanning electron microscopy studies may allow the presence of inactive domains to be probed. Micrographs of the activated materials are shown in Figure 4.12. The traditionally synthesized catalyst shows agglomerated platelets (Figure 4.12 a)) which agrees with the literature for traditionally prepared materials refluxed in organic solvents [18]. The morphology of the activated phase dried with pure THF is shown in Figure 4.12 b). The length of the platelets is approximately 0.835 μm and the surface area is 72 m^2/g. The thickness calculated with Equation 4.17 is 8.5 nm and the thickness calculated from XRD analysis 6.9 nm. This implies that the concentration of $(VO)_2P_2O_7$ is relatively high when pure THF was used to dry the precursor. This contradicts the hypothesis that the differences in intrinsic activity are only due to impurities acting as inactive domains. However, the micrographs can provide some ideas related to other differences in the surface characteristics.

The morphology of the activated catalysts dried with THF-2-propanol mixtures can be observed in Figure 4.12 c) and d) for precursors prepared in pure THF and mixtures of THF-toluene respectively. Determining the length of the crystallite is very difficult since for these materials the platelet morphology is not as evident and polymorphism is observed instead. In

Figure 4.12 c) the presence of large platelets (2 μm) and really small particles (100-150 nm) in the center of the picture is evident. In Figure 4.12 d) the polymorphism and the considerable breadth of the particle size distribution are even clearer: large plates are present and small particles with cube shapes can be distinguished in this image as well as in Figure 4.12 e). Since the lengths of the crystallites cannot be measured, estimating the thickness based on the surface area is not feasible. The XRD estimation yield 11 nm and 22 nm for Figure 4.12 c) and d) respectively, but this values can be only considered as the height of crystallite columns perpendicular to (100) plane of $(VO)_2P_2O_7$, since the morphology of these materials is very diffuse. Polymorphism rather than impurity of the activated materials produced from concentrated $VOHPO_4 \bullet 0.5H_2O$ can now be related to the different intrinsic activities in Table 4.4.

The inclusion of alcohol prior the autoclave drying improved the exposure and development of the (100) plane of $(VO)_2P_2O_7$. In Figure 4.13 c) and d) the peaks at $2\theta = 23°$ (100) are the most intense within the difractogram in contrast to Figure 4.13 a) and b) where the intensity of the same reflection is the not the highest. As an additional reference the XRD difractograms can be also compared to the material that yielded the highest selectivity in section 3.2.1 (Figure 4.13 e)) which also has (100) plane with lower relative intensity.

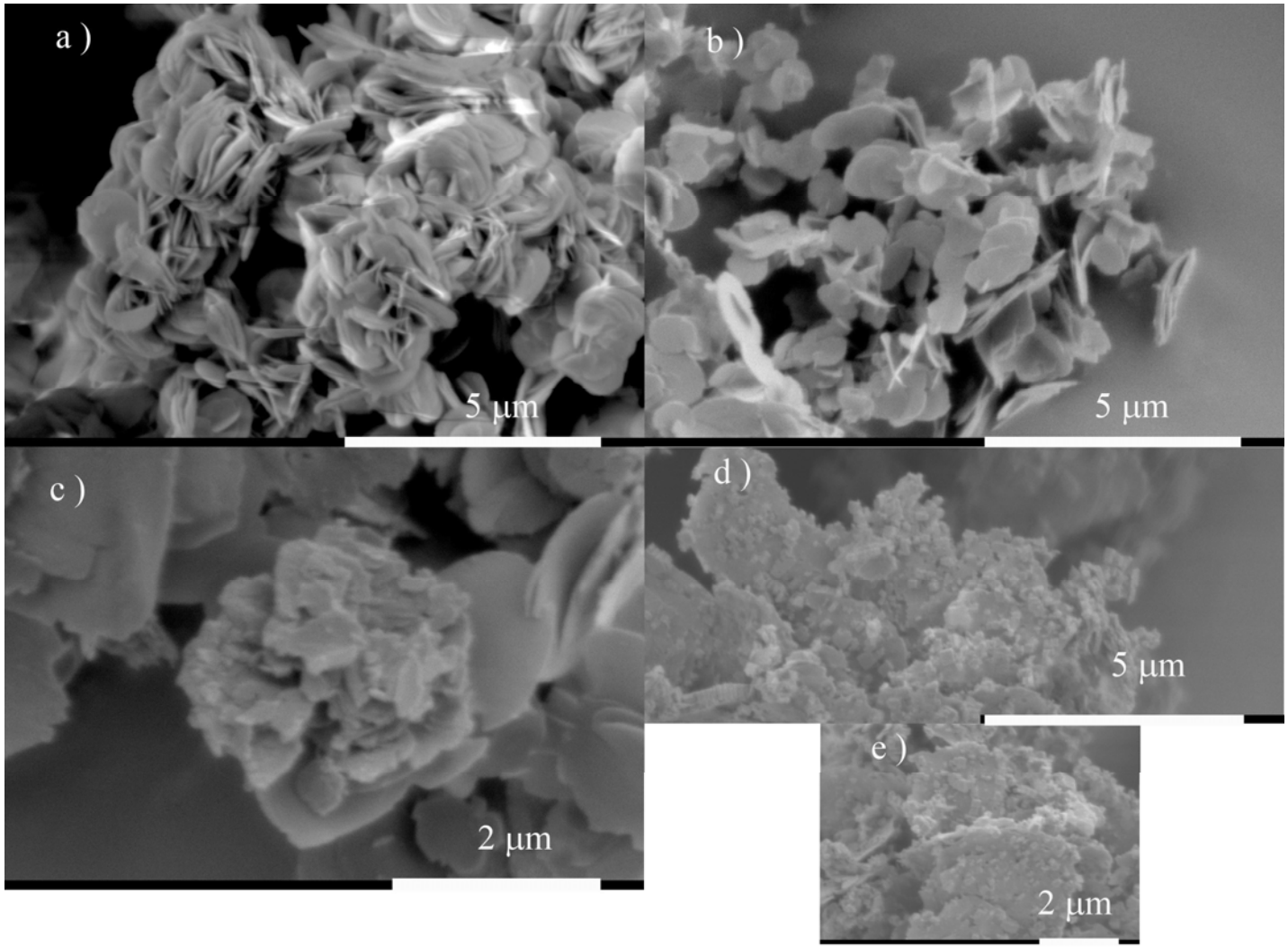

Figure 4.12 SEM of activated VPO catalysts activated and evaluated in 1.5% n-butane in air. a) Traditionally prepared, b) Autoclave dried in THF, c) Autoclave dried in THF-2-propanol, d) and e) Geled in toluene-THF dried as c)

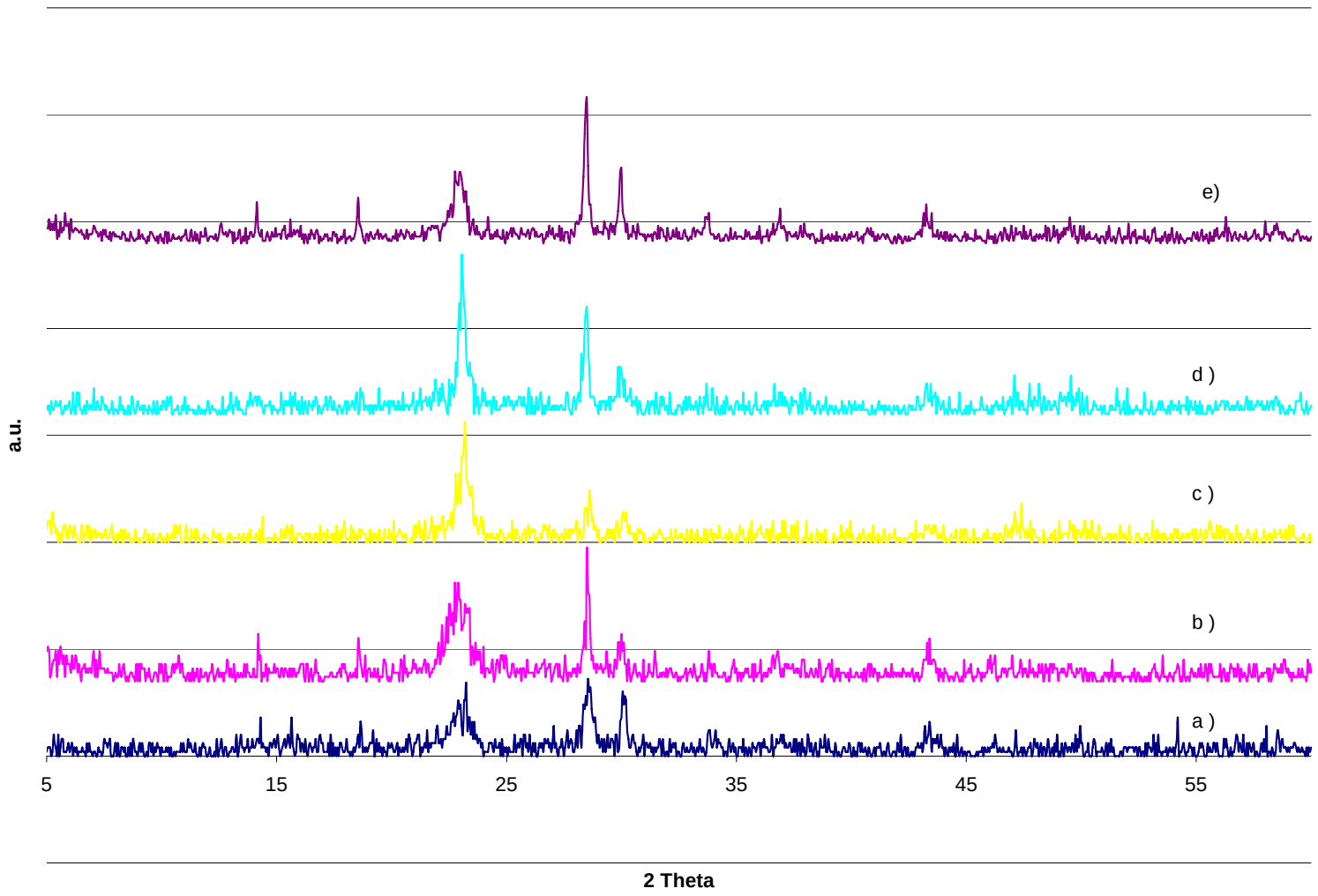

Figure 4.13 XRD patterns of activated catalysts from the sol-gel prepared precursors a) Traditionally prepared, b) Autoclave dried in THF, c) Autoclave dried in THF-2-propanol, d) Geled in toluene-THF dried as c) and e) reference in first experiment

Chapter 5 Aspects on active site and nanostructured $(VO)_2P_2O_7$

Improvement on the catalytic activity of sol-gel prepared VPO catalysts has been discussed in previous chapters. Features associated to the morphology and the particle size are expected to contribute to the identification of species associated with the active and selective surface for the partial oxidation of n-butane. Activation during large periods of time was carried out to enhance the presence of small crystallites. Infrared spectroscopy was undertaken to identify the surface species. In addition, a short description on the most recent literature about active and selective surface precedes the results of the experimental work.

5.1 Experimental

It is speculated that 72 h was not long enough to reach an equilibrated state leading to incomplete formation of small crystallites. Therefore, precursors prepared in pure THF and THF-toluene solutions were treated under reaction conditions for 250 hours (the conditions are and analysis techniques are those in section 4.1). Diffuse reflectance infrared Fourier transform analysis of the activated materials (for 72 h) dispersed in KBr (1:8 weight ratio) was carried out for the identification of the selective surface species (for experimental details see section 2.1).

5.2 Active surface and hydrolysis of $(VO)_2P_2O_7$

The nature and characteristics of the active site of vanadyl pyrophosphate have been a matter of debate since its invention during the 1970's [70]. A model of a "living active surface" is proposed where different active sites, mobility of adsorbed species, multiple reaction pathways, several types of adsorbed oxygen, influence of co-adsorbed species and concerted mechanisms should be considered when formulating mechanisms for the partial oxidation of n-butane [14]. Among those, two main ideas about the active site have been recently formulated. First, the active site is comprised by islands of binary vanadium oxides [101] and second, pure surface of $(VO)_2P_2O_7$ has been considered to be responsible for activity and selectivity [102].

Experimental evidence is more accepted [5, 6, 103] for the idea by Bluhm et al. [101] who claimed that clusters of binary vanadium oxides are the active sites. Xue and Schrader [104] proposed that a reducing atmosphere (n-butane and water) hydrolyzes the $(VO)_2P_2O_7$ surface,

forming V_2O_5. The researchers observed that intensity of the Raman shift band of the V-O-P linkage decreases when $(VO)_2P_2O_7$ is treated with wet n-butane, implying that the linkage is being cleaved. They speculate that n-butane reduction is responsible for the cleavage by removing the oxygen from the linkage, while water reacts with the phosphorous oxides to produce phosphate ion (PO_4^{3-}) whose vibrations were observed with IR spectroscopy. However, other functional groups that must be present in products of this mechanism (P-OH and V-OH) were not observed. Researchers explained this lack of evidence with the low concentrations of this surface species. In the same study, when the materials were treated with oxidizing mixtures, no V-O-P cleavage was observed, implying that linkage oxygen might be replaced by oxygen from the gas phase.

Bluhm et al. [101] suggested that water produced during the oxidation reactions promoted the production of islands of binary vanadium oxides, separated by phosphates. Their in situ XPS studies demonstrate the presence of V=O and V-O-V bonds whose changes in charge density provide a suitable environment for the reaction. They suggest that $(VO)_2P_2O_7$ is converted to H_3PO_4 and vanadium oxides with a general formula V_xO_y where vanadium (IV) are the most likely to be present [105]. These islands are flexible structures that are capable of exchanging electrons easily, undergoing redox processes, and holding non-stoichiometric compositions better than a rigid structure like $(VO)_2P_2O_7$ which might be acting only as a support .

Ballarini et al. [103] suggested that hydrolysis of the surface can take place not only on $(VO)_2P_2O_7$ but also on $VOPO_4$. Hydrolysis of the $(VO)_2P_2O_7$ is favored by a slight excess of phosphorous and the products (vanadium (IV) oxides) are stable towards oxidation. On the other hand, $VOPO_4$ is produced by oxidation of $(VO)_2P_2O_7$ when a slight shortage of phosphorous is present. $VOPO_4$ undergoes hydrolysis only at temperatures higher than 380°C and the product (vanadium (V) oxide) is likely to stay oxidized and is less selective.

Small crystallites of the precursor were transformed into the active phase in the presence of water to study its influence on the activation process [68]. The researchers found that the transformation is accelerated when water is added to the reactant mixture and speculate that water increases the mobility of atoms in the solid phase which favors crystallization and redox processes. However the fast activation process was not observed during a wet treatment under an inert atmosphere.

An active and selective site on the surface of vanadyl pyrophosphate can be reasonably attained by the formation of phosphate species (H_3PO_4) together with vanadium oxides. The high surface area of nanostructured precursors and activated catalysts can provide evidence of the existence of surface phosphate species. In these materials the concentration of surface species is higher compared to low surface area materials (where bulk species predominate) allowing the spectroscopic detection of stretchings associated with surface entities.

5.3 Nanostructured vanadyl pyrophosphate

Small crystallites of $(VO)_2P_2O_7$ have a mosaic-like structure that eventually break down and become very selective towards maleic anhydride [17, 54]. The mosaic-like structure was also observed by Duvauchelle and Bordes [106] when $(VO)_2P_2O_7$ was calcined at 420°C during 48 h. The resulting materials were comprised of several layers of nanostructured crystallites.

As observed in Figure 4.12 d)-e), large platelets of $(VO)_2P_2O_7$ seem to predominate. Small particles with cubic shape are observed when the gelation of the vanadium alkoxide was performed in toluene-THF solutions.. The conversion-selectivity results of the tests are 33-60 for MiPr20mL and 57-27 for MT50/iPr20, which are out of the confidence intervals in Table 4.4 showing a performance that is different and slightly poorer compared to the behavior of the materials reacted for 72 hours.

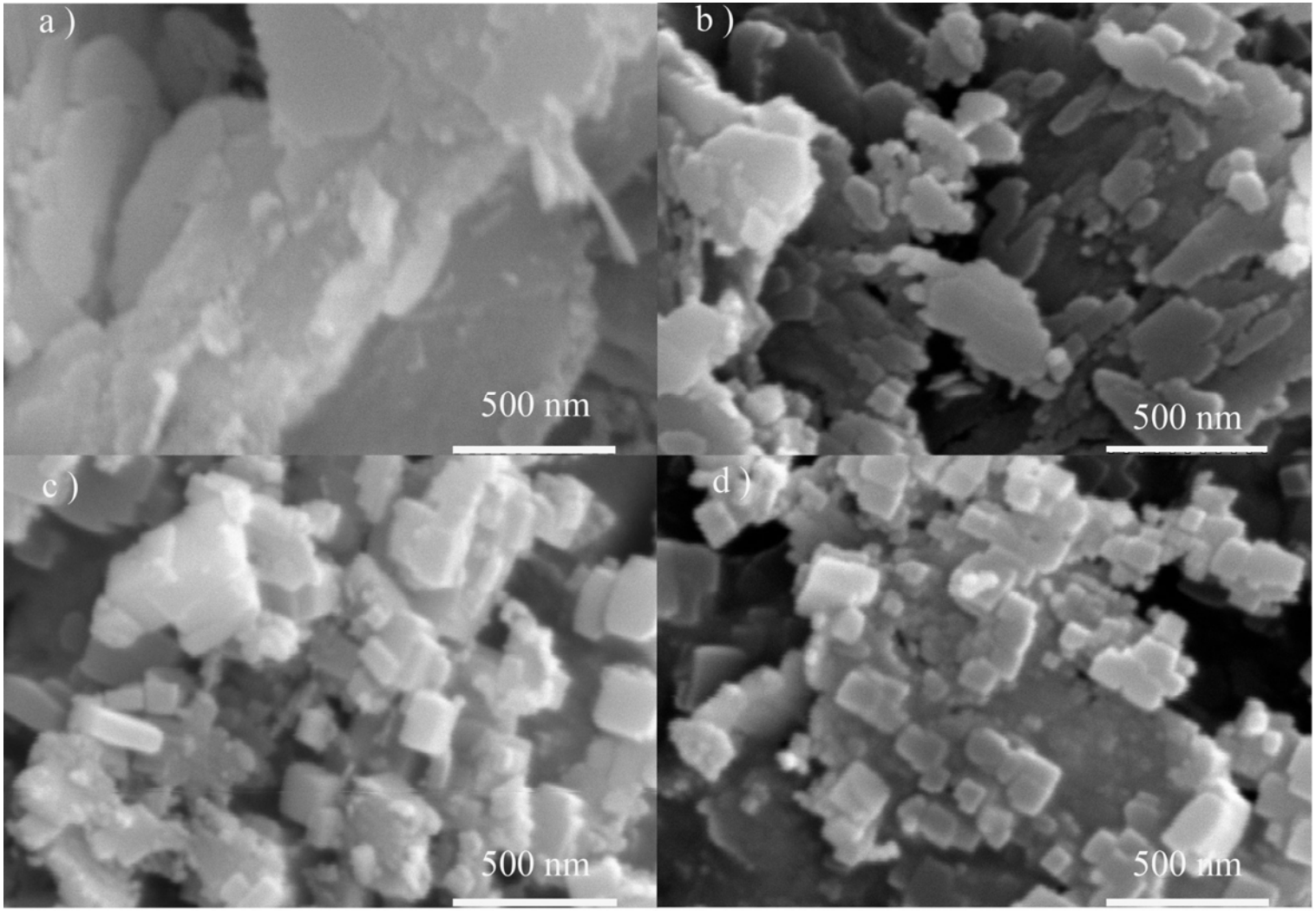

Figure 5.1 SEM of sol-gel prepared $(VO)_2P_2O_7$ gelled in pure THF equilibrated for a) 72h, b) 250 h and gelled in toluene-THF equilibrated for c) 72h and d) 250 h

The analysis of the equilibration process would require a complete experimental design as in section 3.2 . Thus, the only observation that can be made is the presence of small crystallites having dimensions closer to those reported for nanostructured $(VO)_2P_2O_7$ [54] in Figure 5.1 b) and d).

The activated catalyst that were prepared in pure THF (Figure 5.1 a) and b)) shows apparent reduction in the crystallite size when the material was treated for long periods of time (250 h). In contrast, the catalysts in Figure 5.1 c) and d) show nearly the same morphology and abundance of small particles, suggesting that the surface nature of this material doesn't change with longer periods of treatment. This observation is an additional and clearer suggestion of the differences in surface nature between activated materials from precursors gelled in THF and THF-toluene mixtures.

5.4 Identification of phosphate species produced by hydrolysis

Phosphate species play a very important role on the nature of the active site since they may act as inhibitors for crystal grow of vanadium oxides [101]. Gai et al. [107, 108] reported the formation of anion vacancies in the surface of $(VO)_2P_2O_7$ that become extended crystalline defects when the crystal glides along the (201) direction. Employing high resolution electron microscopy, they measured the concentration of defects when the surfaces are treated with reducing atmospheres. The researchers observed that when the surface was treated with steam/N_2 for long periods of time, the n-butane conversion to maleic anhydride, in the absence of oxygen in the gas stream, was low [107]. Researchers tentatively attributed this phenomenon to the formation of a new crystalline phase (irreversibly reduced) when glide shear defects extended throughout the material due to long-time exposures to steam. This concept leads to a possible and interesting explanation for the difficult crystallization and diffusion processes observed by Ryumon [68] when they treated the nanostructured precursors with water in an inert atmosphere. If water is the agent generating the anionic vacancies and cleaving the V-O-P linkage, subsequent formation of high order defects will make crystallization slow. However, the role of n-butane has not been completely evidenced; it could easily remove the V-O-P oxygen from the $(VO)_2P_2O_7$ lattice via redox process[104], allowing water to react with phosphorous oxides, but the products of such a hydrolysis reaction have not been completely detected.

The general idea of this section is taking advantage of the high surface area of sol-gel prepared activated compounds to elucidate the presence of phosphates through their IR spectra and the results are shown in Figure 5.2.

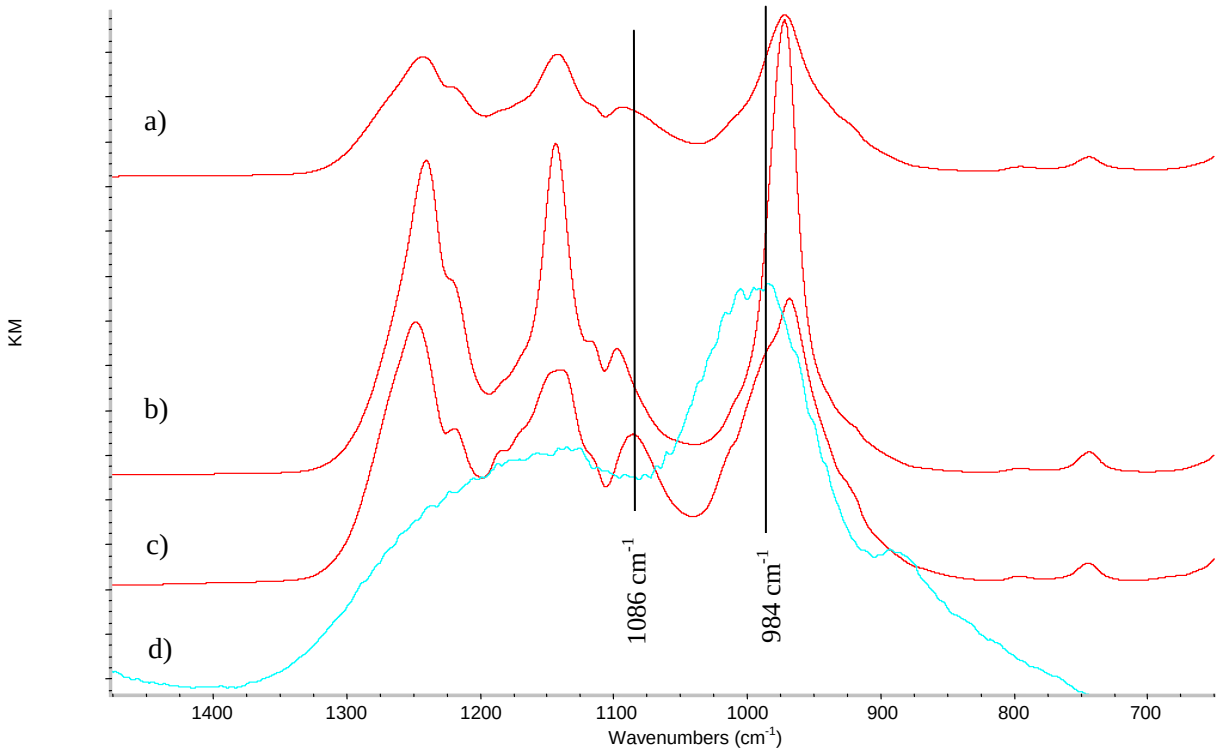

Figure 5.2 DRIFTS of sol gel prepared $(VO)_2P_2O_7$ gelated in b) THF and c) THF and toluene compared with a) traditionally prepared and d) H_3PO_4

The spectra in Figure 5.2 b) and c) are sol-gel prepared $(VO)_2P_2O_7$ whose selectivity was larger than traditionally prepared VPO in section 4.3 . For comparison purposes, spectra a) and d) are those of the traditionally obtained catalysts and phosphoric acid, respectively. The spectrum of phosphoric acid was taken by diluting anhydrous H_3PO_4 in KBr at room temperature.

The oxygen atoms involved in the hydrolysis reactions are those in the base that is perpendicular to P=O bond of the phosphate tetrahedron. Thus, two vibrations may be important in the analysis of these oxygen atoms, $\nu_s(PO_3)$ and $\nu_{as}(PO_3)$, which are reported for compounds like vanadium and potassium phosphates [66, 109]. The band at 970 cm^{-1} has been assigned to ν(V=O) for $(VO)_2P_2O_7$ [66] and is present in Figure 5.2 a), b) and c); however in Figure 5.2 c) a shoulder at 984 cm^{-1} can be observed. This band could be associated with the $\nu_s(PO_3)$ vibration

frequency reported for potassium phosphates (989 cm^{-1}, reported at page 225 of the reference)[109] and observed in the spectrum of anhydrous phosphoric acid in Figure 5.2 d). The $\nu_s(PO_3)$ band for $(VO)_2P_2O_7$ has been assigned at 1095 cm^{-1} which was also observed in Figure 5.2 a) and b), suggesting that in compounds with a less complex solid structure like the potassium phosphates or the H_3PO_4 itself this vibration shifts to lower wavenumbers. As previously discussed, a less rigid structure with free phosphate ions separating vanadyl groups is expected in the surface of activated VPO catalysts. Interestingly, in Figure 5.2 c) a slight shifting of the $\nu_s(PO_3)$ vibration frequency for $(VO)_2P_2O_7$ from 1095 cm^{-1} [66] to 1086 cm^{-1} was observed. This shifted band was assigned to this vibration in $(VO)_2P_2O_7$ treated in wet feed as a consequence of the hydrolysis of V-O-P bonds [104]. Additional broadening of the band at 1140 cm^{-1} assigned to $\nu_{as}(PO_3)$ [66] and clearly present in the spectrum of anhydrous phosphoric acid suggests the presence of some flexibility in phosphate ions present in the VPO catalysts.

The presence of the shoulder at 984 cm^{-1} and the shifting of the $\nu_{as}(PO_3)$ frequency to 1086 cm^{-1} is observed only in the materials that were prepared in a mixture of THF and Toluene. This is an additional difference from those observed between Figure 4.12 c) Figure 4.12 d)-e) and could be a reason for similar intrinsic activities despite different surface areas: the materials have different superficial characteristics.

It is suspected that the relative amounts of small cubic crystallites are lower in Figure 4.12 c) than in d)-e), consequently it is speculated that Figure 4.12 d)-e) crystallites are the ones rich in hydrolyzed V-O-P bonds. However, the expected direct correlation between the apparent amounts of nanostructured crystallites and the surface areas was not observed, suggesting that the relative difference in the amount of small crystallites is only apparent.

Chapter 6 Summary, conclusions and future work

6.1 Summary

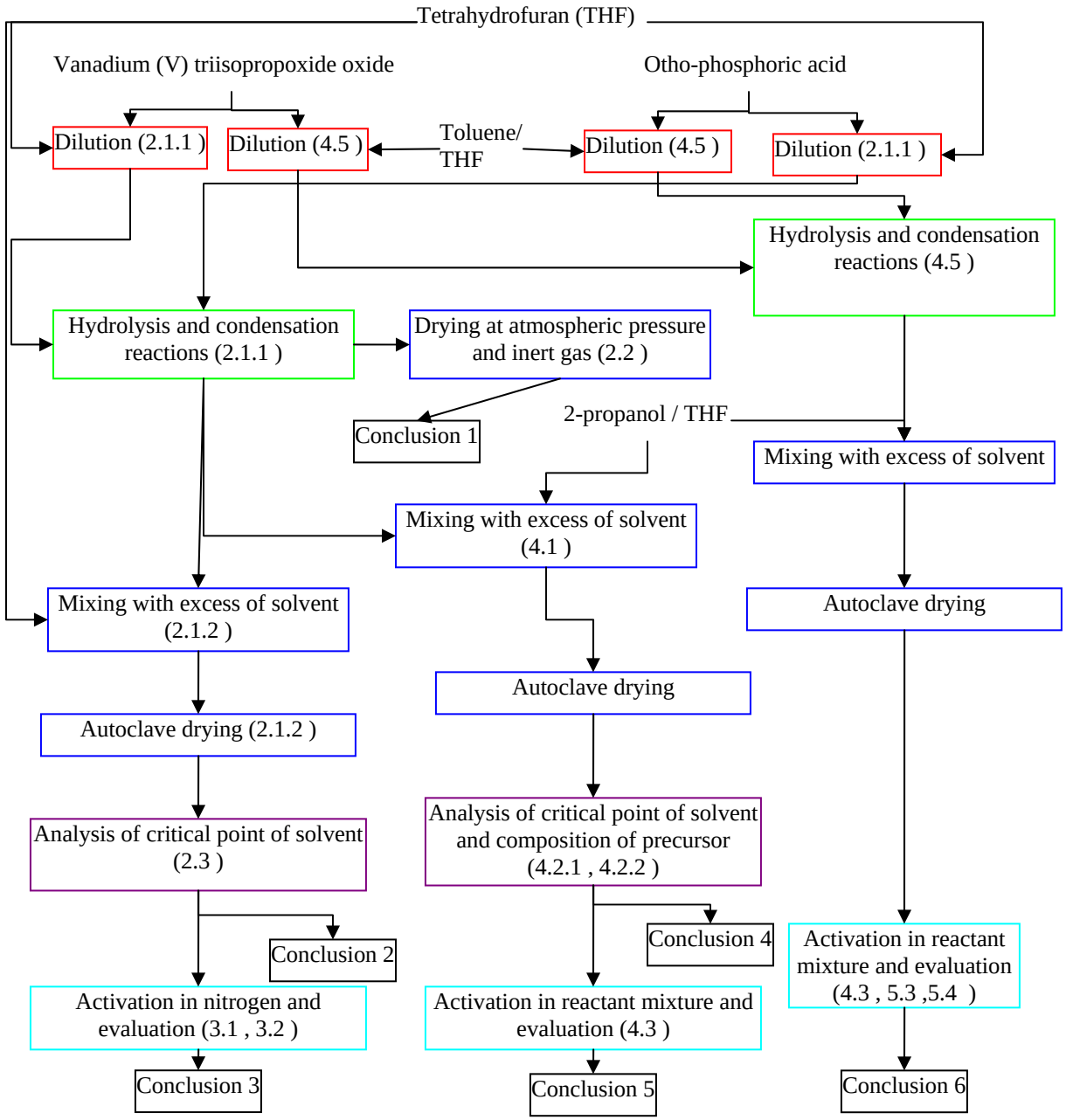

Figure 6.1 Summary of the steps and modifications of the sol-gel synthesis of VPO, numbers in parenthesis are the sections in which the experimental conditions are described and the results are analyzed

The flow chart shown in Figure 6.1 describes the sol-gel process to prepare vanadium phosphorous oxides. The number in parenthesis corresponds to the sections within the body of this dissertation where the step was described or where the results from this modifications were analyzed. The boxes in red describe the dissolution of the chemical compounds that served as sources of vanadium and phosphorous for the hydrolysis and condensation reactions that are described in green boxes. The drying processes, hypercritical and atmospheric, are noted in blue boxes. Study and analysis of vapor-liquid equilibrium to ensure hypercritical conditions are represented in purple boxes. The activation of the precursors towards the active phase is enclosed into the bright blue boxes. Finally, the black boxes show where the main conclusions of the study were drawn.

To understand the synthesis procedure of one of the sol-gel prepared materials, Figure 6.1 can be followed starting from the dilution of vanadium alkoxide and phosphoric acid which were reacted according to section 2.1.1 . The products of the hydrolysis and condensation reactions are mixed with a solution of 2-propanol and THF as described in section 4.1 . The autoclave drying of the slurry is carried out according to the procedures of section 2.1.2 . The conditions of hypercritical drying were studied and analyzed in section 4.2.1 and the analysis of the concentration of the precursor in the dried solid in section 4.2.2 . The analysis of the results allowed the statement of the conclusion 4 on section 6.2 . When the precursor were activated for the partial oxidation of n-butane as described in section 4.3 , conclusion 5 in section 6.2 was drawn.

6.2 Conclusions

1. Sol-gel synthesis in pure tetrahydrofuran resulted in lamellar crystalline $VOPO_4$ whose layers are intercalated with interdigitated molecules of organic compounds like 2-propanol or the solvent itself. The intimate relation between the intercalated molecules and the solid was evidenced with infrared bands typical of carbon bonds and with crystallographic information that can not be associated to any other vanadium phosphorous oxide.

2. The amount of extra solvent prior the hypercritical (autoclave drying) affected the physical and chemical characteristics of the dried aerogels. The more solvent was added the more surface area was obtained due to the absence of a vapor-liquid interface that collapses the aerogel structure and yields non-porous agglomerated solids. Low amounts of extra solvent

allowed high concentration of 2-propanol (byproduct of the acid hydrolysis of the vanadium alkoxide), which effectively reduced the V^{5+} phase towards small particles of $VOHPO_4 \bullet 0.5H_2O$ (the precursor). Autoclave drying yielded high surface area precursors (60-120 m^2/g) from a V^{5+} gel.

3. Activation of the sol-gel prepared and autoclave-dried precursors under an inert atmosphere resulted in $(VO)_2P_2O_7$ (the active phase), which was selective in the partial oxidation of n-butane to maleic anhydride. The active materials are more selective at similar levels of conversion than the catalysts prepared according to the traditional organic method. The obtained catalysts contain nanostructured crystallites that have been reported to be very selective by the literature. However, the distribution of such small particles is not homogeneous, which is also proved by the variation of the intrinsic activity among the preparations. The heterogeneous surface was attributed to the incomplete reduction of the gel inside the autoclave that generated precursors with different contents of small crystallites of $VOHPO_4 \bullet 0.5H_2O$ and consequently small contents of nanostructured $(VO)_2P_2O_7$.

4. Incorporation of 2-propanol along with tetrahydrofuran as the solvent prior to autoclave drying was effective in increasing the contents of the precursor as evidenced in the XRD analysis. However, a relative reduction of surface area was observed (50 m^2/g compared to the previous 100 m^2/g). The reason for such a reduction was clarified by estimation of the critical condition of the mixture to guarantee the condition of hypercritical drying and by estimation of the thickness of the crystallites with techniques that involve different and independent assumptions. The condition of hypercritical drying is satisfied and the estimations of the crystallite thickness agree to each other. The values surface area 50 m^2/g are not low, but are characteristic of materials with crystallite size of 1 μm in length and 15 nm in thickness. Sol-gel synthesis allowed the preparation of high surface area $VOHPO_4 \bullet 0.5H_2O$.

5. Activation of sol-gel prepared precursors in a mixture of n-butane and air increases the activity of the catalysts. The sol-gel prepared precursors synthesized in mixtures of toluene-tetrhydrofuran and 2-propanol-tetrahydrofuran are more selective than the traditionally prepared materials and than their analogues prepared in pure tetrahydrofuran. A higher selectivity is initially attributed to the increased amount of small crystallites observed in the scanning electron micrographs. However, the intrinsic activity of the catalysts is very different from the baseline

$(VO)_2P_2O_7$, indicating that the surface of the sol-gel prepared materials is different in nature. The origin of this difference is speculated to be the polymorphism of the observed surfaces.

6. Even though the precursors gelled in pure tetrahydrofuran and in a mixture of toluene with tetrahydrofuran did not feature remarkable differences in composition and catalytic performance, the morphology of the crystallites of the activated catalysts is different. Apparently, the activated materials from precursors gelled in toluene-tetrahydrofuran mixtures are comprised of small cubic crystallites that are not present in other materials. Interestingly, the amount of these small crystallites increased when the reaction was carried out for long periods of time (250 h). It is suggested that the presence of the small cubic crystallites allowed the observation with infrared spectroscopy of phosphates and vanadyl groups that are associated to one of the most accepted models for the active and selective surface.

6.3 Future work

Kinetic studies to establish the real influence of variables such as the concentration of oxygen, and the relationship between conversion and selectivity for the sol-gel prepared materials will also allow the comparison of their performance with other nanostructured catalysts reported in the literature. Catalyst evaluation during long periods of time will provide information about the influence of the equilibration process in the catalysts performance.

Transmission electron microscopy (TEM) studies of the small crystallites observed in this study will provide information about the arrangement of the crystalline planes within the cubic nanoparticles. This information will elucidate which planes are more exposed to the reaction and confirm information about the nature of the active site.

Variations on the heating process during the autoclave drying can provide some improvement on the reduction of vanadium towards the precursor. The optimal temperature and pressure for the reduction might be reached only a for few minutes, since the heating process is a continuous ramp. Determining those optimum values, as well as modifying the heating program (including one step in the ramp) may improve the amounts of precursor produced with low amounts of alcohol.

Exploring the use of other sources of vanadium and phosphorous as V^{4+} alkoxides and phosphorous alkoxides may lead to the direct synthesis of the precursor avoiding the reduction

steps. However the high pressure drying process may generate over-reduction of vanadium which can be detrimental for the catalytic activity.

References

[1] E. Bordes, Catal. Today 1 (1987) 499.

[2] F. Cavani, F. Trifiro, in: M. Baerns (Ed.), Basic Principles in Applied Catalysis, Springer-Veralg, Berlin Heidelberg, 2004, p. 19.

[3] B.K. Hodnett, Catal. Rev. -Sci. Eng. 27 (1985) 373.

[4] G. Centi, F. Cavani, F. Trifiro, in: G. Centi, F. Cavani,F. Trifiro (Eds.), Selective Oxidation by Heterogeneous Catalysis, Kluwer Academic/Plenum Publishers, New York City, 2001, p. 143.

[5] G.J. Hutchings, J. Mater. Chem. 14 (2004) 3385.

[6] N. Ballarini, F. Cavani, C. Cortelli, S. Ligi, F. Pierelli, F. Trifiro, C. Fumagalli, G. Mazzoni, T. Monti, Top. Catal. 38 (2006) 147.

[7] C. Yan, L. Sun, F. Cheng, in: Z.L. Wang, Y. Liu,Z. Zhang (Eds.), Handbook of Nanophase and Nanostructured Materials Vol. 1, Kluwer Academic/Plenum Publishers, New York City, 2003, p. 72.

[8] Inc Global Information. http://www.the-infoshop.com/study/mrc32066-maleic-anhydride.html, 2007.

[9] G. Centi, F. Trifiro, J.R. Ebner, V.M. Franchetti, Chem. Rev. 88 (1988) 55.

[10] G.J. Hutchings, J.K. Bartley, C. Rhodes, S.H. Taylor, R. Wells, D.J. Willock, in: I.T. Horváth (Ed.), Encyclopedia of Catalysis, John Wiley & Sons, Inc., Hoboken, 2003, p. 634.

[11] F. Cavani, F. Trifiro, Appl. Catal. A 157 (1997) 195.

[12] P.A. Agaskar, L. DeCaul, R.K. Grasselli, Catal. Lett. 23 (1994) 339.

[13] B. Schioett, K.A. Joergensen, R. Hoffmann, J. Phys. Chem. 95 (1991) 2297.

[14] G. Centi, F. Cavani, F. Trifiro, in: G. Centi, F. Cavani,F. Trifiro (Eds.), Selective Oxidation by Heterogeneous Catalysis., Kluwer Academic/ Plenum Publishers, New York, 2001, p. 368.

[15] B. Kubias, U. Rodemerck, H.-. Zanthoff, M. Meisel, Catal. Today 32 (1996) 243.

[16] Z. Xue, G.L. Schrader, J. Catal. 184 (1999) 87.

[17] Y. Kamiya, N. Hiyoshi, N. Ryumon, T. Okuhara, J. Mol. Catal. A: Chem. 220 (2004) 103.

[18] C.J. Kiely, A. Burrows, S. Sajip, G.J. Hutchings, M.T. Sananes, A. Tuel, J. Volta, J. Catal. 162 (1996) 31.

[19] L. O'Mahony, J. Henry, D. Sutton, T. Curtin, B.K. Hodnett, Appl. Catal. A 253 (2003) 409.

[20] S. Sajip, J.K. Bartley, A. Burrows, C. Rhodes, J. Claude Volta, C.J. Kiely, G.J. Hutchings, Phys. Chem. Chem. Phys. 3 (2001) 2143.

[21] S. Sajip, J.K. Bartley, A. Burrows, M. Sananes-Schulz, A. Tuel, J. Claude Volta, C.J. Kiely, G.J. Hutchings, New J. Chem. 25 (2001) 125.

[22] H.S. Horowitz, C.M. Blackstone, A.W. Sleight, G. Teufer, Appl. Catal. 38 (1988) 193.

[23] N. Hiyoshi, N. Yamamoto, N. Terao, T. Nakato, T. Okuhara, Stud. Surf. Sci. Catal. 130B (2000) 1715.

[24] M.A. Carreon, V.V. Guliants, F. Pierelli, F. Cavani, Catal. Lett. 92 (2004) 11.

[25] G.J. Hutchings, J.K. Bartley, J.M. Webster, J.A. Lopez-Sanchez, D.J. Gilbert, C.J. Kiely, A.F. Carley, S.M. Howdle, S. Sajip, S. Caldarelli, C. Rhodes, J.C. Volta, M. Poliakoff, J. Catal. 197 (2001) 232.

[26] G.J. Hutchings, J.A. Lopez-Sanchez, J.K. Bartley, J.M. Webster, A. Burrows, C.J. Kiely, A.F. Carley, C. Rhodes, M. Haevecker, A. Knop-Gericke, R.W. Mayer, R. Schloegl, J.C. Volta, M. Poliakoff, J. Catal. 208 (2002) 197.

[27] M.J. Ledoux, C. Crouzet, C. Pham-Huu, V. Turines, K. Kourtakis, P.L. Mills, J.J. Lerou, J. Catal. 203 (2001) 495.

[28] J.H. Holles, C.J. Dillon, J.A. Labinger, M.E. Davis, J. Catal. 218 (2003) 42.

[29] C.J. Dillon, J.H. Holles, M.E. Davis, J.A. Labinger, Catal. Today 81 (2003) 189.

[30] C.J. Dillon, J.H. Holles, R.J. Davis, J.A. Labinger, M.E. Davis, J. Catal. 218 (2003) 54.

[31] J.A. Lopez-Sanchez, L. Griesel, J.K. Bartley, R.P.K. Wells, A. Liskowski, D. Su, R. Schloegl, J. Volta, G.J. Hutchings, Phys. Chem. Chem. Phys. 5 (2003) 3525.

[32] Y. Kamiya, E. Nishikawa, T. Okuhara, T. Hattori, Appl. Catal. A 206 (2001) 103.

[33] R. Mallada, S. Sajip, C.J. Kiely, M. Menendez, J. Santamaria, J. Catal. 196 (2000) 1.

[34] S. Mota, M. Abon, J.C. Volta, J.A. Dalmon, J. Catal. 193 (2000) 308.

[35] N. Ballarini, F. Cavani, C. Cortelli, F. Gasparini, A. Mignani, F. Pierelli, F. Trifiro, C. Fumagalli, G. Mazzoni, Catal. Today 99 (2005) 115.

[36] M. Alonso, M.J. Lorences, G.S. Patience, A.B. Vega, F.V. Diez, S. Dahl, Catal. Today 104 (2005) 177.

[37] A. Cruz-Lopez, N. Guilhaume, S. Miachon, J. Dalmon, Catal. Today 107-108 (2005) 949.

[38] B. Munder, Y. Ye, L. Rihko-Struckmann, K. Sundmacher, Catal. Today 104 (2005) 138.

[39] Y. Ye, L. Rihko-Struckmann, B. Munder, K. Sundmacher, J. Electrochem. Soc. 153 (2006) D21.

[40] G.J. Hutchings, M.T. Sananes, S. Sajip, C.J. Kiely, A. Burrows, I.J. Ellison, J.C. Volta, Catal. Today 33 (1997) 161.

[41] R. Higgins, G.J. Hutchings, US Patent 4 317 777 (1982) to Imperial Chemical Industries Limited.

[42] Y. Kamiya, S. Ueki, N. Hiyoshi, N. Yamamoto, T. Okuhara, Catal. Today 78 (2003) 281.

[43] M.A. Carreon, V.V. Guliants, Chem. Mater. 14 (2002) 2670.

[44] B.G. Shpeizer, X. Ouyang, J.M. Heising, A. Clearfield, Chem. Mater. 13 (2001) 2288.

[45] A.C. Pierre, in: A.C. Pierre (Ed.), Introduction to Sol-Gel Processing., Kluwer Academic Publishers, Norwell, 1998, p. 242.

[46] S.A. Ennaciri, P. Bardoux, Mater. Sci. Forum 152-153 (1994) 331.

[47] D. Farrusseng, A. Julbe, M. Lopez, C. Guizard, Catal. Today 56 (2000) 211.

[48] C. R'kha, M.T. Vandenborre, J. Livage, R. Prost, E. Huard, J. Solid State Chem. 63 (1986) 202.

[49] S.A. Ennaciri, K. Malka, C. Louis, P. Barboux, C. R'kha, J. Livage, Phosphorus Res. Bull. 11 (2000) 87.

[50] S. Utamapanya, K.J. Klabunde, J.R. Schlup, Chem. Mater. 3 (1991) 175.

[51] R.O. Kuehl, in: R.O. Kuehl (Ed.), Design of experiments: statistical principles of research design and analysis, Brooks/Cole: Pacific Grove, Pacific Grove, 2000, p. 73.

[52] M. Nakamura, K. Kawai, Y. Fujiwara, J. Catal. 34 (1974) 345.

[53] AMI-200, Operations Manual, Altamira instruments, Pittsburgh.

[54] Y. Kamiya, N. Ryumon, H. Imai, T. Okuhara, Catal. Lett. 111 (2006) 159.

[55] P. Amoros, R. Ibanez, E. Martinez-Tamayo, A. Beltran-Porter, D. Beltran-Porter, G. Villeneuve, Mater. Res. Bull. 24 (1989) 1347.

[56] N. Yamamoto, N. Hiyoshi, T. Okuhara, Chem. Mater. 14 (2002) 3882.

[57] J.W. Johnson, A.J. Jacobson, J.F. Brody, S.M. Rich, Inorg. Chem. 21 (1982) 3820.

[58] J.W. Johnson, A.J. Jacobson, J.F. Brody, J.T. Lewandowski, Inorg. Chem. 23 (1984) 3842.

[59] M. Misawa, J. Chem. Phys. 93 (1990) 8401.

[60] J. El Haskouri, S. Cabrera, M. Roca, J. Alamo, A. Beltran-Porter, D. Beltran-Porter, M.D. Marcos, P. Amoros, Inorg. Chem. 38 (1999) 4243.

[61] S.J. Teichner, in: J. Fricke (Ed.), Aerogels, Sringer-Verlag, Berlin, 1986, p. 22.

[62] L. Griesel, J.K. Bartley, R.P.K. Wells, G.J. Hutchings, Catal. Today 99 (2005) 131.

[63] W. Dong, J.K. Bartley, N.F. Dummer, F. Girgsdies, D. Su, R. Schloegl, J. Volta, G.J. Hutchings, J. Mater. Chem. 15 (2005) 3214.

[64] L. Griesel, J.K. Bartley, R.P.K. Wells, G.J. Hutchings, J. Mol. Catal. A: Chem. 220 (2004) 113.

[65] B.E. Poling, J.M. Prausnitz, J.P. O'Connell, in: B.E. Poling, J.M. Prausnitz,J.P. O'Connell (Eds.), The properties of gases and liquids, McGraw-Hill, New York City, 2001, p. A-50.

[66] G. Busca, F. Cavani, G. Centi, F. Trifiro, J. Catal. 99 (1986) 400.

[67] N. Hiyoshi, N. Yamamoto, N. Ryumon, Y. Kamiya, T. Okuhara, J. Catal. 221 (2004) 225.

[68] N. Ryumon, H. Imai, Y. Kamiya, T. Okuhara, Appl. Catal. A 297 (2006) 73.

[69] Y.H. Taufiq-Yap, A.R.M. Hasbi, M.Z. Hussein, G.J. Hutchings, J. Bartley, N. Dummer, Catal. Lett. 106 (2006) 177.

[70] F. Cavani, F. Trifirò, in: M. Berns (Ed.), Basic Principles in Applied Catalysis, Springer-Verlag, Berlin Heidelberg, 2004, p. 21.

[71] J.K. Bartley, J.A. Lopez-Sanchez, G.J. Hutchings, Catal. Today 81 (2003) 197.

[72] R.O. Kuehl, in: R.O. Kuehl (Ed.), Design of experiments: statistical principles of research design and analysis, Brooks/Cole: Pacific Grove, Pacific Grove, 2000, p. 492.

[73] S. Albonetti, F. Cavani, S. Ligi, F. Pierelli, F. Trifiro, F. Ghelfi, G. Mazzoni, Stud. Surf. Sci. Catal. 143 (2002) 963.

[74] K. Katsumoto, D.M. Marquis, US Patent 4132670 (1979) to Chevron Research Co., USA.

[75] C.P. Hicks, C.L. Young, J. Chem. Soc., Faraday Trans. 2 73 (1977) 597.

[76] R.A. Heidemann, A.M. Khalil, AICHE J. 26 (1980) 769.

[77] M. Castier, S.I. Sandler, Chem. Eng. Sci. 52 (1997) 3393.

[78] M. Castier, S.I. Sandler, Chem. Eng. Sci. 52 (1997) 3579.

[79] L. Freitas, G. Platt, N. Henderson, Fluid Phase Equilib. 225 (2004) 29.

[80] N. Henderson, L. Freitas, G.M. Platt, AICHE J. 50 (2004) 1300.

[81] E.C. Carlson, Chem. Eng. Prog. 92 (1996) 35.

[82] D.S.H. Wong, S.I. Sandler, AICHE J. 38 (1992) 671.

[83] D.S.H. Wong, H. Orbey, S.I. Sandler, Ind. Eng. Chem. Res. 31 (1992) 2033.

[84] R. Stryjek, J.H. Vera, Can. J. Chem. Eng. 64 (1986) 323.

[85] J.M. Prausnitz, R.N. Lichtenthaler, Gomes de Acevedo, E., Molecular Thermodynamics of Fluid Phase Equilibria, Prentice-Hall, Inc, Upper Saddle River, 1999, p. 860.

[86] M. Hirata, S. Ohe, K. Nagahama, Computer Aided Data Book of Vapor-Liquid Equilibria, Kodansha Ltd., Tokyo, 1975, p. 339.

[87] H. Orbey, S.I. Sandler, Int. J. Thermophys. 16 (1995) 695.

[88] Z. Zhang, F. Zhou, E.J. Lavernia, Metall. Mat. Trans. A Phys. Metall. Mat. Sci. 34A (2003) 1349.

[89] C.E. Krill, R. Birringer, Philos. Mag. A 77 (1998) 621.

[90] X.L. Wang, J.L. Robertson, in: Z.L. Wang, Y. Liu,Z. Zhang (Eds.), Handbook of Nanophase and Nanostructured Materials Vol. 2, Kluwer Academic/Plenum Publishers, New York City, 2003, p.1.

[91] B.E. Warren, X-ray diffraction, Addison-Wesley Pub. Co, Reading, Mass., 1969, p. 381.

[92] C.J. Kiely, A. Burrows, G.J. Hutchings, K.E. Bere, J.C. Volta, A. Tuel, M. Abon, Faraday Discuss. 105 (1996) 103.

[93] TOPAS V. 2.1, User's Manual, Bruker AXS, Karlsruhe, 2003, p. 79.

[94] J.I. Langford, NIST Special Publication 846 (1992) 110.

[95] TOPAS V. 2.1, Tutorial, Bruker AXS, Karlsruhe, 2003, p. 86.

[96] K.T. Ranjit, K.J. Klabunde, Chem. Mater. 17 (2005) 65.

[97] J. Wisniak, H. Segura, R. Reich, Ind. Eng. Chem. Res. 35 (1996) 3742.

[98] C.C. Kao, R.N. Miller, J.F. Sturgis, J. Chem. Eng. Data 46 (2001) 229.

[99] P.H. Van Konynenburg, R.L. Scott, Philos. Trans. R. Soc. London, Ser. A 298 (1980) 495.

[100] S.A. Ennaciri, K. Malka, C. Louis, P. Barboux, C. R'Kha, J. Livage, Catal. Lett. 62 (1999) 79.

[101] H. Bluhm, M. Haevecker, E. Kleimenov, A. Knop-Gericke, A. Liskowski, R. Schloegl, D.S. Su, Top. Catal. 23 (2003) 99.

[102] V.V. Guliants, S.A. Holmes, J.B. Benziger, P. Heaney, D. Yates, I.E. Wachs, J. Mol. Catal. A: Chem. 172 (2001) 265.

[103] N. Ballarini, F. Cavani, C. Cortelli, M. Ricotta, F. Rodeghiero, F. Trifiro, C. Fumagalli, G. Mazzoni, Catal. Today 117 (2006) 174.

[104] Z. Xue, G.L. Schrader, J. Phys. Chem. B 103 (1999) 9459.

[105] E. Kleimenov, H. Bluhm, M. Haevecker, A. Knop-Gericke, A. Pestryakov, D. Teschner, J.A. Lopez-Sanchez, J.K. Bartley, G.J. Hutchings, R. Schloegl, Surf. Sci. 575 (2005) 181.

[106] N. Duvauchelle, E. Bordes, Catal. Lett. 57 (1999) 81.

[107] P.L. Gai, K. Kourtakis, D.R. Coulson, G.C. Sonnichsen, J. Phys. Chem. B 101 (1997) 9916.

[108] P.L. Gai, K. Kourtakis, Science 267 (1995) 661.

[109] S.D. Ross, Inorganic infrared and Raman spectra, McGraw-Hill, London, New York, 1972, p. 414.

[110] K.L. Butcher, M.S. Medani, J. Appl. Chem. 18 (1968) 100.

[111] C. Schmitt. http://saber.towson.edu/~schmitt/pyro/chapter5.html, 1996.

[112] A.P. Grosvenor, B.A. Kobe, N.S. McIntyre, Surf. Sci. 574 (2005) 317.

[113] I.Z. Babievskaya, N.F. Drobot, K.S. Gavrichev, V.A. Krenev, R.K. Idiatulov, V.L. Tsiperman, S.V. Korostin, Y.V. Permyakov, A.A. Vishnev, Inorg. Mater. (Transl. of Neorg. Mater.) 40 (2004) 35.

[114] N.F. Drobot, I.Z. Babievskaya, K.S. Gavrichev, N.A. Ovchinnikova, O.A. Noskova, V.A. Krenev, Inorg. Mater. (Transl. of Neorg. Mater.) 38 (2002) 501.

[115] I. Yamashita, M. Shimizu, JP Patent 50105562 (1975) to Asahi Chemical Industry Co., Ltd., Japan.

[116] A. Usui, JP Patent 2004292 (1990) to Mycoal Warmers Company Limited, Japan.

[117] B.E. Yoldas, US Patent 4465739 (1984) to Westinghouse Electric Corp., USA.

[118] F. Suzuki, K. Onozato, Y. Kurokawa, J. Non Cryst. Solids 94 (1987) 160.

[119] T. Fujita, T. Yamaguchi, N. Takusaagawa, K. Kitajima, J. Ceram. Soc. Jpn. 106 (1998) 1242.

[120] S.J. Lee, J. Mater. Sci. 39 (2004) 5833.

Appendix A Gas chromatograph calibration

The equations of calibration for the gas chromatography techniques are based in the areas of the responses of the thermal conductivity and flame ionization detectors. For the CO, CO_2 and n-butane the areas of the peaks from the TCD chromatogram related to the area of N_2. In Equation A. 1 CF_{gas} stands for calibration factor

$$\frac{Area\ gas}{Area\ N_2} = CF_{gas}\frac{Moles\ gas}{Moles\ N_2}$$

Equation A. 1

For the case of the maleic anhydride in the FID the area of the peak of the anhydride is related to that of the n-butane in Equation A. 2 where P_{v62} is the vapor pressure of Maleic anhydride at the water bath and P_T is the total pressure of the saturator-GC system and x_{C4} is the molar fraction of n-butane in the gas phase.

$$\frac{Area\ MA}{Area\ C_4} = CF_{MA}\frac{Moles\ MA}{Moles\ C_4} = CF_{MA}\frac{P_{v62^0C}}{\left(P_T - P_{v62^0C}\right)x_{C_4}}$$

Equation A. 2

A summary of the results of calibration factors is presented in Table A. 1. This is the result of at least four measurements of the standards and fitting with a least squares routine.

Table A. 1 Summary of calibration factors for the catalysts evaluation experiments

Gas	CF
CO	1.097
CO_2	0.67
n-butane	1.03
Maleic Anhydride	1.925

Appendix B Prediction of VLE at high pressures for a binary mixture

B.1 Determination of binary interaction parameters

The mixture to be evaluated is methanol (1) and benzene (2); it was selected due to the available data for low and high pressure. In general the procedure to determine the binary interaction parameters for the activity coefficient model and for the second virial coefficient is the same as the procedure used in section A. The low-pressure data used to determine the binary interaction parameters are reported in the literature at 55^{o}C [86]. For this system the NRTL model was employed as the activity coefficient model and the minimization process was stared with α=1, g_{12}=g_{21}= 2727 J/mol (or the same as RT) as suggested by the literature [87]. The values of the NRTL model after the minimization are α=0.27376, g_{12}=1829.7 J/mol and g_{21}= 4517.3 J/mol. The set k_{12} calculated to satisfy the g^E condition are shown in Figure B. 1 a). It is interesting to observe that for this case there is not considerable distinction in the value of k_{12} that generate the lowest average values in the differences of g^E, P_{err} and y_{err} and it corresponds to the value for x_1=0.5, i.e. k_{12}=0.3168. For the purpose of this appendix, which is determining if the selecting criteria for k_{12} is appropriate, the values of k_{12} 0.25, 0.3168 and 0.45 were employed to represent the VLE using the pure fugacity coefficient model with PRSV EOS WS. Predicted temperature and vapor phase composition are presented in Figure B. 2. Again we observed that the best representation is for pressure and that it is observed for k_{12}=0.3168. The other two values yield poor predictions of the equilibrium pressure and will provide some ideas on the accuracy of the chosen parameter when predicting VLE at high pressures.

B.2 Comparison with experimental data at high pressures

Results of this part are presented in Figure B. 3, and compared with experimental data reported in the literature [110]. It should be noticed that the parameters that best predicted the data at low pressures also do it at high pressures. Predicted bubble and dew pressures in Figure B. 3 for k_{12}=0.45 or k_{12}=0.25 do not fit the experimental data very well, the former yields non

differentiable sections at T=220°C which could be wrongly assigned to the expectation of critical point vicinity in the absence of experimental evidence. Even though the predicted values from k_{12}=0.25 could be looked as an acceptable representation of the experimental data, the best fit is observed for k_{12}=0.3168. It is important to notice that this value is in agreement with the reported by Wong and Sandler in their early work with the mixing rule (0.309)[83]. We can imply from this example that the accurate representation of the experimental data at low pressures along with the conformity of the g^E calculation based on an activity coefficient model and the EOS model can provide accurate estimative of VLE data at high pressures.

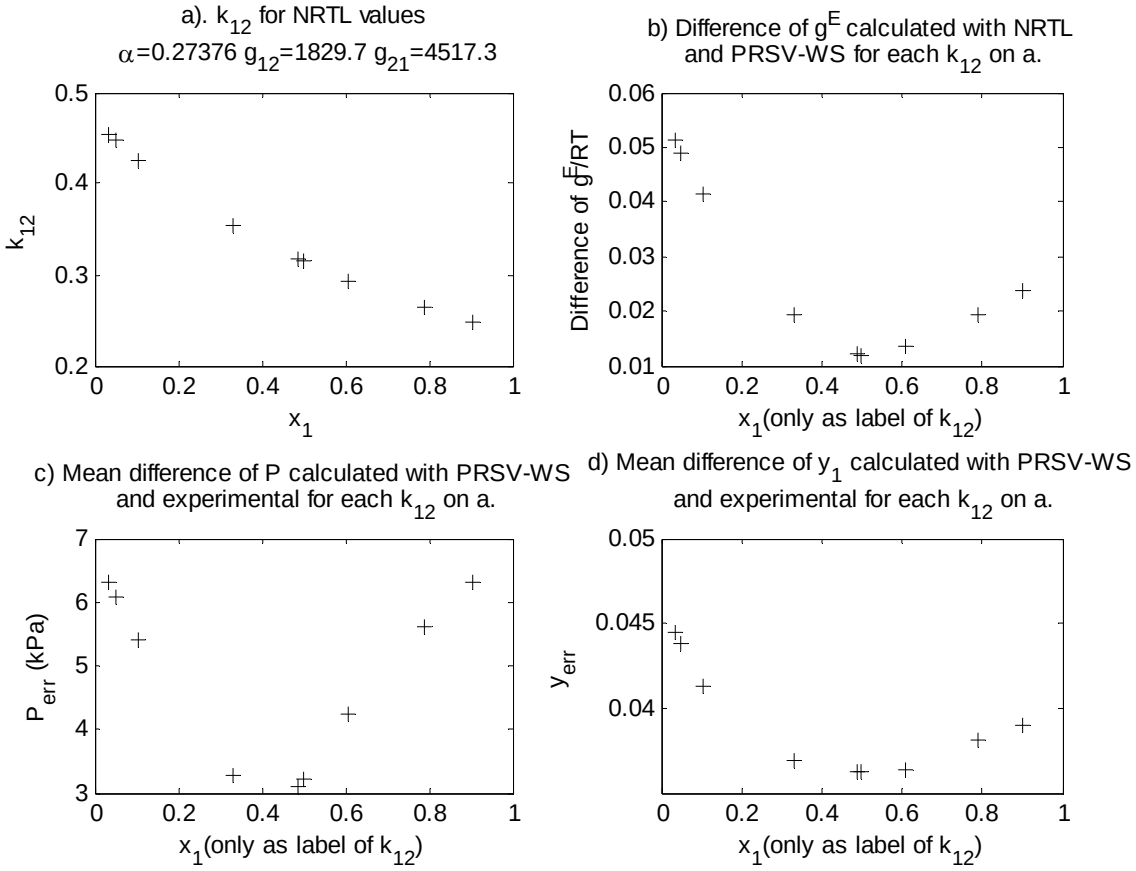

Figure B. 1 Determination of k_{12} that best predicts experimental data at low pressure with PRSV EOS and WS mixing rule for a mixture of methanol(1) and benzene(2)

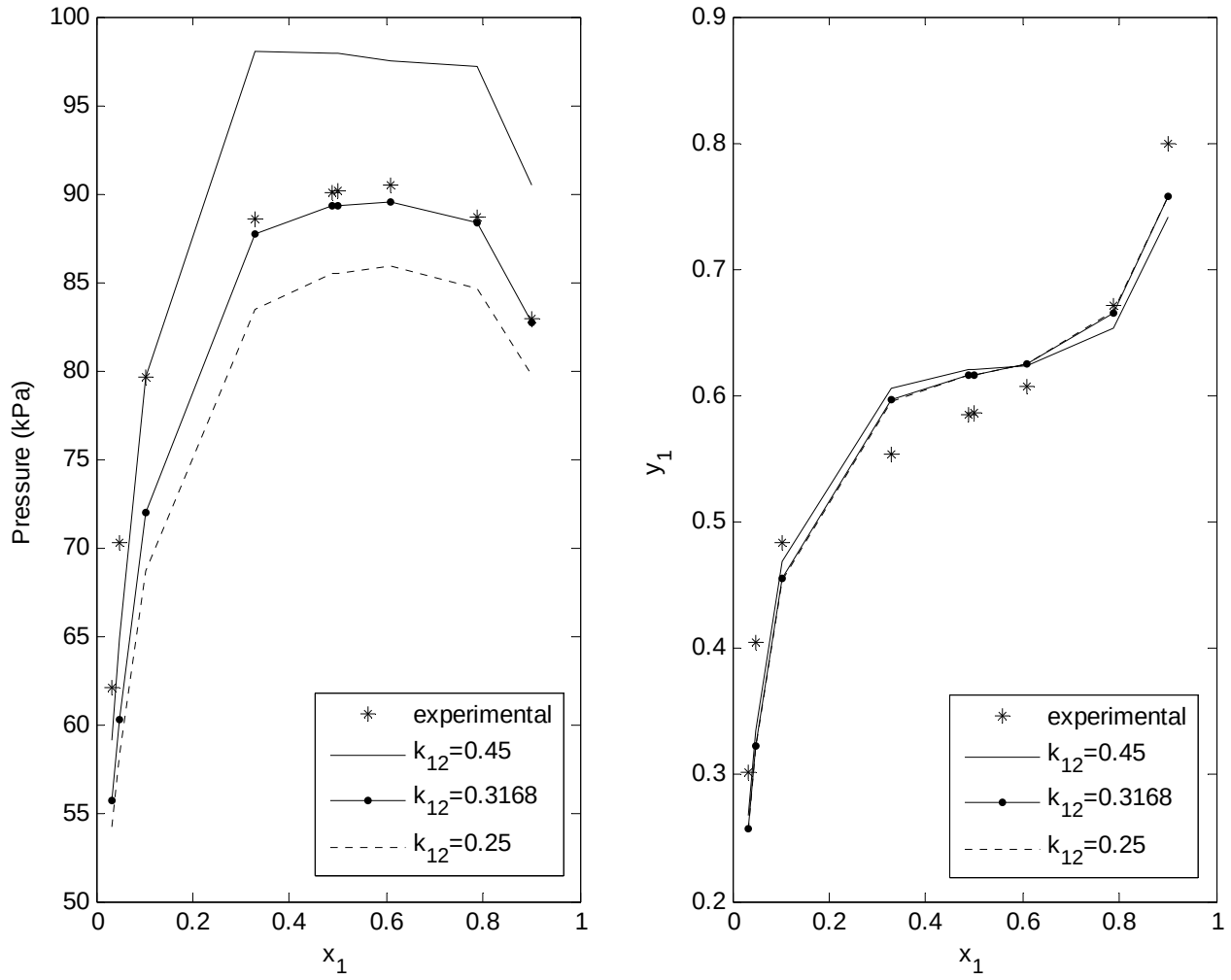

Figure B. 2 Prediction of low pressure VLE data for methanol-benzene mixture with PRSV EOS and WS mixing rule for three different k_{12}

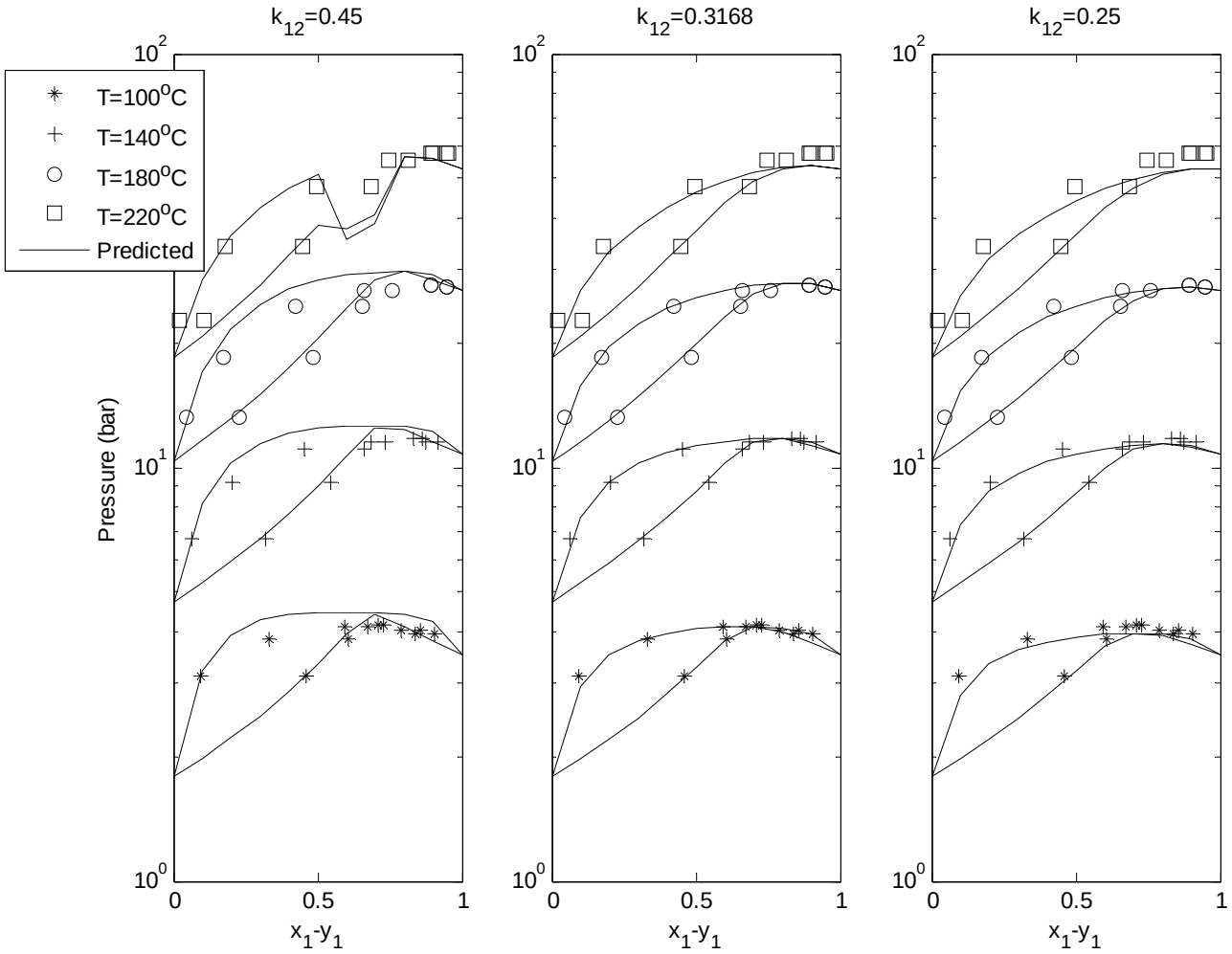

Figure B. 3 Comparison of high pressure VLE experimental data for methanol-benzene mixture with predicted with PRSV EOS and WS mixing rule for three different k_{12}

B.3 Computer routines to estimate VLE of binary mixtures

B.3.1 Summary of routines

The calculation was performed using the available software MATLAB. A summary of all the routines employed for the estimation of VLE data for binary mixtures with the PRSV EOS and the WS mixing rule is presented in Table B. 1 . A brief description is included along with the information that is required to be input to each routine. The routines are required to be run in the order 1, 2, 3 and 4. For routine 1 all the subroutines must be updated by typing the data or parameters shown in the required information column. Routines 2, 3 and 4 can be run without updating their subroutines since they are already updated for routine 1, only the required information is necessary to be typed.

Table B. 1Summary of computer routines employed for the estimation of VLE of binary mixtures with a PRSV EOS and a WS mixing rule

No.	m-file	Description	Required Information
1	kijWSbinarygood.m	Minimizes the maximum temperature or pressure error (calculated by routine 1.1) by changing the binary interaction parameters. Uses a simplex method.	Estimation of binary interaction parameters from experimental data fitted to any activity coefficient model or appropriate estimations. Name of the subroutine 1.1 to be used in the optimization.
1.1	presserror.m (for 2-propanol-THF) presserrornrtl.m (for methanol-benzene)	Calculates the equilibrium temperature or pressure using the fugacity coefficient model for each of the values of k_{12} generated by routine 1.1.1 and solving Equation 4.11. Calculates the error (Equation 4.12 and pressure analogous) by comparing with experimental data at low pressure. Generates the maximum value of the error among the calculation for all the k_{12} values	Experimental data of a low pressure isobar: equilibrium molar liquid composition, molar vapor composition and temperature.

1.1.1	kijWSbinary1fthf.m (for 2-propanol-THF) kijWSbinary1f.m (for methanol-benzene)	Calculates the excess Gibbs free energy from the EOS model (g^E_{EOS}). Calculates the values of k_{12} that satisfy the WS mixing rule condition ($g^E_{EOS}=g^E_{AC}$) employing a bisection algorithm as convergence method. Generates one k_{12} per each experimental point provided.	Experimental data of a low pressure isobar: equilibrium molar liquid composition and temperature Critical constants, accentric factor and k_1 for SV modification of PR EOS
1.1.1.1	alpha.m	Calculates the "a" parameter for the PR EOS according to SV modification for each component.	
1.1.1.2	gert.m (for 2-propanol-THF) gertnrtl.m (for methanol-benzene)	Calculates the excess Gibbs free energy (g^E_{AC}) from a Wilson model or from a NRTL model.	
1.1.2	phinithf.m (for 2-propanol-THF) phini.m (for methanol-benzene)	Calculates the fugacity coefficient using the EOS model	Critical constants, accentric factor and k_1 for SV modification of PR EOS
2	kijWSbinary1thf.m (for 2-propanol-THF) kijWSbinary1.m	Uses routines 1.1.1 and 1.1.2 to calculate the k_{12} values that satisfy $g^E_{EOS}=g^E_{AC}$ condition. Calculates the equilibrium at low pressures and additionally calculates the error in the calculation of the molar composition of the vapor phase. Generates the plots of the encountered k_{12}, the errors on temperature, molar vapor phase composition and the error of the $g^E_{EOS}=g^E_{AC}$ for each k_{12}. From this plots the values of k_{12} that generate the minimum errors are picked and compare with the experimental data to choose the one that best represent them.	Experimental data of a low pressure isobar: equilibrium molar liquid composition, molar vapor composition and temperature. Critical constants, accentric factor and k_1 for SV modification of PR EOS Binary interaction parameters calculated with routine 1

3	thf2propmT.m (for 2-propanol-THF) metholbenzmT.m (for methanol-benzene)	Calculates and plots the equilibrium pressure using the PRSV EOS and WS mixing rule for different temperatures to analyze the behavior or to compare with experimental data (P-x-y diagrams). When analysis of the behavior is required the plots are used to locate the compositions at which the unrealistic data shows up suggesting the presence of critical points	Binary interaction parameters and k_{12} selected with routine 2. Antoine constants for the two compounds Experimental data at high pressure for comparison or. Desired temperatures for the evaluation.
3.1	BubPbin.m	Calculates the bubble pressure of a binary mixture according to traditional algorithms	
3.2	DewPbin.m	Calculates the dew pressure of a binary mixture according to traditional algorithms	
4	thf2prop.m	Calculates and plots the P-T diagrams for the desired total molar fractions used in the autoclave drying or determined with routine 3	Binary interaction parameters and k_{12} selected with routine 2. Antoine constants for the two compounds Desired total molar compositions for the evaluation. Autoclave readings of temperature and pressure

B.3.2 Routine Codes

In this section the program codes for MATLAB are presented the text in bold represent data that needs to be typed in order to update the code before running. These m-files are intended for binary mixtures whose critical loci have not been either experimentally or rigorously determined and when the VLE experimental data are available at low pressures.

kijWSbinarygood.m

```
clc
clear
%options=optimset('MaxFunEvals',900);
[y,val,exitflag]=fminsearch('presserrornrtl',[1 2727 2727])
```

presserror.m

```
function Terr=presseror(par)
par
% for all this routine will use 1 for THF and 2 for 2-propanol
P=101325;
y=[0.105 0.1957 0.346 0.465 0.5651 0.651 0.7279 0.7991 0.8672 0.9336 0.967];
x1=[0.05 0.1 0.2 0.3 0.4 0.5 0.6 0.7 0.8 0.9 0.95];
T=[80.73 79.4 77.18 75.3 73.54 71.85 70.34 69.02 67.85 66.74 66.24]+273.15;
kijf=kijWSbinary1fthf(par);
for j=1:length(x1)
   Ts1=T;
   Ts2=T*0.5;
   par=[par(1) par(2) kijf(j)];
   for i=1:length(x1)
      Ts11=Ts1(i);
      Ts22=Ts2(i);
      err=1;
      while abs(err)>0.0001
         ph1(i,:)=phinithf(Ts11,P,x1(i),par,1);
         ph2(i,:)=phinithf(Ts22,P,x1(i),par,1);
         err1=1-(ph1(i,2)+x1(i)*(ph1(i,1)-ph1(i,2)));
         err2=1-(ph2(i,2)+x1(i)*(ph2(i,1)-ph2(i,2)));
         Ts=-err1*(Ts22-Ts11)/(err2-err1)+Ts11;
         ph(i,:)=phinithf(Ts,P,x1(i),par,1);
         err=1-(ph(i,2)+x1(i)*(ph(i,1)-ph(i,2)));
         if err<0
            Ts11=Ts;
         else
            Ts22=Ts;
         end
      end
      Tcalc(i)=Ts;
      phf(i,:)=ph(i,:);
      yf1(i)=x1(i)*ph(i,1);
   end
   j;
   Terr2=T-Tcalc;
   Terr1(j)=mean(abs(T-Tcalc));
end
Terr=max(Terr1)
```

presserrornrtl.m

```
function Perr=presserrornrtl(par)
par
T=55+273.15;
%for methanol benzene
```

```
y2=[0.3019 0.4051 0.4841 0.554 0.5845 0.5858 0.6078 0.6716 0.7997];
x1=[0.034 0.0493 0.1031 0.3297 0.4874 0.4984 0.6076 0.7896 0.9024];
P2=[465.84 527.12 597.48 664.24 675.62 675.99 678.44 664.91 622.29]*1.333E2;
kijf=kijWSbinary1f(par);
for j=1:length(x1)
   Ps1=P2*1.5;
   Ps2=P2*0.5;
   par=[par(1) par(2) par(3) kijf(j)];
   for i=1:length(x1)
      Ps11=Ps1(i);
      Ps22=Ps2(i);
      err=1;
      while abs(err)>0.0001
         ph1(i,:)=phini(T,Ps11,x1(i),par,1);
         ph2(i,:)=phini(T,Ps22,x1(i),par,1);
         err1=1-(ph1(i,2)+x1(i)*(ph1(i,1)-ph1(i,2)));
         err2=1-(ph2(i,2)+x1(i)*(ph2(i,1)-ph2(i,2)));
         Ps=-err1*(Ps22-Ps11)/(err2-err1)+Ps11;
         ph(i,:)=phini(T,Ps,x1(i),par,1);
         err=1-(ph(i,2)+x1(i)*(ph(i,1)-ph(i,2)));
         if err<0
            Ps11=Ps;
         else
            Ps22=Ps;
         end
      end
      Pcalc(i)=Ps;
      phf(i,:)=ph(i,:);
      yf1(i)=x1(i)*ph(i,1);
   end
   j;
   Perr2=P2-Pcalc;
   Perr1(j)=mean(abs(P2-Pcalc));
end
Perr=max(Perr1)
```

kijWSbinary1fthf.m

```
function akij=kijWSbinary1fthf(par)
% for all this routine will use 1 for THF and 2 for 2-propanol and P const
x2=[0.05 0.1 0.2 0.3 0.4 0.5 0.6 0.7 0.8 0.9 0.95]; % for thf and 2-propanol
T2=[80.73 79.4 77.18 75.3 73.54 71.85 70.34 69.02 67.85 66.74 66.24]+273.15;
R=8.31451;%J/(mol*K)
%for thf and 2-propanol
Tc=[540.1 508.4];
Pc=[51.9 47.6425]*1E5;
w=[0.2255 0.66372];
```

```
k1=[0.03961 0.23264];
% for thf and 2 propanol with Wilson equation
l12=par(1);
l21=par(2);
b=0.077796*R*Tc./Pc;
for q=1:length(x2)
   x1=x2(q);
   x=[x1 1-x1];
   % for thf and 2-propanol
   T=T2(q);
   P=101325;
   gertac=gert(x,l12,l21)
   a=alpha(T,Tc,Pc,w,k1,R);
   D=P;
   E=(D*b-R*T);
   F=-3*D*b.^2-2*R*T*b+a;
   G=D*b.^3-a.*b+R*T*b.^2;
   r1=roots([D E(1) F(1) G(1)]);
   r2=roots([D E(2) F(2) G(2)]);
   for i=1:3
         if r1(i)<0
            r1(i)=0;
         end
         if r2(i)<0
            r2(i)=0;
         end
   end
   v=[min(nonzeros(r1)) min(nonzeros(r2))];%
   A1=x*(log(v./(v-b)))';
   A2=(1/(R*T))*x*(a./(2*(2)^0.5*b).*log((v+b*(1-2^0.5))./(v+b*(1+2^0.5))))';
   A3=x*(P*v/(R*T)-1)'-x*(log(P*v/(R*T)))';
   B2=A1+A2+A3;
   kij=[-0.9:0.1:0.9];
   error1=1;
   count=1;
   while abs(error1)>0.000001
      for j=1:length(kij)
         A=b(1)-a(1)/(R*T);
         B=b(2)-a(2)/(R*T);
         C=a./b;
         svc=(x(1)^2*A+x(2)^2*B)+(x(1)*x(2)*(A+B))*(1-kij(j));
         bm=svc/(1-gertac/(-0.623225240147)-(x*C')/(R*T));
         am=bm*(x*C'+gertac*R*T/(-0.623225240147));
         D=P;
         E=(D*bm-R*T);
         F=-3*D*bm^2-2*R*T*bm+am;
```

```
            G=D*bm^3-am*bm+R*T*bm^2;
            r=roots([D E F G]);
            for i=1:3
               if r(i)<0
                  r(i)=0;
               end
            end
            vm=min(nonzeros(r));
            A4=log(vm/(vm-bm));
            A5=(1/(R*T))*am/(2*(2)^0.5*bm)*log((vm+bm*(1-
2^0.5))/(vm+bm*(1+2^0.5)));
            A6=P*vm/(R*T)-1-log(P*vm/(R*T));
            gereos=(A4+A5+A6-B2);
            error(j)=gereos-gertac;
         end
         for j=2:length(kij)
            if error(j)>0
                  if error(j-1)<0
                     kijc=kij(j);
                     clave=j;
                     error1=error(j);
                  end
            end
         end
         kij=[kij(clave-1):0.1/(10^count):kij(clave)];
         count=count+1;
      end
      kijf(q)=kijc;
      errorf(q)=error1;
      ger(q)=gereos;
   end
   akij=kijf;
```

kijWSbinary1f.m

```
   function akij=kijWSbinary1f(par)
   %for methanol (1) and benzene (2) using an isotherm
   x2=[0.034 0.0493 0.1031 0.3297 0.4874 0.4984 0.6076 0.7896 0.9024];
   P2=[465.84 527.12 597.48 664.24 675.62 675.99 678.44 664.91 622.29]*1.333E2;
   R=8.31451;%J/(mol*K)
   % for methanol and benzene
   Tc=[512.58 562.16];
   Pc=[80.9579 48.98]*1E5;
   w=[0.56533 0.20929];
   k1=[-0.16816 0.07019];
   % for methanol and benzene with NRTL
   al=par(1);
```

```
g12=par(2);
g21=par(3);
b=0.077796*R*Tc./Pc;
for q=1:length(x2)
   x1=x2(q);
   x=[x1 1-x1];
   % for methanol cyclohexane/benzene
   T=55+273.15;
   P=P2(q);
   gertac=gertnrtl(T,x,al,g12,g21);
   a=alpha(T,Tc,Pc,w,k1,R);
   D=P;
   E=(D*b-R*T);
   F=-3*D*b.^2-2*R*T*b+a;
   G=D*b.^3-a.*b+R*T*b.^2;
   r1=roots([D E(1) F(1) G(1)]);
   r2=roots([D E(2) F(2) G(2)]);
   for i=1:3
         if r1(i)<0
            r1(i)=0;
         end
         if r2(i)<0
            r2(i)=0;
         end
   end
   v=[min(nonzeros(r1)) min(nonzeros(r2))];%
   A1=x*(log(v./(v-b)))';
   A2=(1/(R*T))*x*(a./(2*(2)^0.5*b).*log((v+b*(1-2^0.5))./(v+b*(1+2^0.5))))';
   A3=x*(P*v/(R*T)-1)'-x*(log(P*v/(R*T)))';
   B2=A1+A2+A3;
   kij=[-0.9:0.1:0.9];
   error1=1;
   count=1;
   while abs(error1)>0.000001
      for j=1:length(kij)
         A=b(1)-a(1)/(R*T);
         B=b(2)-a(2)/(R*T);
         C=a./b;
         svc=(x(1)^2*A+x(2)^2*B)+(x(1)*x(2)*(A+B))*(1-kij(j));
         bm=svc/(1-gertac/(-0.623225240147)-(x*C')/(R*T));
         am=bm*(x*C'+gertac*R*T/(-0.623225240147));
         D=P;
         E=(D*bm-R*T);
         F=-3*D*bm^2-2*R*T*bm+am;
         G=D*bm^3-am*bm+R*T*bm^2;
         r=roots([D E F G]);
```

```
            for i=1:3
               if r(i)<0
                  r(i)=0;
               end
            end
            vm=min(nonzeros(r));
            A4=log(vm/(vm-bm));
            A5=(1/(R*T))*am/(2*(2)^0.5*bm)*log((vm+bm*(1-
2^0.5))/(vm+bm*(1+2^0.5)));
            A6=P*vm/(R*T)-1-log(P*vm/(R*T));
            gereos=(A4+A5+A6-B2);
            error(j)=gereos-gertac;
         end
         for j=2:length(kij)
            if error(j)>0
                  if error(j-1)<0
                     kijc=kij(j);
                     clave=j;
                     error1=error(j);
                  end
            end
         end
         kij=[kij(clave-1):0.1/(10^count):kij(clave)];
         count=count+1;
      end
      kijf(q)=kijc;
      errorf(q)=error1;
      ger(q)=gereos;
   end
   akij=kijf;
```

alpha.m

```
function a=alpha(T,Tc,Pc,w,k1,R)
k0=0.378893+1.4897153*w-0.17131848*w.^2+0.0196554*w.^3;
k=k0+k1.*(1+(T./Tc).^0.5).*(0.7-T./Tc);
al=(1+k.*(1-(T./Tc).^0.5)).^2;
a=0.457235*R^2*Tc.^2./Pc.*al;
```

gert.m

```
function a=gert(x,l12,l21)
a=-x(1)*log(x(1)+l12*x(2))-x(2)*log(x(2)+l21*x(1));
```

gertnrtl.m

```
function a=gertnrtl(T,x,alpha,g12,g21)
R=8.31451;
```

```
t12=g12/(R*T);
t21=g21/(R*T);
G12=exp(-alpha*t12);
G21=exp(-alpha*t21);
a=x(1)*x(2)*(t21*G21/(x(1)+x(2)*G21)+t12*G12/(x(2)+x(1)*G12));
```

phinithf.m

```
function phi=phinithf(T,P,x,par,ph)
%ph 1 for liquid and 2 for vapor
x1=[x 1-x];
R=8.31451;
%for thf 2propanol
Tc=[540.1 508.4];
Pc=[51.9 47.6425]*1E5;
w=[0.2255 0.66372];
k1=[0.03961 0.23264];
l12=par(1);
l21=par(2);
kij=par(3);

b=0.077796*R*Tc./Pc;
a=alpha(T,Tc,Pc,w,k1,R);

%for thf and 2-propanol
lngdAdn=log(actcoef(x1(1),l12,l21));
gertac=gert(x1,l12,l21);


C1=-0.623225240147;
dnDdn=(a./b)/(R*T)+lngdAdn/C1;
A=b(1)-a(1)/(R*T);
B=b(2)-a(2)/(R*T);
C=(A+B)/2*(1-kij);
ABC=[A C;C B];
dn2Q=2*(x1*ABC);
Q=(x1(1)^2*A+x1(2)^2*B)+(x1(1)*x1(2)*(A+B))*(1-kij);
D=x1*(a./b)'/(R*T)+gertac/C1;
dnbm=1/(1-D)*dn2Q-Q/(1-D)^2*(1-dnDdn);
bm=Q/(1-D);
am=R*T*bm*D;
dn2am=(R*T)*(D*dnbm+bm*dnDdn);
D=P;
E=(D*bm-R*T);
F=-3*D*bm^2-2*R*T*bm+am;
G=D*bm^3-am*bm+R*T*bm^2;
r=roots([D E F G]);
```

```
for i=1:3
      if r(i)<0
          r(i)=0;
      end
      if imag(r(i))~=0
         r(i)=0;
      end
end
if ph==1
   vm=min(nonzeros(r));
else
   vm=max(nonzeros(r));
end
H=-log(P*(vm-bm)/(R*T));
I=dnbm/bm*(P*vm/(R*T)-1);
J=1/(2*2^0.5)*(am/(bm*R*T))*(1/am*dn2am-1/bm*dnbm);
K=log((vm+bm*(1-2^0.5))/(vm+bm*(1+2^0.5)));
lnphi=H+I+J*K;
phi=exp(lnphi);
phi(3)=vm;
```

phini.m

```
function phi=phini(T,P,x,par,ph)
%ph 1 for liquid and 2 for vapor
x1=[x 1-x];
R=8.31451;
% for methanol benzene
Tc=[512.58 562.16];
Pc=[80.9579 48.98]*1E5;
w=[0.56533 0.20929];
k1=[-0.16816 0.07019];
alpha1=par(1);
g12=par(2);
g21=par(3);
kij=par(4);
b=0.077796*R*Tc./Pc;
a=alpha(T,Tc,Pc,w,k1,R);
%for methanol benzene
lngdAdn=log(actcoefcnrtl(T,x1(1),alpha1,g12,g21));
gertac=gertnrtl(T,x1,alpha1,g12,g21);
C1=-0.623225240147;
dnDdn=(a./b)/(R*T)+lngdAdn/C1;
A=b(1)-a(1)/(R*T);
B=b(2)-a(2)/(R*T);
C=(A+B)/2*(1-kij);
ABC=[A C;C B];
```

```
dn2Q=2*(x1*ABC);
Q=(x1(1)^2*A+x1(2)^2*B)+(x1(1)*x1(2)*(A+B))*(1-kij);
D=x1*(a./b)'/(R*T)+gertac/C1;
dnbm=1/(1-D)*dn2Q-Q/(1-D)^2*(1-dnDdn);
bm=Q/(1-D);
am=R*T*bm*D;
dn2am=(R*T)*(D*dnbm+bm*dnDdn);
D=P;
E=(D*bm-R*T);
F=-3*D*bm^2-2*R*T*bm+am;
G=D*bm^3-am*bm+R*T*bm^2;
r=roots([D E F G]);
for i=1:3
      if r(i)<0
          r(i)=0;
      end
      if imag(r(i))~=0
         r(i)=0;
      end
end
if ph==1
   vm=min(nonzeros(r));
else
   vm=max(nonzeros(r));
end
H=-log(P*(vm-bm)/(R*T));
I=dnbm/bm*(P*vm/(R*T)-1);
J=1/(2*2^0.5)*(am/(bm*R*T))*(1/am*dn2am-1/bm*dnbm);
K=log((vm+bm*(1-2^0.5))/(vm+bm*(1+2^0.5)));
lnphi=H+I+J*K;
phi=exp(lnphi);
phi(3)=vm;
```

kijWSbinary1thf.m

```
clc
clear

% this routine presents the results of the binary parameters determination

%VLE experimental data

% for all this routine we will use 1 for THF and 2 for 2-propanol using an
% isobar
P=101325;
y=[0.105 0.1957 0.346 0.465 0.5651 0.651 0.7279 0.7991 0.8672 0.9336 0.967];
x1=[0.05 0.1 0.2 0.3 0.4 0.5 0.6 0.7 0.8 0.9 0.95]; % for thf and 2-propanol
```

```
T2=[80.73 79.4 77.18 75.3 73.54 71.85 70.34 69.02 67.85 66.74 66.24]+273.15;


%substance properties

R=8.31451;%J/(mol*K)
%for thf and 2-propanol
Tc=[540.1 508.4];
Pc=[51.9 47.6425]*1E5;
w=[0.2255 0.66372];
k1=[0.03961 0.23264];

% binary interaction parameters

% for thf and 2 propanol with Wilson equation
par=[1.3477 0.65701];
l12=par(1);
l21=par(2);

b=0.077796*R*Tc./Pc;
kijf=kijWSbinary1fthf(par);
for j=1:length(x1)

   % error between experimental data and EOS VLE calculation with each
   % kij from simultaneous fitting

   Ts1=T2;
   Ts2=T2*0.5;
   par=[par(1) par(2) kijf(j)];
   for i=1:length(x1)
      Ts11=Ts1(i);
      Ts22=Ts2(i);
      err=1;
      while abs(err)>0.0001
         ph1(i,:)=phinithf(Ts11,P,x1(i),par,1);
         ph2(i,:)=phinithf(Ts22,P,x1(i),par,1);
         err1=1-(ph1(i,2)+x1(i)*(ph1(i,1)-ph1(i,2)));
         err2=1-(ph2(i,2)+x1(i)*(ph2(i,1)-ph2(i,2)));
         Ts=-err1*(Ts22-Ts11)/(err2-err1)+Ts11;
         ph(i,:)=phinithf(Ts,P,x1(i),par,1);
         err=1-(ph(i,2)+x1(i)*(ph(i,1)-ph(i,2)));
         if err<0
            Ts11=Ts;
         else
            Ts22=Ts;
         end
```

```
    end
    Tcalc(i)=Ts;
    phf(i,:)=ph(i,:);
    yf1(i)=x1(i)*ph(i,1);
end
Terr2(:,j)=T2-Tcalc;
Terr(j)=mean(abs(T2-Tcalc));
Tmax=max(T2-Tcalc);
yerr2(:,j)=y-yf1;
yerr(j)=mean(abs(y-yf1));
ymax=max(y-yf1);

% comparison between gert from the activity coeficient model and the
% EOS for each of the optimun

for i=1:length(x1)
    x11=x1(i);
    x=[x11 1-x11];
    % for thf and 2-propanol
    T=T2(i);
    gertac=gert(x,l12,l21);
    % for methanol cyclohexane
    %P=P2(i);
    %gertac=gertnrtl(T,x,al,g12,g21);
    a=alpha(T,Tc,Pc,w,k1,R);
    D=P;
    E=(D*b-R*T);
    F=-3*D*b.^2-2*R*T*b+a;
    G=D*b.^3-a.*b+R*T*b.^2;
    r1=roots([D E(1) F(1) G(1)]);
    r2=roots([D E(2) F(2) G(2)]);
    for q=1:3
        if r1(q)<0
            r1(q)=0;
        end
        if r2(q)<0
            r2(q)=0;
        end
    end
    v=[min(nonzeros(r1)) min(nonzeros(r2))];%
    A1=x*(log(v./(v-b)))';
    A2=(1/(R*T))*x*(a./(2*(2)^0.5*b).*log((v+b*(1-2^0.5))./(v+b*(1+2^0.5))))';
    A3=x*(P*v/(R*T)-1)'-x*(log(P*v/(R*T)))';
    B2=A1+A2+A3;
    A=b(1)-a(1)/(R*T);
    B=b(2)-a(2)/(R*T);
```

```
            C=a./b;
            svc=(x(1)^2*A+x(2)^2*B)+(x(1)*x(2)*(A+B))*(1-kijf(j));
            bm=svc/(1-gertac/(-0.623225240147)-(x*C')/(R*T));
            am=bm*(x*C'+gertac*R*T/(-0.623225240147));
            D=P;
            E=(D*bm-R*T);
            F=-3*D*bm^2-2*R*T*bm+am;
            G=D*bm^3-am*bm+R*T*bm^2;
            r=roots([D E F G]);
            for q=1:3
              if r(q)<0
                r(q)=0;
              end
            end
            vm=min(nonzeros(r));
            A4=log(vm/(vm-bm));
            A5=(1/(R*T))*am/(2*(2)^0.5*bm)*log((vm+bm*(1-2^0.5))/(vm+bm*(1+2^0.5)));
            A6=P*vm/(R*T)-1-log(P*vm/(R*T));
            gereos=(A4+A5+A6-B2);
            errge(i)=gereos-gertac;
          end
          errge1(j)=mean(abs(errge));
        end


        figure(1)
        subplot(2,2,1)
        plot(x1,kijf,'+k')
        xlabel('Molar Fraction of THF')
        ylabel('k_{12}')
        title({'a) k_{12} for Wilson parameters';' \Lambda_{12}=1.3477 and
\Lambda_{21}=0.65701'})
        subplot(2,2,2)
        plot(x1,errge1,'+k')
        xlabel('Molar Fraction of THF (only as label of k_{12})')
        ylabel('Difference of g^E/RT')
        title({'b) Difference of g^E calculated with Wilson';' and PRSV-WS for each k_{12} on
a.'})
        subplot(2,2,3)
        plot(x1,Terr,'+k')
        xlabel('Molar Fraction of THF (only as label of k_{12})')
        ylabel('T_{err} (^0C)')
        title({'c) Mean difference of T calculated with PRSV-WS';' and experimental for each
k_{12} on a.'})
        subplot(2,2,4)
        plot(x1,yerr,'+k')
```

```
xlabel('Molar Fraction of THF (only as label of k_{12})')
ylabel('y_{err}')
title({'d) Mean difference of y_{THF} calculated with PRSV-WS';' and experimental for each k_{12} on a.'})

figure(2)
subplot(1,2,1)
plot(x1,T2,'*k',x1,T2-Terr2(:,6)','-k',x1,T2-Terr2(:,9)','.-k',x1,T2-Terr2(:,11)',':k')
xlabel('x_{THF}')
ylabel('Temperature (^0C)')
legend('experimental','k_{12}=0.006607','k_{12}=0.007467','k_{12}=0.00806')
subplot(1,2,2)
plot(x1,y,'*k',x1,y-yerr2(:,5)','-k',x1,y-yerr2(:,10)','.-k',x1,y-yerr2(:,11)',':k')
xlabel('x_{THF}')
ylabel('y_{THF}')
legend('experimental','k_{12}=0.006607','k_{12}=0.007467','k_{12}=0.00806')
```

kijWSbinary1.m

```
clc
clear

% this routine presents the results of the binary parameters determination

%VLE experimental data

%for methanol benzene using the same isotherm

T=55+273.15;
y2=[0.3019 0.4051 0.4841 0.554 0.5845 0.5858 0.6078 0.6716 0.7997];
x1=[0.034 0.0493 0.1031 0.3297 0.4874 0.4984 0.6076 0.7896 0.9024];
P2=[465.84 527.12 597.48 664.24 675.62 675.99 678.44 664.91 622.29]*1.333E2;

%substance properties

R=8.31451;%J/(mol*K)
% for methanol benzene
Tc=[512.58 562.16];
Pc=[80.9579 48.98]*1E5;
w=[0.56533 0.20929];
k1=[-0.16816 0.07019];

% binary interaction parameters

par=[0.27376 1829.7 4517.3];
al=par(1);
g12=par(2);
```

```
g21=par(3);
b=0.077796*R*Tc./Pc;


kijf=kijWSbinary1f(par);
for j=1:length(x1)

   % error between experimental data and EOS VLE calculation with each
   % kij from simultaneous fitting

   Ps1=P2*1.5;
   Ps2=P2*0.5;
   par=[al g12 g21 kijf(j)];
   for i=1:length(x1)
      Ps11=Ps1(i);
      Ps22=Ps2(i);
      err=1;
      while abs(err)>0.0001
         ph1(i,:)=phini(T,Ps11,x1(i),par,1);
         ph2(i,:)=phini(T,Ps22,x1(i),par,1);
         err1=1-(ph1(i,2)+x1(i)*(ph1(i,1)-ph1(i,2)));
         err2=1-(ph2(i,2)+x1(i)*(ph2(i,1)-ph2(i,2)));
         Ps=-err1*(Ps22-Ps11)/(err2-err1)+Ps11;
         ph(i,:)=phini(T,Ps,x1(i),par,1);
         err=1-(ph(i,2)+x1(i)*(ph(i,1)-ph(i,2)));
         if err<0
            Ps11=Ps;
         else
            Ps22=Ps;
         end
      end
      Pcalc(i)=Ps;
      phf(i,:)=ph(i,:);
      yf1(i)=x1(i)*ph(i,1);
   end
   Perr2(:,j)=P2-Pcalc;
   Perr(j)=mean(abs(P2-Pcalc));
   Pmax=max(P2-Pcalc);
   yerr2(:,j)=y2-yf1;
   yerr(j)=mean(abs(y2-yf1));
   ymax=max(y2-yf1);

   % comparison between gert from the activity coeficient model and the
   % EOS for each of the optimun

   for i=1:length(x1)
```

```
x11=x1(i);
x=[x11 1-x11];
% for thf and 2-propanol
%T=T2(q);
%P=1.01325;
%gertac=gert(x,l12,l21);
% for methanol cyclohexane/benzene
P=P2(i);
gertac=gertnrtl(T,x,al,g12,g21);
a=alpha(T,Tc,Pc,w,k1,R);
D=P;
E=(D*b-R*T);
F=-3*D*b.^2-2*R*T*b+a;
G=D*b.^3-a.*b+R*T*b.^2;
r1=roots([D E(1) F(1) G(1)]);
r2=roots([D E(2) F(2) G(2)]);
for q=1:3
      if r1(q)<0
         r1(q)=0;
      end
      if r2(q)<0
         r2(q)=0;
      end
end
v=[min(nonzeros(r1)) min(nonzeros(r2))];%
A1=x*(log(v./(v-b)))';
A2=(1/(R*T))*x*(a./(2*(2)^0.5*b).*log((v+b*(1-2^0.5))./(v+b*(1+2^0.5))))';
A3=x*(P*v/(R*T)-1)'-x*(log(P*v/(R*T)))';
B2=A1+A2+A3;
A=b(1)-a(1)/(R*T);
B=b(2)-a(2)/(R*T);
C=a./b;
svc=(x(1)^2*A+x(2)^2*B)+(x(1)*x(2)*(A+B))*(1-kijf(j));
bm=svc/(1-gertac/(-0.623225240147)-(x*C')/(R*T));
am=bm*(x*C'+gertac*R*T/(-0.623225240147));
D=P;
E=(D*bm-R*T);
F=-3*D*bm^2-2*R*T*bm+am;
G=D*bm^3-am*bm+R*T*bm^2;
r=roots([D E F G]);
for q=1:3
  if r(q)<0
    r(q)=0;
  end
end
vm=min(nonzeros(r));
```

```
        A4=log(vm/(vm-bm));
        A5=(1/(R*T))*am/(2*(2)^0.5*bm)*log((vm+bm*(1-2^0.5))/(vm+bm*(1+2^0.5)));
        A6=P*vm/(R*T)-1-log(P*vm/(R*T));
        gereos=(A4+A5+A6-B2);
        errge(i)=gereos-gertac;
    end
    errge1(j)=mean(abs(errge));
end
figure(1)
subplot(2,2,1)
plot(x1,kijf,'+k')
xlabel('x_1')
ylabel('k_{12}')
title({'a). k_{12} for NRTL values';' \alpha=0.27376 g_{12}=1829.7 g_{21}=4517.3'})
subplot(2,2,2)
plot(x1,errge1,'+k')
xlabel('x_1(only as label of k_{12})')
ylabel('Difference of g^E/RT')
title({'b) Difference of g^E calculated with NRTL';' and PRSV-WS for each k_{12} on
a.'})
subplot(2,2,3)
plot(x1,Perr/1000,'+k')
xlabel('x_1(only as label of k_{12})')
ylabel('P_{err} (kPa)')
title({'c) Mean difference of P calculated with PRSV-WS';' and experimental for each
k_{12} on a.'})
subplot(2,2,4)
plot(x1,yerr,'+k')
xlabel('x_1(only as label of k_{12})')
ylabel('y_{err}')
title({'d) Mean difference of y_1 calculated with PRSV-WS';' and experimental for each
k_{12} on a.'})

figure(2)
subplot(1,2,1)
plot(x1,P2/1000,'*k',x1,(P2-Perr2(:,4)')/1000,'-k',x1,(P2-Perr2(:,5)')/1000','.-k',x1,(P2-
Perr2(:,6)')/1000',':k')
xlabel('x_{1}')
ylabel('Pressure (kPa)')
legend('experimental','k_{12}=0.45','k_{12}=0.3168','k_{12}=0.25')
subplot(1,2,2)
plot(x1,y2,'*k',x1,y2-yerr2(:,4)','-k',x1,y2-yerr2(:,5)','.-k',x1,y2-yerr2(:,6)',':k')
xlabel('x_{1}')
ylabel('y_{1}')
legend('experimental','k_{12}=0.45','k_{12}=0.3168','k_{12}=0.25')
```

thf2propmT.m

```
clc
clear
x=[0:0.025:1];
par=[1.3477 0.65701 0.006607];
T1=[90:20:250]+273.15;
for ji=1:length(x)
   x1=x(ji);
   a=[6.99515 6.6604];
   b=[1202.29 813.055];
   c=[226.254 132.93];
   Ps1=10.^(a(1)-b(1)./(T1+c(1)-273.15));
   Ps2=10.^(a(2)-b(2)./(T1+c(2)-273.15));
   Ps=(x1*Ps1+Ps2*(1-x1))*101325/760;
      for i=1:length(T1)
         A=BubPbin(Ps(i),T1(i),x1,par);
         BubP(i)=A(1);
         vml(i)=A(2);
         B=DewPbin(Ps(i),T1(i),x1,par);
         DewP(i)=B(1);
         vmv(i)=B(2);
         %if BubP(i)<DewP(i)
            %BubP(i)=DewP(i);
         %end
      end
   BubP1(ji,1:length(BubP))=BubP;
   DewP1(ji,1:length(DewP))=DewP;
end
%[x2,t2]=meshgrid(x,T1);
figure(1)

subplot(3,3,1)
plot(x,BubP1(:,1)/100000,'-k',x,DewP1(:,1)/100000,'--k')
legend('BuP','DewP')
title('V-L-E at 90^oC')

subplot(3,3,2)
plot(x,BubP1(:,2)/100000,'-k',x,DewP1(:,2)/100000,'--k')
title('V-L-E at 110^oC')

subplot(3,3,3)
plot(x,BubP1(:,3)/100000,'-k',x,DewP1(:,3)/100000,'--k')
title('V-L-E at 130^oC')

subplot(3,3,4)
plot(x,BubP1(:,4)/100000,'-k',x,DewP1(:,4)/100000,'--k')
ylabel('Pressure (bar)')
```

```
title('V-L-E at 150^oC')

subplot(3,3,5)
plot(x,BubP1(:,5)/100000,'-k',x,DewP1(:,5)/100000,'--k')
title('V-L-E at 170^oC')

subplot(3,3,6)
plot(x,BubP1(:,6)/100000,'-k',x,DewP1(:,6)/100000,'--k')
title('V-L-E at 190^oC')

subplot(3,3,7)
plot(x,BubP1(:,7)/100000,'-k',x,DewP1(:,7)/100000,'--k')
title('V-L-E at 210^oC')

subplot(3,3,8)
plot(x,BubP1(:,8)/100000,'-k',x,DewP1(:,8)/100000,'--k')
xlabel('x_1-y_1')
title('V-L-E at 230^oC')

subplot(3,3,9)
plot(x,BubP1(:,9)/100000,'-k',x,DewP1(:,9)/100000,'--k')
title('V-L-E at 250^oC')
```

metholbenzmT.m

```
clc
clear
x=[0:0.1:1];
kij=[0.45 0.3168 0.25];
T1=[100 140 180 215]+273.15;
Fres(:,1)=x;
for h=1:length(kij)
   par=[0.27376 1829.7 4517.3 kij(h)];
   for ji=1:length(x)
      x1=x(ji);
      a=[7.87863 6.90565];
      b=[1473.11 1211.033];
      c=[230 220.79];
      Ps1=10.^(a(1)-b(1)./(T1+c(1)-273.15));
      Ps2=10.^(a(2)-b(2)./(T1+c(2)-273.15));
      Ps=(x1*Ps1+Ps2*(1-x1))*101325/760;
         for i=1:length(T1)
            A=BubPbinnrtl(Ps(i),T1(i),x1,par);
            BubP(i)=A(1);
            vml(i)=A(2);
            B=DewPbinnrtl(Ps(i),T1(i),x1,par);
            DewP(i)=B(1);
```

```
            vmv(i)=B(2);
            %if BubP(i)<DewP(i)
               %BubP(i)=DewP(i);
            %end
          end
        BubP1(ji,1:length(BubP))=BubP;
        DewP1(ji,1:length(DewP))=DewP;
    end
    Fres=[Fres BubP1 DewP1];
end
Fres1=Fres(:,2:2*length(T1)+1);
Fres2=Fres(:,2*length(T1)+2:4*length(T1)+1);
Fres3=Fres(:,4*length(T1)+2:6*length(T1)+1);
x1=[0.0926 0.3328 0.5940 0.729 0.8596 0.9056];
y1=[0.4577 0.6075 0.6708 0.7084 0.7868 0.8376];
P1=[45.3 55.6 59.7 60.4 58.4 57.3]*1.01325/14.7;
x2=[0.0619 0.2018 0.456 0.6845 0.8614 0.9159];
y2=[0.3224 0.5469 0.6644 0.7344 0.8317 0.8773];
P2=[97.8 133.8 160.8 167.5 170 167.5]*1.01325/14.7;
x3=[0.045 0.1748 0.4268 0.6632 0.8942 0.9511];
y3=[0.227 0.4819 0.6546 0.7583 0.8915 0.9461];
P3=[191.2 266.5 354.7 389.5 400.5 396.5]*1.01325/14.7;
x4=[0.0233 0.1778 0.4996 0.7474 0.8933 0.9521];
y4=[0.1068 0.4485 0.6864 0.8117 0.8999 0.9477];
P4=[328 497.5 693 800.5 836 835]*1.01325/14.7;
figure(1)
subplot(1,3,1)
semilogy(x1,P1,'*k',x2,P2,'+k',x3,P3,'oK',x4,P4,'sk',x,Fres1/100000,'-
k',y1,P1,'*k',y2,P2,'+k',y3,P3,'oK',y4,P4,'sk')
title('k_{12}=0.45')
legend('T=100^oC','T=140^oC','T=180^oC','T=220^oC','Predicted')
xlabel('x_1-y_1')
ylabel('Pressure (bar)')
subplot(1,3,2)
semilogy(x1,P1,'*k',x2,P2,'+k',x3,P3,'oK',x4,P4,'sk',x,Fres2/100000,'-
k',y1,P1,'*k',y2,P2,'+k',y3,P3,'oK',y4,P4,'sk')
title('k_{12}=0.3168')
xlabel('x_1-y_1')
subplot(1,3,3)
semilogy(x1,P1,'*k',x2,P2,'+k',x3,P3,'oK',x4,P4,'sk',x,Fres3/100000,'-
k',y1,P1,'*k',y2,P2,'+k',y3,P3,'oK',y4,P4,'sk')
title('k_{12}=0.25')
xlabel('x_1-y_1')
```

BubPbin.m

```
function Pb=BubPbin(Ps,T,x,par)%
```

```
p=Ps;
k=zeros(1,2);
x1=[x 1-x];
fl=phinithf(T,p,x,par,1);%liquid
vme=fl(3);
fl=fl(1:2);
fv=phinithf(T,p,x*0.5,par,2);%vapor
fv=fv(1:2);
k=fl./fv;
y=k.*x1;
b=1-sum(y);
deltaP=100000;
if abs(b)<=0.000001
   vml=vme;
end
while abs(b)>0.000001
 skx=sum(y);
 dskx=1;
 while abs(dskx)>0.000001 % loop to stabilize the conc in a [0,1] interv
  y=y./sum(y); % to make sure both of them are less than 1
  fv=phinithf(T,p,y(1),par,2);%vapor
  vmv=fv(3);
  fv=fv(1:2);
  fl=phinithf(T,p,x,par,1);%liquid
  vml=fl(3);
  fl=fl(1:2);
  k=fl./fv;
  y=k.*x1;
  dskx=skx-sum(y);
  skx=sum(y);
 end
 bant=b;
 b=1-sum(y);
 c=b*bant;
 if c<=0
    deltaP=deltaP/10;
 end
 if b>0
   p=p-deltaP;
 else
   p=p+deltaP;
 end
end
Pb=[p vml];
```

DewPbin.m

```
function Pb=DewPbin(Ps,T,y,par)
p=Ps;
k=zeros(1,2);
y1=[y 1-y];
fl=phinithf(T,p,y*1.5,par,1);%liquid
fl=fl(1:2);
fv=phinithf(T,p,y,par,2);%vapor
vme=fv(3);
fv=fv(1:2);
k=fl./fv;
x=y1./k;
b=1-sum(x);
deltaP=100000;
if abs(b)<=0.000001
   vmv=vme;
end
while abs(b)>0.000001
 skx=sum(x);
 dskx=1;
 while abs(dskx)>0.000001
  x=x./sum(x);
  fl=phinithf(T,p,x(1),par,1);%liquid
  vml=fl(3);
  fl=fl(1:2);
  fv=phinithf(T,p,y,par,2);%vapor
  vmv=fv(3);
  fv=fv(1:2);
  k=fl./fv;
  x=y1./k;
  dskx=skx-sum(x);
  skx=sum(x);
 end
 bant=b;
 b=1-sum(x);
 c=b*bant;
 if c<=0
    deltaP=deltaP/10;
 end
 if b>0
   p=p+deltaP;
 else
   p=p-deltaP;
 end
end
Pb=[p vmv];
```

thf2prop.m

```
clc
clear
x=[0.24 0.64];
par=[1.3477 0.65701 0.006607];
T1=[90:10:280]+273.15;
for ji=1:length(x)
   x1=x(ji);
   a=[6.99515 6.6604];
   b=[1202.29 813.055];
   c=[226.254 132.93];
   Ps1=10.^(a(1)-b(1)./(T1+c(1)-273.15));
   Ps2=10.^(a(2)-b(2)./(T1+c(2)-273.15));
   Ps=(x1*Ps1+Ps2*(1-x1))*101325/760;
      for i=1:length(T1)
         A=BubPbin(Ps(i),T1(i),x1,par);
         BubP(i)=A(1);
         vml(i)=A(2);
         B=DewPbin(Ps(i),T1(i),x1,par);
         DewP(i)=B(1);
         vmv(i)=B(2);
      end
   BubP1(ji,1:length(BubP))=BubP;
   DewP1(ji,1:length(DewP))=DewP;
end
Tmeas1=[162 174 184 189 199 206 219 227 228 245 251 257 262 264];
Pmeas1=[14 17.5 21 24 29 32 40 42 50 55 57.5 60 62.5 65]+1.01235;
Tmeas2=[161 176 189 195 210 222 231 236 241 249 254 260 264];
Pmeas2=[12.5 16 20 22.5 30 35 40 45 50 52.5 55 57 59]+1.01235;

figure(1)
subplot(1,2,1)
plot(T1(1:13)-273.17,BubP1(1,1:13)/100000,'-k',T1(1:13)-
273.15,DewP1(1,1:13)/100000,'-.k',T1(1:20)-273.15,Ps1(1:20)*1.01325/760,':k',T1(1:16)-
273.15,Ps2(1:16)*1.01325/760,'--k',Tmeas1,Pmeas1,'*k')
legend('BuP','DewP','pure THF','pure 2-propanol','Autoclave readings')
title('molar fraction of THF 0.24 (45 mL of alcohol)')
xlabel('Temperature (^oC)')
ylabel('Pressure (bar)')
subplot(1,2,2)
plot(T1(1:14)-273.15,BubP1(2,1:14)/100000,'-k',T1(1:14)-
273.15,DewP1(2,1:14)/100000,'-.k',T1(1:20)-273.15,Ps1(1:20)*1.01325/760,':k',T1(1:16)-
273.15,Ps2(1:16)*1.01325/760,'--k',Tmeas2,Pmeas2,'*k')
title('molar fraction of THF 0.64 (20 mL of alcohol)')
xlabel('Temperature (^oC)')
```

Appendix C Sol-gel prepared alumina films as coatings

The main goal of this appendix is to describe the possibilities of generating infrared radiation from oxidation processes that might last for long periods of time. Pyrophoric properties of metal oxidation reactions make them likely to be considered as a suitable source of heat to emit infrared radiation [111]. The exothermic nature of these reactions is also valuable at low temperatures [112]. Oxidation of iron, activated by chloride salts, with the presence of water and carbon is the source of heat for commercial, domestic and medical body warmers [113]. The role of each component of the heat-generating mixtures (Fe+C+H_2O+NaCl) has been described in the literature. Carbon (in the form of activated carbon) delivers water to the oxidation reactions and some of its surface functional groups contribute as catalysts for the oxidation reaction [114]. Chloride salts have been suggested as promoters of ion transport and electronic tunneling from metal to the adsorbed oxygen and water [111]. The final composite material is embedded in a polymeric matrix that controls the dissipation of heat and the transport of oxygen from the air to the metal surface [113].

In exploratory experiments (shown in following sections) it was found that neither the patent literature nor the journal literature reports any details on the blending procedures of the main components of the heat generating mixtures. The purpose of the present study is determining the influence of mixing stages to possibly extend the duration of the heat emission of the mixtures. Additionally, the control of oxygen diffusion to the iron particles is considered a very important issue to maintain the heat generation for long periods of time. Therefore alternatives to this issue by coating the reaction surface are also explored in this work.

C.1 Preparation of heat generating mixtures

C.1.1 Exploratory experiments on blending times

Two different compositions were explored. The first preparation is reported in the patent literature [115, 116]. Low contents of activated carbon and high concentrations of salt are the main characteristics of this preparation. The second preparation is reported by Bavieskaya et al. [113], which is characterized by high contents of activated carbon and low concentrations of salt.

The first preparation yielded slurries that did not generate heat. Their high water contents blocked the access of oxygen to the iron particles. The second preparation yielded mixtures with less amount of water; those increased their surface temperature once they were exposed to the air. To prepare these composites, 4.5 g of a 5% NaCl in water solution were added to 2 g of activated carbon and contacted during 3 days to ensure an appropriate impregnation of the porous carbon with salt solution. Then, 10 g of reduced iron powder were added to the water-salt-carbon mixture and blended inside a nitrogen-atmosphere glove box. Two types of activated carbon were employed with different particle size (-100 and 20-40 mesh sizes).

The preparations were tested with a very simple experiment. The powders were taken out of the box, exposed to the atmosphere and the surface temperature was measured with a pyrometer. The powders were frequently stirred to ensure complete oxidation of iron. For comparison the heat generating solid mixture of a commercial hand warmer and a commercial foot warmer were evaluated with this test.

The results of the above mentioned exploratory experiment are shown in Figure C.1. The prepared mixtures generated values of the surface temperature similar to the ones generated by the commercial products. However a delay in the appearance of the maximum temperature was observed. The particle size of the activated carbon also influenced the time at which the maximum temperature was reached. The larger the particle the longer the time.

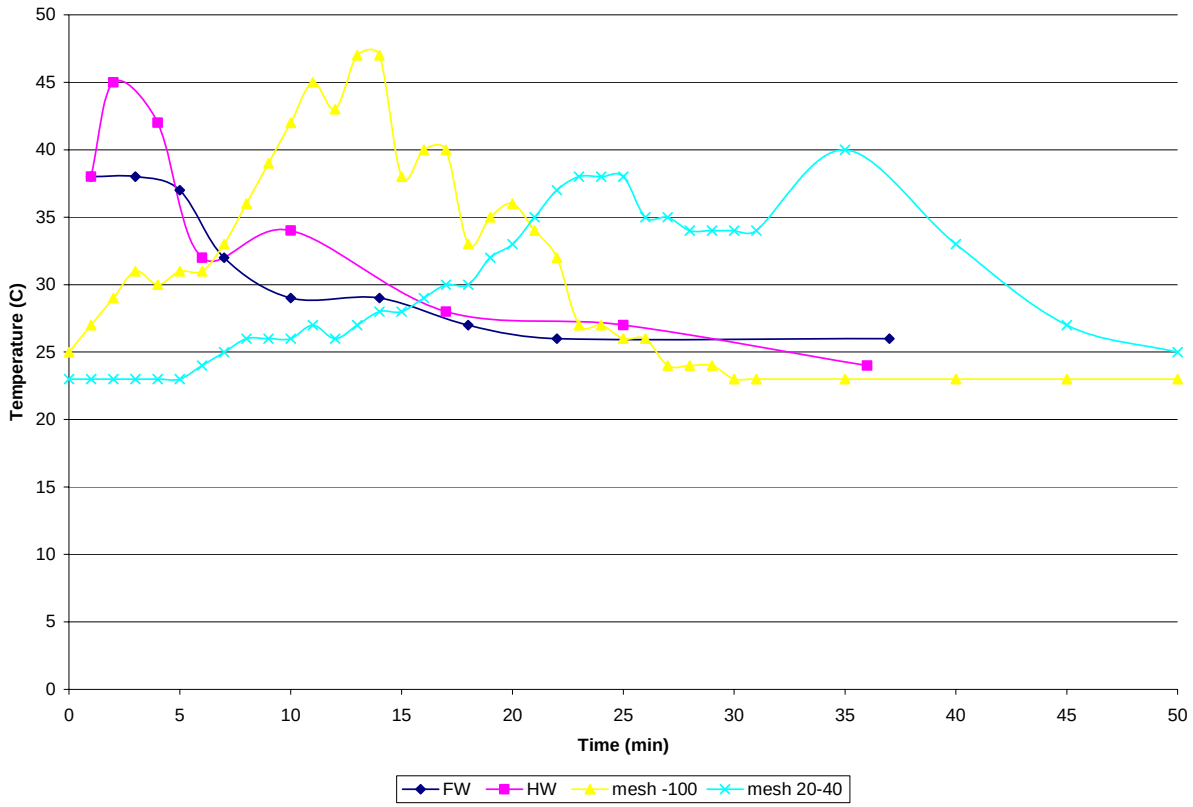

Figure C.1 Surface temperature of heat-emitting mixtures exposed to the air. FW: Commercial foot warmer. HW: Commercial hand warmer.

The first analysis of the preparation techniques involved the influence of the aging time during two stages of the blending process on the surface temperature of the mixtures. The studied stages are the mixing of the salt solution and the activated carbon and the mixing of such slurry with the iron powder. For the first mixing process, two levels of aging were analyzed: overnight and three days. For the second blending process three levels were taken into account: 0, 1 and 5 days. The results are shown in Figure C.2 for a 20-40 mesh activated carbon and in Figure C.3 for the -100 mesh activated carbon.

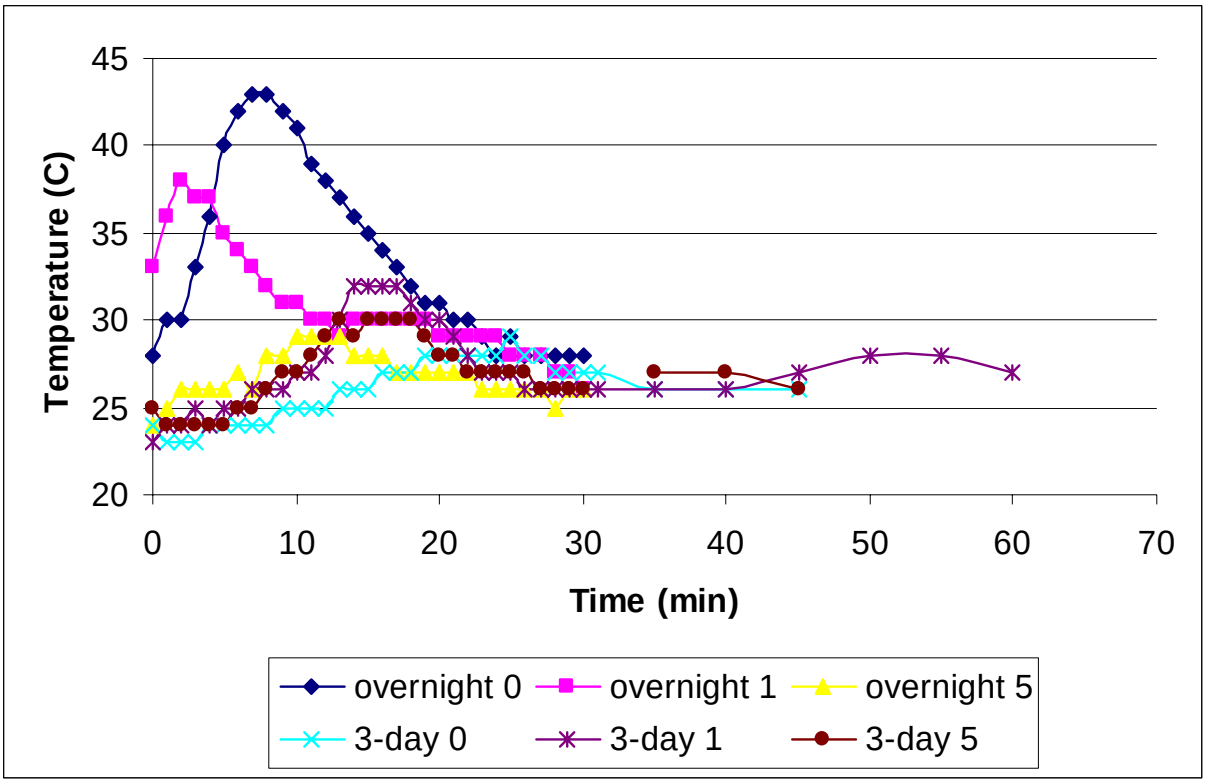

Figure C.2 Surface temperature of heat-emitting mixtures exposed to the air when activated carbon 20-40 was used

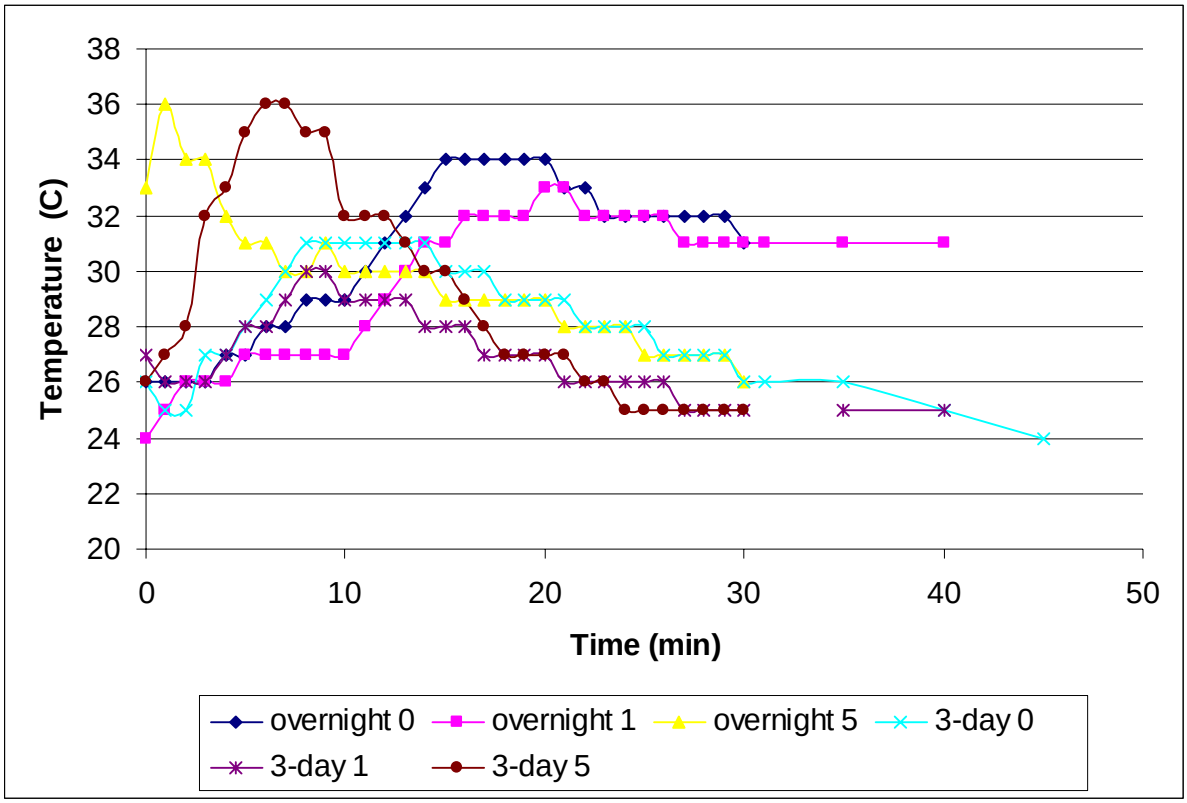

Figure C.3 Surface temperature of heat-emitting mixtures exposed to the air when activated carbon -100 was used

Clearly, the results show that the particle size of the activated carbon affects the oxidation reaction and consequently the surface temperature. For the 20-40 mesh activated carbon the aging time for both stages doesn't increase the surface temperature and only changes the location of the maximum temperature. When the initial blending is very long, the temperature decreased for the 20-40 activated carbons. This is probably due to the deep impregnation of the salt solution, once inside the big particles, it can not go out to react with iron and oxygen. For this type of activated carbon short blending times are preferable.

For the -100 mesh activated carbon the situation is considerably different. When the first stage is carried out overnight the extension of the reaction (as measured by the surface temperature) is favored for short periods of contact with iron powder although after 5 days the material has a very fast initial reaction. When the contact time of the salt solution and activated carbon is 3-day long, the long period of contact with the iron powder is certainly better. Small

particles and higher surface area carbons are able to hold the water molecules longer than big particles. When all the components are together for a long time the reaction lasts longer as well.

C.1.2 Experiments on blending times

The previous section discussed exploratory experiments that showed a possible important influence of the particle size of the activated carbon on the surface temperature of the heat generating materials. However, the inferences about the impregnation times for the activated carbon with the saline solution and the blending times of iron with carbon-salt mixture were not completely supported by statistically significant data. To understand and validate the influence of these preparation variables in the surface temperature of the materials, an experiment including these two factors was planned.

Two mixtures (one for each type of activated carbon) were prepared by mixing activated carbon with the 5%-saline solution. Samples were randomly drawn from each mixture after 0, 1 and 3 days and immediately mixed with iron powder. These final heat-generating mixtures were stored inside the nitrogen-atmosphere glove box and three samples of approximately 2 g each were taken for the surface temperature measurement after 0, 2 and 5 days of storage. The measurements were carried out with a 5-minute interval from 0 to 100 min. The whole process was repeated once for accuracy. The results of the first analysis are shown in Figure C.4 and Figure C.5.

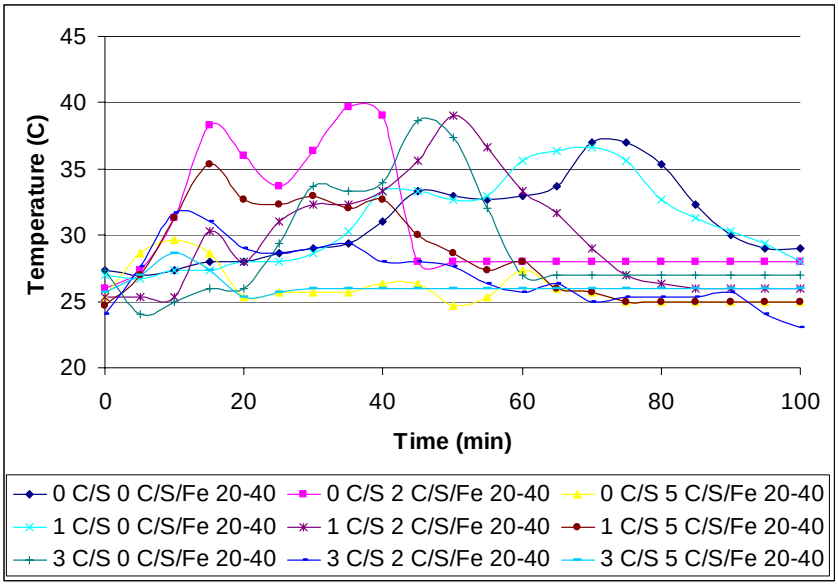

Figure C.4 Surface temperature of heat-emitting mixtures exposed to the air. C/S: Days aging for carbon-saline solution mixture before iron adding. C/S/Fe: Days of aging for carbon-saline solution-Iron powder mixture before analysis. 20-40: mesh size of activated carbon employed

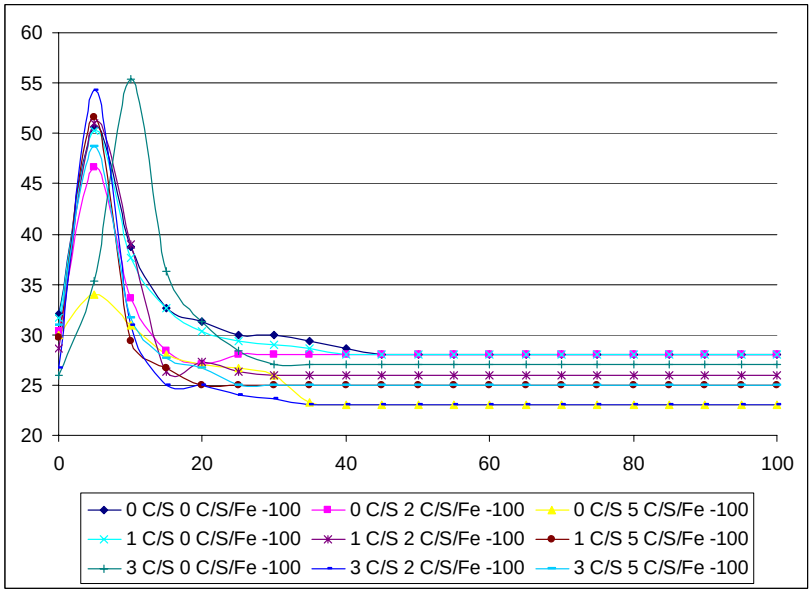

Figure C.5 Surface temperature of heat-emitting mixtures exposed to the air. C/S: Days aging for carbon-saline solution mixture before iron adding. C/S/Fe: Days of aging for carbon-saline solution-Iron powder mixture before analysis. -100: mesh size of activated carbon employed

Two main response variables were studied in this analysis: the maximum difference between the surface temperature and the room temperature and time required for the reaction to reach such a maximum difference.

The maximum temperature is shown in Table C.1. From these values we can conclude that the time that the carbon and the saline solution are in contact before the addition of the iron powder does not affect the maximum temperature when the particle size of the activated carbon is small. When a large-particle activated carbon is employed, the temperature difference presents a minimum that may be attributed to diffusion of saline solution inside the carbon particles since it doesn't contact the iron powder. The temperature difference increases after some of the external water is evaporated and the salt concentration increases. The time that the whole blend remains stored before its exposure to air doesn't influence the maximum temperature difference for both activated carbon types. We conclude that small particle size will always produce the same results in terms of the reached maximum temperature difference; the large particle carbon may be generating diffusion effects which are affecting the temperature difference.

Table C.1 Maximum temperature differences between the surface and the room (°C) reached by the mixtures. Values with the same letter are not significantly different.

Mesh size of activated Carbon	Time to mix the carbon-saline blend with iron powder (days)		
	0	1	3
-100	22.5[a]	17.9[a]	18.9[a]
20-40	22.9[a]	14.4[b]	20.22[a]
Mesh size of activated Carbon	Time to expose the heat-generating mixture to the atmosphere to test		
	0	2	5
-100	23[a]	16.4[b]	19.94[a,b]
20-40	20.44[a]	17.44[a]	19.667[a]

The time at which the mixtures reached the maximum temperature difference is shown in Table C.2. We had already concluded that the time to reach the maximum temperature difference is shorter for mixtures containing small-particle carbon and now we conclude that the preparation contact times don't influence it. The large particles of carbon have a long response time when carbon and saline solution are contacted only for one day. Again we can attribute this

behavior to the diffusion of the solution inside the particles. The shortest response time is for the mixtures analyzed 5 days after preparation.

Table C.2 Time for materials to reach the maximum temperature differences between the surface and the room (min.). Values with the same letter are not significantly different.

Mesh size of activated Carbon	Time to mix the carbon-saline blend with iron powder (days)		
	0	1	3
-100	5.1[a]	8.9[b]	6.5[a,b]
20-40	21.4[a]	50.6[b]	22.2[a]
Mesh size of activated Carbon	Time to expose the heat-generating mixture to the atmosphere to test		
	0	2	5
-100	5.4[a]	11.3[b]	4.9[a,b]
20-40	37.5[a]	41.9[a]	14.7[b]

C.2 Coating surfaces with alumina films

Controlling the diffusion of oxygen to the reacting surface by embedding the iron/carbon/ saline mixture in a porous polymeric matrix allowed prolongation of the heat generating reaction in the commercial body warmers [113]. Coating the surface with a porous film can play the same role as the polymeric materials and increase the reaction lifetime.

C.2.1 Choice of the best alumina alkoxide

The exploratory work was started with the preparation of the alkoxide sol. Initially two main procedures were followed according to the patent literature [117]. The partial hydrolysis of aluminum sec-butoxide was carried out in ethanol which yielded a very clear solution as precursor for the coating material. Partial hydrolysis of aluminum triisopropoxide in ethanol and ethanol-toluene didn’t generate clear solutions.

Heat generating mixtures were pelletized to be able to dip them in the sec-butoxide solution and dried at room temperature in a vacuum line. Although oxidation was observed (change of color of the solid surface), the surface temperature did not increase upon exposure to air. The final product was a mixture of a white fluffy powder with the partially rusted iron. It is possible that the aluminum hydroxide powders did not adhere to the heat generating mixture.

Any heat released may have been consumed during the drying process. Spraying and spreading the solution over the pellets were also tried with the same results.

A second approach was based on the synthesis of permeable alumina membranes reported by the literature [118]. In this procedure aluminum iso-propoxide was added to an excess of water at 80°C and peptized with acetic acid overnight. The translucent sol was poured over the heat generating mixture in a Petri dish. The drying process was carried out at atmospheric conditions. This preparation generated relatively thin films attached to the surface of the powder. The presence of water as solvent leads the process to a very stressful drying step due to the high surface tension, however large domains of material were crack-free. The iron mixture was prematurely exposed to the atmosphere through the few cracks that did exist and oxidation started. As evidence of the heat generating reactions, faster evaporation was observed in those regions of the dish where the mixture was deposited. Finally orange (rusted) shiny plaques were obtained from the dish.

C.2.2 Thick films for more resistant coatings

To prevent cracking, a thick film (more resistant to mechanical stress) was obtained with partial evaporation of the water. After several trials it was found that removing about 80% of the initial mass of the sol leads to the formation of a very thick gel. The sol was poured into a plastic dish and was dried at room temperature until it reached 20% of its initial weight. A viscous gel is formed. This process also helped to partially remove the acetic acid (used to peptize the aluminum hydroxide) which could be contributing to early oxidation reactions. The presence of thick films also increased the drying time, thus the drying process was undertaken in a vacuum line. For this approach a pellet, the size of quarter was formed by pressing the mixture at pressures up to 3500 psi. This pellet was then placed over the partially dried gel. To complete the coverage, other portions of the gel were spread over the top of the pellet and the whole system was dried under vacuum. After 2 h of exposure to the atmosphere, the temperature of the coated pellet started increasing from 4°C to 13°C above room temperature and the condition was maintained for 90 min. It is interesting to note that the bottom coating of the gel was a very homogeneous thin film of the alumina membrane that was pealed from both the pellet and the plastic dish. The top coating remained attached to the surface since it is a thicker membrane produced by the manual spread of the gel.

Subsequently, small pellets were coated with the alumina films. Particles were made by breaking down pressed portions of the mixture and thick films were made by spreading the alumina concentrated gel and drying under vacuum. When the materials were exposed to the atmosphere, their surface temperature decreased as an evidence of incomplete drying. After about 3 hours of atmosphere contact, big cracks showed up again in the coating allowing direct exposure of the iron surface to air. The vacuum and atmospheric drying processes still generate enough large stresses on the alumina membrane to crack the coating even though the particles are small.

C.2.3 Thin films of alumina as coatings

As the ideas on thick membranes did not succeed, the thin films were employed again as a suitable alternative, now with a different approach for the coating procedure. The sol was prepared in the same way as described above and the pelletized mixture was made in the same way as well; however the sol was dropped on the pellets on a fritted funnel. In this way the minimum amount of sol was deposited on the surface of the particles. The particles were placed under vacuum for about 3 hours and then left overnight in an evacuated cell. When the particles were exposed to the atmosphere, a shiny coating was observed on all of them. The maximum surface temperature was reached after 15 minutes and a minimum of 3°C difference from the room temperature was kept until 40-60 minutes of exposure. The oxidation was also observed by the change in the color of the surface. Orange domains were dispersed on the surface, evidencing a very heterogeneous distribution of the heat generating spots in the particles. Some of the well coated particles did not have any orange domain and some other ones were completely orange.

C.2.4 Conclusion and alternative approaches

A complete coating process has not been possible. However, results described in previous sections demonstrated some extension of the oxidation reaction by delaying the emergence of the maximum temperature (compared with the results in Figure C.5, Table C.1 and Table C.2 for the mixtures prepared with -100 mesh size activated carbon). A summary of the observed difficulties and advantages when coating iron mixtures with porous alumina is shown in Table C.3. A breakable film is the main problem when gel spreading and sol spraying have been used. This condition may be attributed to the rigidness and fragility of porous alumina.

Composite materials as precursors of the specifically microstructured alumina have reported strong interactions between polymers and polynuclear hydroxyaluminum (suspended species of the alumina sols) [119]. It is suggested that this strong interaction may provide some flexibility to the film without affecting its porosity. The polymer that was tested is polyethylene glycol (PEG). Low molecular weights are important to avoid the reduction of porosity and to improve the solubility in the alumina sol, but high molecular weights might provide very low glass transition temperatures which should provide flexibility to the alumina matrix. Suggested molecular weight for appropriate solubility of PEG is 2000 and its glass transition temperature is -72°C [120].

Table C.3 Advantages 1) and difficulties 2) when coating iron mixtures with alumina sols

Coating method that controls film thickness	Size of pellet	
	Large (2 cm)	Small (0.5 cm)
Spread gel over the pellet surface (generates thick coatings)	1) Good adhesion of the film to the surface of the pellets helps to the complete coverage 2) Heterogeneous thickness, long time for drying and size of pellet are difficulties for the application	1) Thickness control is easier in smaller coating areas 2) High surface tension applied to small lengths breaks the films and expose the material directly to the air
Pellet deposited over a thin film of partially dried gel or impregnation with sol over the pellets (generates thin coatings)	1) Homogeneous thickness when the pellet is deposited on a partially dried gel 2) Adhesion of the film to large areas of pellet is not complete and it peels off the surface directly exposing the pellet to atmosphere.	1) Complete and homogeneous coating that can be dried easily 2) Small pellets don’t contain the compounds of the heating mixture in the same ratios as the bulk (bad mixing of solids is more influential)

The amount of polymers was determined using a ratio of the weight of aluminum ions to weight of polymer [120] Two Al:polymer ratios (1:3 and 1:6) were employed to inspect the flexibility of the films. In both cases the solubility of the polymer in the alumina sol was complete. The sol-polymer mixture was allowed to dry overnight and the films were manually bent to test the flexibility. Apparently, increasing the ratio improves the flexibility but this fact needs to be quantified with a better experimental technique. PEG seems to be a good polymer to improve the flexibility.

A mixture with Al:polymer ratio 1:6 of alumina sol and polyethylene glycol (PEG) was employed to coat the heat generating powders. The initial approach aimed to coat pellets of heating powders by dropping the solution over the materials and evaporating the liquid under vacuum. The vacuum evaporation quickly removed most of the liquid but large bubbles created by the viscous coating destroyed some parts of the coating films and when the material was exposed to the air not all of the pellets were completely coated. Drying under atmospheric conditions was carried out by incorporating a water adsorbent (Ascarite) into the drying chamber. In this case the films peeled off from the flat surfaces of the pellets, directly exposing parts of the mixture to the air. Pellets are easy to handle during the coating process but the large surfaces are difficult to keep coated even with flexible films.

Powder (small and medium chunks as they are produced after the mixing process) was coated with the alumina-PEG mixture and dried under atmospheric pressure in the presence of Ascarite. When the material was exposed to the atmosphere, a homogenous film was observed coating the small chunks of carbon-iron-salt composite. Surface temperature kept a difference of only 2°C with room temperature for at least 90 min. Homogenous oxidation was evidenced by the change in the color of the material.

More work is necessary in the application of these alternative composites. For example, evaluation of the permeability of the coatings, homogeneity of the heat generating mixtures and alternative coating methodologies should be studied.